

POLITECNICO DI TORINO

Department of Structural, Geotechnical and Building Engineering



**Politecnico
di Torino**

Master's Degree in Civil Engineering

CALIBRATION OF A MULTI-STRUT MACRO MODEL FOR SEISMIC ANALYSIS OF INFILLED REINFORCED CONCRETE FRAMES

Supervisor

Prof. Fabio Di Trapani

Candidate

Santosh Shrestha

Co-supervisor

Ing. Marilisa Di Benedetto

Ing. Antonio Pio Sberna

Academic Year 2023-2024

Thesis Certificate

This is to undertake the thesis titled “Calibration of a Multi-strut Macro Model for Seismic Analysis of Infilled Reinforced Concrete Frames”. The proposed model has three struts one diagonal and two non-diagonal in the reinforced concrete frame. The study will determine the equivalent width of each strut and the position of the non-diagonal strut for maximum shear demand at the column ends. This thesis is submitted to the Department of Structural, Geotechnical and Building Engineering, Politecnico di Torino, Italy for the ward on Master of Science in Civil Engineering. This research was done by me under the supervision of Prof. Fabio Di Trapani and Ph.D. scholar Marilisa Di Benedetto and Antonio Pio Sberna . The contents of this thesis in full or in parts, have not been submitted to any other Institute or University for the award of any degree or diploma.

Signature of the Author: _____

Santosh Shrestha

Certified by: _____

Prof. Fabio Di Trapani

Accepted by: _____

ABSTRACT

Reinforced concrete (RC) frames often incorporate unreinforced masonry infills which are composed of either solid or hollow clay bricks or concrete units and have been widely used for many decades around the world. Researchers have discovered that masonry infill enclosed in RC frames has a considerable stiffening and strengthening effect, which can be beneficial or adverse in the case of seismic action and influences global displacement capacity. Although numerous experimental and numerical studies have shown in different literature that masonry infills modify the behaviour of framed structures under lateral loads, the contribution of panels is generally neglected in the common structural analysis due to modeling complexity. However, internal force modifications caused by infill-frame interaction may be incompatible with the strength of surrounding frame elements, especially when additional shear forces arise at the end of beams and columns leading to unexpected brittle failures.

Micro-modeling and macro-modeling techniques are used for the finite element analysis of infilled frame structure. Different codes and regulations enforce the single equivalent diagonal compression strut approach to consider the elastic in-plane stiffness of the masonry panel. However, the additional shear demand due to the frame-infill interaction cannot be evaluated using standard equivalent strut models, and the micro-modeling approach is too computationally demanding to be employed in practice. This leaves open the issue of determining the additional shear on columns and, as a result, selecting the appropriate eccentricity for the diagonal struts. This study aims to calibrate an equivalent three-struts macro-model and validate outcomes with refined micro-model and experimental data from the various literature to reach acceptable results both in global and local analyses. The outcome of this calibration study will determine the equivalent width of each strut and the position of the non-diagonal strut for maximum shear demands at the column ends of various case study tests. A genetic algorithm is used to find the optimum struts position to optimize both local and global response. When conducting seismic assessments of existing RC structures for practical applications, the findings of this research study can be conveniently applied to perform shear safety checks at the column's ends.

ACKNOWLEDGEMENT

I would like to express my sincere gratitude to the Department of Structural, Geotechnical and Building Engineering (DISEG), Politecnico di Torino for providing me with the opportunity to undertake the course Structure Engineering for Master of Science in Civil Engineering. The knowledge I gained has been invaluable in shaping my professional development and enhancing my academic knowledge.

Firstly, I would like to extend gratitude to my supervisor, Professor Fabio Di Trapani, for providing me with the opportunity to work with a group of passionate researchers who are entirely committed to their work. His enthusiasm, support, and insightful input have been extremely beneficial to my thesis research. His commitment and dedication were the main motivation to deal with the challenges.

Secondly, I express my gratitude to another Ph.D. scholar Ing. Marilisa Di Benedetto for her helpful guidance, and expertise, and for providing the necessary data and information to complete the thesis work. Despite her busy schedule, I am incredibly grateful for her invaluable time.

Additionally, I would also like to thank my co-supervisor the Ph.D. scholar Ing. Antonio Pio Sberna, for his unwavering support and mentorship at every step. His expertise has provided me with a unique perspective and has been instrumental in broadening my knowledge. I appreciate the time and effort invested in helping me navigate the challenges and opportunities presented during the thesis research.

In conclusion, I want to express my gratitude to everyone who supported and encouraged me to accomplish my master's degree. Everyone's advice and encouragement have been tremendous, and I do not doubt that the abilities and information I have acquired during my studies will serve my engineering work well in my future endeavours.

Sincerely,

Contents

ABSTRACT	i
ACKNOWLEDGEMENT	ii
Contents	iii
List of Table	v
List of Figure	vi
CHAPTER 1	1
Introduction	1
1.1 Background.....	1
1.2 Problem Statement.....	3
1.3 Objective of Study	5
1.4 Scope and Limitation.....	6
1.5 Framework of Thesis	7
CHAPTER 2	8
Literature Review	8
2.1 Overview of Infill Frames in Structural Engineering.....	8
2.2 Previous Research on Infill Wall Modeling	9
2.3 State of Art in Infill Analysis for Equivalent Strut Macro-models	13
CHAPTER 3	17
Methodology.....	17
3.1 Research outline	17
3.1.1 Fiber Elements and Material Model	17
3.1.2 Concrete Model Proposed by Kent and Park Model (1971)	21
3.1.3 Concrete Model Proposed by Mander Model (1971).....	22
3.1.4 Genetic Algorithm	25
3.2 Implementation of Multi-Strut Model in OpenSeesPy.....	27
3.3 Description of OpenSeesPy model.....	27
3.3.1 Number of dimensions and degree of freedom	28
3.3.2 Node	28
3.3.3 Constraints.....	28
3.3.4 Materials	28
3.3.5 Sections.....	29
3.3.6 Elements	30
3.4 Experimental Setup for Calibration Model	31
3.4.1 Experimental Details of Specimen S1A and S1B	32

3.4.2	Experimental Details of Specimens 5,6 and 11	34
3.4.3	Experimental Details of Specimen C1, L2 and N1	37
3.4.4	Experimental Details of Specimen TA2 and FIF	38
3.5	Influence of Masonry Property in Calibration.....	41
3.5.1	Masonry Details for Specimen S1A and S1B	43
3.5.2	Masonry Details for Specimen 5,6 and 11	43
3.5.3	Masonry Details for Specimen C1, L2 and N1	44
3.5.4	Masonry Details for Specimen TA2, FIF	45
3.6	Equivalent Strut Macro-modeling for Calibration.....	47
CHAPTER 4.....		51
Analysis of Selected Specimens		51
4.1	Gravity Load Analysis.....	51
4.2	Pushover Analysis	54
4.3	Evaluation of Numerical-Experimental Results Goodness	57
4.4	Optimization with Genetic Algorithm (GA)	59
CHAPTER 5.....		63
Calibration Result.....		63
5.1	Integrating Masonry Infill with the Macro-Model	63
5.2	Calibration with Experimental Data (Global Response) using GA.....	64
5.3	Calibration with Micro-Modal Analysis (Local Response) using GA	69
5.4	Validation of the Proposed Model.....	78
CHAPTER 6.....		90
Conclusion.....		90
6.1	Summary of Key Findings.....	90
6.2	Implications of Findings.....	91
6.3	Recommendations for Future Research.....	92
Appendix A. <i>Openseespy</i> code for the multi-strut macro model generation.....		93
Appendix B. <i>Openseespy</i> code for genetic algorithm (GA).....		101
Appendix C. <i>Openseespy</i> code for run and plot		103
References		105

List of Table

1. Geometric and typological details of reference specimens	40
2. Concrete and steel rebar properties of reference specimen	41
3. Mechanical properties of masonry for specimen S1A and S1B[16].	43
4. Average strength of masonry materials for specimen 5,6,11[28]	44
5. Average properties of the brick, mortar and masonry for specimen C1, L2 and N1	44
6. Average properties of the brick, mortar and masonry for specimen TA2, FIF	46
7. Geometrical, mechanical, stress-strain parameters and equivalent strut width of infills.	50
8. Gravity load and the dimension of frame for different specimens	51
9. Parameters that used in genetic algorithm for optimisation of the global and local response.....	62
10. Width of each strut and position of eccentric struts by GA.....	64
11. RMSD value of referenced specimen using GA	69
12. Maximum shear force comparison between micro model and GA macro modal	77
13. Updated weightage of each equivalent struts.....	79
14. Updated position of off-diagonal struts evaluated by empirical equation.....	80
15. GA and proposed modal error for global and local response	86
16. Referenced specimen fitness value for GA and proposed model	87

List of Figure

1. Equivalent Diagonal Strut of URM Infill Wall.	1
2. Schematization of the stresses arising from the infilled frame's (a) detachment of the edges and shear effect (b) Fracture caused by edge crushing.	2
3. Pillar failure occurs when shear stress rises because of masonry impacts' strut effect.	3
4. Macro model for infill frame (a) single equivalent strut (b) multi equivalent strut	4
5. Local shear failure at column ends of infilled RC frames.....	5
6. Different models of the frame infill interaction that use off-diagonal struts are proposed by (a) Srymakezis and Vratsanou (1986), (b) Zarnic and Tomazevic (1988), (c) Schmidt (1989), (d) Chrysostomou (1991), (e) El-Dakhakhni (2003).	10
7. The infill is represented by two equivalent struts, and the extremities' positions are defined [4].....	10
8. Fiber-section model for equivalent strut model.	12
9. Behaviour of frames under lateral loads (a) bare frame, predominant frame action(b) infilled predominant truss action.	14
10. Failure modes for infilled RC frames: (a) frame failure, sliding shear and diagonal cracking (b) corner crushing and diagonal compression.	15
11. Numerical approaches for infilled frames modeling.....	15
12. Idealized models of beam-column elements.	18
13. Non-linear displacement-based element.	20
14. Non-linear force-based element.....	20
15. Stress-Strain model for confined and unconfined concrete	21
16. Concrete confinement effective area by Mander et al.....	22
17. Stress-strain curve for the confined concrete.	24
18. Relation between a simulation model and GA optimization algorithm	26
19. Constitutive laws of the materials used to define the model (a) <i>concrete2</i> (b) <i>steel2</i>	29
20. Diagram of the fibre modeling of a reinforced concrete beam	29
21. Fibre modeling of a conventional beam or pillar in a confinement frame.....	30
22. S1A and S1B specimen details (measures in cm)	32
23. Test setup for specimen S1A and S1B[16]	33
24. Design of weak frame test specimen 5, $h/l = 0.67$ (measure in mm)	34
25. Design of strong frame test specimen 6, $h/l = 0.67$ (measure in mm)	35
26. Design of weak frame test specimen 11, $h/l = 0.48$ (measure in inch, 1 in. =25.4 mm)	36
27. Test setup for specimen 5,6,11 (1 in = 25.4 mm).....	36
28. RC frame dimension for specimen C1, L2, N1 (measured in cm).....	37
29. Reinforcement details of the RC frame for specimen TA2 (measured in cm)	38
30. Reinforcement details of the RC frame for specimen FIF (measured in mm)	39
31. Geometric details of masonry units for specimen 5,6,11	44
32. Detail of Masonry Unit for Specimen TA2 (measured in mm)	45
33. Brick units: (a) top view (b) side view and (c) arrangement of the masonry for specimen (FIF).....	46

34. Modeling scheme for the infilled frame.....	47
35. Elevation of vertical loading system.....	51
36. Gravity load (a) Mechanical and geometric features (b) <i>OpenSeesPy</i> model.....	52
37. Infilled frame subjected to lateral actions.....	55
38. Hydraulic jack for lateral load application	55
39. Lateral load applied incrementally throughout the pushover analysis.....	56
40. Experimental curves and average experimental curves for specimens (a) S1A (b) S1B	58
41. Experimental curves and average experimental curves for specimen (a) 5 (b) 6 (c) 11	58
42. Schematization of the infill by three equivalent struts and definition of the position.....	63
43. Experimental backbone curve and pushover curve by GA for specimens (a) S1A (b) S1B	66
44. Experimental backbone curve and pushover curve by GA for specimens (a) 5 (b) 6.....	66
45. Experimental backbone curve and pushover curve by GA for specimen 11.....	67
46. Experimental backbone curve and pushover curve by GA for specimens (a) C1 (b) L2.....	67
47. Experimental backbone curve and pushover curve by GA for specimen N1.....	68
48. Experimental backbone curve and pushover curve by GA for specimens (a) TA2 (b) FIF	68
49. Identifying section cuts and predicting shear demand at infilled frame columns.....	70
50. Micro-model analysis; damage pattern on infilled-frame specimen (a) S1A (b) S1B	71
51. Shear demand calibration of macro model-GA with micro-model at column ends: S1A.....	71
52. Shear demand calibration of macro model-GA with micro-model at column ends: S1B.....	72
53. Micro-model analysis; damage pattern on infilled-frame specimen (a) 5 (b) 6.....	72
54. Micro-model analysis; damage pattern on infilled-frame specimen 11	73
55. Shear demand calibration of macro model-GA with micro-model at column ends: (a) 5 (b) 6 (c) 11	73
56. Micro-model analysis; damage pattern on infilled-frame specimen (a) C1 (b) L2 (c) N1.....	74
57. Shear demand calibration of macro model-GA with micro-model at column ends: (a) C1 (b) L2 (c) N1	75
58. Micro-model analysis; damage pattern on infilled-frame specimen (a) TA2 (b) FIF	76
59. Shear demand calibration of macro model-GA with micro-model at column ends: TA2.....	77
60. Shear demand calibration of macro model-GA with micro-model at column ends: FIF	77
61. Relationship between strut weightage and the aspect ratio of the RC frame.....	78
62. Non-diagonal struts position discrepancy between GA and proposed analytical equation.....	800
63. Validation of proposed model for specimen S1A (a) struts-frame orientation (b) global response (c) local response.....	81
64. Validation of proposed model for specimen S1B (a) struts-frame orientation (b) global response ..	81
65. Validation of proposed model for specimen S1B local response	82
66. Validation of proposed model for specimen FIF (a) struts-frame orientation (b) global response (c) local response.....	82
67. Validation of proposed model for specimen 5 (a) struts-frame orientation (b) global response (c) local response.....	83

68. Validation of proposed model for specimen 6 (a) struts-frame orientation (b) global response	83
69. Validation of proposed model for specimen 6 local response	84
70. Validation of proposed model for specimen TA2 (a) struts-frame orientation (b) global response (c) local response	84
71. Validation of proposed model for specimen L2 (a) struts-frame orientation (b) global response	84
72. Validation of proposed model for specimen L2 local response.....	85
73. Validation of proposed model for specimen N1 (a) struts-frame orientation (b) global response (c) local response.....	85
74. Validation of proposed model for specimen 11 (a) struts-frame orientation (b) global response	85
75. Validation of proposed model for specimen 11 local response	86
76. Histogram: error between GA and proposed model for global response	88
77 . Histogram: error between GA and proposed model for local response on windward column.....	88
78. Histogram: error between GA and proposed model for local response on leeward column.....	89

CHAPTER 1

Introduction

1.1 Background

Reinforced concrete (RC) became the most common construction material for the building's construction after the invention of Portland cement in the 19th century. This construction material has been rapidly increased in all the regions of developing and developed countries because of its strength, durability, versatility, availability of raw materials, low maintenance, and good seismic performance. The versatility of this building material simplifies the construction of the building's structural units like slab, beam, column, and foundation. To enclose and partition the building several techniques and materials can be used, and brick masonry is the most used technique because of the flexibility and availability of construction materials (brick, cement, sand, water). Although brick masonry infills are considered non-structural elements within the beam-column frame structure, they improve the performance of the structure under earthquake load[1].

Masonry infills are usually ignored by engineers while conducting structural analyses of buildings, just considering them as dead loads in the frame because they lack sufficient understanding of the behaviour of infill and frame composites, as well as the variability of material properties concerning different geometric configurations and construction techniques. According to FEMA 356 (Section 7.5.2), a solid unreinforced masonry infill (URM) panel prior to cracking shall be represented with an equivalent diagonal compression strut of calculated design width [Figure 1] which is useful for finite element programs to analyse masonry infills within the frames[2].

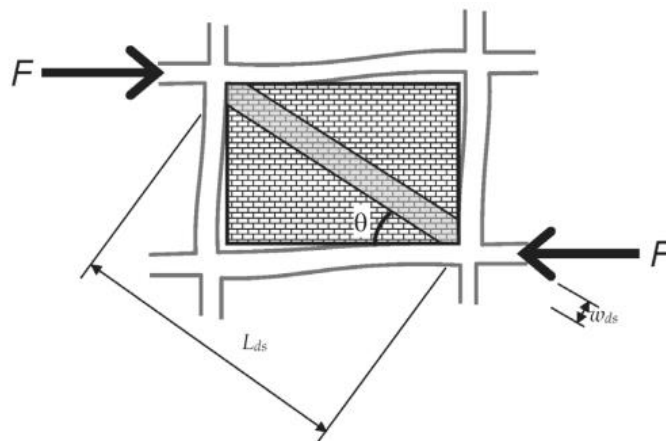


Figure 1. Equivalent Diagonal Strut of URM Infill Wall.

The interaction between reinforced concrete (RC) frames and masonry panel, cause potential damage due to the interaction between surrounding frame and the infill. The brick wall, which is more rigid than the RC frame, is often the first to be damaged. There are essentially three types of damage to masonry, which can be summarised as cracking diagonally, sliding horizontally along mortar joints and crushing edges. In certain situations, the compressive loads are so high that they cause the pillar to shear as well as cause the masonry to break. In fact, the existence of infills increases the pressures on the structure during seismic events, especially increasing demand cutting on the pillar. This occurs because of the compressive force that develops inside the diagonal connecting rods having to release onto the frame. However, this masonry connecting rod's width is limited because it only recalls the area of the frame next to the infill's diagonal; numerous modelling examples in the literature take advantage of this equivalent strut, and each of them suggests a different method for determining the previously mentioned connecting rods' widths. As we move away from the node, tensions along this region consequently build up and eventually tend to decrease. These tensions are released on the pillar as well as the beam [Figure 2].

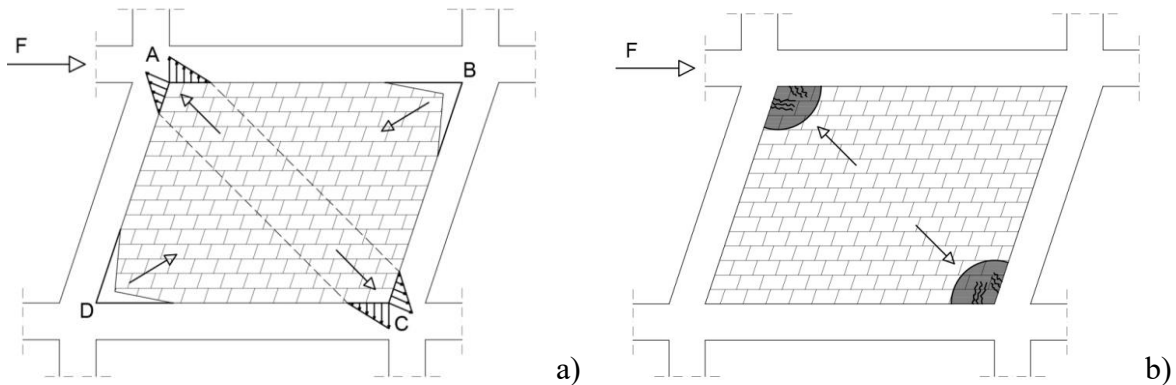


Figure 2. Schematization of the stresses arising from the infilled frame's (a) detachment of the edges and shear effect (b) Fracture caused by edge crushing.

Tension on the beam's edge increases shear stress, bending moment, and normal stress in the pillar. Instead, applying tension to the pillar's edge causes an increase in the column's shear stress, bending moment, and normal stress in the beam. The force increases connected to column shear forces are the ones that should worry us the most. As we can see in Figure 3,

under the worst circumstances, this can cause shear failure of the column, that could lead to a brittle collapse of the structure.

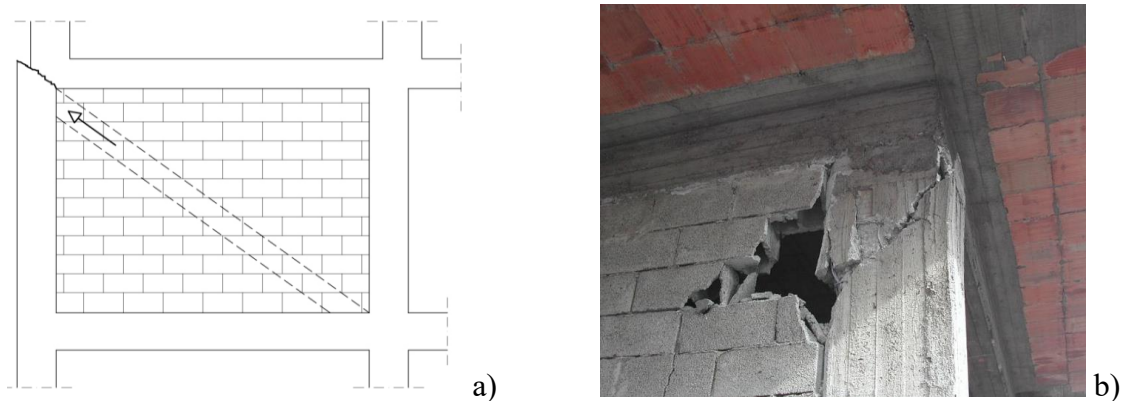


Figure 3. Pillar failure occurs when shear stress rises because of masonry impacts' strut effect [27].

1.2 Problem Statement

Frame-infills received a lot of interest in the past, and a lot of research has been done to do adequate structural evaluations and predict the effects of infill on the frame. The research study on the infilled frame can be categorized into three ways, the first one is the experimental investigation and the other two are micro-modeling and macro-modeling which is an analytical investigation based on the results of experimental research. The micro model is also known as the finite element model able to capture the failure mechanism of the masonry, mortar-masonry units' interface, and infill frame interaction. Macro-model represents the infill masonry as nonlinear struts of equivalent width which have been calibrated with the micro-model to capture the frame-infill interaction.

Despite more than 60 years of research into the impact of masonry infills on the seismic performance of frame structures, theoretical findings and simplified computational models proposed by various authors are rarely used in practical engineering, nor are mandatory prescriptions and detailed recommendations provided by most technical codes. However, a review of previous and recent literature on the topic reveals that this is not entirely surprising[3]. Eurocode 8 (ENV version) suggests calculating the fundamental period of an infilled structure as the average of the fundamental periods of the bare and infilled structures, it also suggests two approximated techniques to derive the fundamental period. The following Eurocode versions remove the indications about the stiffening effect of infilled panels because the increased strength due to infills usually compensates for the consequences of increasing seismic forces[4].

Macro-modeling of the infills can be done by equivalent single-strut Figure 4(a) and multi-strut model Figure 4(b). FEMA 356, Par. 7.5.2.1 recommends Eq. (1-2) for the calculation of masonry infill in-plane stiffness and strength based on the single-strut macro model. For a concrete frame with masonry infills that will crack when subjected to design lateral forces, the response can be represented by using a diagonally braced single-strut frame model, in which the infill acts as an equivalent compression strut having width 'a'.

$$a = 0.175(\lambda_1 h_{col})^{-0.4} r_{inf} \quad (1)$$

$$\lambda_1 = \left[\frac{E_{me} t_{inf} \sin 2\theta}{4E_{fe} I_{col} h_{inf}} \right]^{\frac{1}{4}} \quad (2)$$

where h_{col} is the column height between centrelines of beams; h_{inf} is the height of infill panel; E_{fe} is the expected modulus of elasticity of frame material; E_{me} is the expected modulus of elasticity of infill material; I_{col} is the moment of inertia of the column; θ is the angle whose tangent is the infill height-to-length aspect ratio; t_{inf} is the thickness of infill panel and equivalent strut; r_{inf} is the diagonal length of infill panel; λ_1 is the coefficient used to determine the equivalent width of the infill strut.

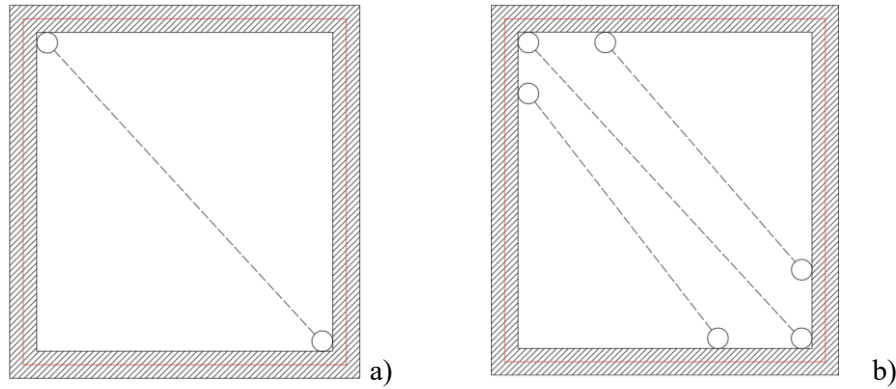


Figure 4. Macro model for infill frame (a) single equivalent strut (b) multi equivalent strut

An equivalent single-strut model is able to capture only the global response of the concrete frame with masonry infills suitably representing the strength, stiffness, and deformation capacity of beam, column, and beam-column joints. Besides stiffening and strengthening effects, the multi-strut model can evaluate local increments of shear demand on column and beam by means of an eccentric positioning of two strut elements[4]. Under seismic loads, the infill-frame interface exhibits highly nonlinear behaviour and is prone to shear collapse [Figure 5]. Making precise modeling for the measurement of internal forces, as well as an accurate prediction of potential local shear failures, is still an object of investigation[5].



Figure 5. Local shear failure at column ends of infilled RC frames [5].

1.3 Objective of Study

The main objective of this study is the calibration of a multi-strut model for the analysis of building structures integrated with masonry infill frames which could match both the global and local effects. Multi-strut model is a more accurate approach that consider the multiple equivalent struts within the frame structure placed eccentrically to represent the complex distribution of force in the frame structure due to masonry infills on the lateral loads. The concentric equivalent single-strut model is not able to accurately model the shear demand on the beam-column of the frame structures. This type of model is limited to determining the load-carrying capacity of the infill-frame, which is used to determine how the structure responds to applied loads and the corresponding displacements. To account for the local effects caused by the interaction between the frame structure and the infill, the equivalent single-strut model has been modified to an eccentric equivalent multi-strut model.

This study aims to calibrate and validate the equivalent multi-strut macro-model based on the Finite Element micro-model results validated with experimental data from the various literature research. Three equivalent struts are proposed for the numerically based macro-model analysis to assess both the global response of the structure and the local shear demand at columns' ends. The proposed three equivalent struts are positioned in such a way that the maximum shear demand of the column end and the global behaviour of the infilled frame could be comparable with the ones evaluated with the micro-modelling approach. The width and the mechanical property of the strut are evaluated from the proposed single strut model of the various literature. A genetic algorithm for the optimization of the positioning of the struts is implemented and used to both capture the global response and the local shear demand at columns' ends. A preliminary study, based on ten experimental tests, is provided for calibration of the proposed model, giving insight of some relationship of the position of the eccentric struts. Then the predictions provided for the positioning are used to calculate the error.

1.4 Scope and Limitation

Multi-strut macro-modeling of masonry infilled frames is a useful method for analysing the behaviour of RC frames, although it has certain limitations. Equivalent strut macro-models are the most effective technique for implementing the strengthening and stiffening effects offered by infills into structural models, overcoming the significant computational effort required by refined FE micromodels. Certain assumptions and simplifications related to material characteristics, structural behaviour, and loading conditions may be required while developing a macro-model. These assumptions may introduce uncertainty and limitations when predicting the structure's actual response. Therefore, a thorough micro model finite element analysis or comparison with experimental data are needed to validate the accuracy of the macro model.

Single-strut models are more computationally efficient than multi-strut models because they require fewer elements and simplifications. This efficiency can be useful for conducting rapid analysis and parametric investigations. Despite this, single strut models fail to reproduce exactly the physical characteristics of the real systems, and as a result, they may neglect essential information such as local shear transfer in contact regions. As a result, many complicated macro-models based on the number of non-diagonal struts were presented, with the primary advantage of accurately capturing the real behaviour of the infill panel when subjected to seismic forces. Multi-strut models are able to capture local shear demand, but they are too sensitive to the positioning of the struts, and it may affect the response of the structure at the local level.

By simulating different loading scenarios and failure mechanisms, multi strut macro models can aid in risk assessment and mitigation strategies which lead to identify potential failure modes and develop proactive measures to enhance the safety and resilience of the structure. In summary, while a multi-strut macro model masonry infilled reinforced concrete frame is an effective tool for analysing and optimising structural behaviour, it has limits in terms of modeling complexity, validation needs, and application. These variables must be carefully considered to ensure that the instrument used in structural engineering practice is accurate and dependable.

1.5 Framework of Thesis

This thesis includes six chapters. The first Chapter is related to the background, problem statement, objective of study, scope, and limitations. A literature review is done in the second chapter which contains the overview of infill frames, previous research and findings, state of art in infill analysis and current challenges and gaps in multi-strut modeling.

In the third chapter is presented the methodology for research design. *OpenSees* (The Open System for Earthquake Engineering Simulation (McKenna (1997))) software was used for modeling of reinforced concrete frames with infills. Implementation of multi-strut model in *OpenSeesPy* is defined with discription of *OpenSeesPy* model. The experimental setup for calibration model is described for all the referenced specimens. Masonry details for all the referenced specimens and influence of it in the RC frame are reported. The sample calculation of equivalent strut width and the mechanical, stress-strain parameters are shown in this chapter.

Chapter four contains the modelling strategy and the analysis of multi-strut macro-models subjected to monotonic loading, implementing pushover analysis on the selected specimens. To capture the global effect and the local effect an optimization tool is implemented with Genetic Algorithm (GA). By doing so the position of the struts are optimized to have a good agreement between the results obtained by the micro-models and the ones obtained by the proposed macro-models, in terms of global response and local shear demand at column ends. The discrepancy between the experimental pushover data and three strut macro-model data is determined by the goodness function RMSD. Optimisation tool Genetic Algorithm (GA) is described in detail.

Macro-model results are validated with the experimental data for global response and with micro-model analysis for local response. Summary of key finding of this research study is summarized in chapter 6 which also include the implication of finding and the recommendation for further research.

In Chapter 6 conclusions and discussions of the results are summarized.

CHAPTER 2

Literature Review

2.1 Overview of Infill Frames in Structural Engineering

The interaction between the masonry wall and frame structure involves both global and local behaviour, there is a strong connection between these two structural elements. A post-earthquake examination of the structures showed that the presence of masonry infill walls might have either positive or negative impacts on the structure. The negative consequences on the building induced by the masonry infill on earthquake load are plan or vertical irregularities[6], soft-storey mechanism[7] and short-column mechanism[8]. The flexural plastic hinges typical of the bare frame are replaced by the equivalent of a box structure composed of braced frames, whose deformation is controlled by infill shear behaviour[9]. Hence, Global stiffness increases in the frame structure due to infill wall bracing. The existence of infills is typically associated with a large increase in total structural stiffness implied by the infills, and then a higher natural frequency of vibration, which relies on the relevant seismic spectrum, might lead to an increase in seismic forces. Many investigations in the literature have been dedicated to characterising the infill frame interaction and determining the infill structural features. The influence of infill walls inside the frame is often described by modeling them as equivalent diagonal struts.

When an infilled frame experiences in-plane loading, the infills, and the frame members work together to create a combined resistance to the load, with the infills deforming mostly due to in-plane shear and direct stresses and the members primarily deforming due to bending and axial stresses[10]. Polyakov proposed modeling the infill panel as an equivalent diagonal compression strut. Holmes discovered that the most effective approach for determining the strength and stiffness of the infilled frame was to use an equivalent strut with dimensions equal to the actual panel material's modulus, thickness, and width, and one-third of the panel's diagonal length. Stafford Smith improved this method even further and initiated a series of tests to more precisely determine the equivalent strut's width[11]. The single equivalent diagonal strut model is simple to use and suitable for demonstrating the masonry panel's overall impact. However, the local effects brought about by the interaction of the surrounding frames and the infill panel are beyond the scope of this model. Because of this, some researchers modified the single strut model to get a simplified technique that can capture the local effect in the frame caused by infill frame interaction.

2.2 Previous Research on Infill Wall Modeling

Infill-frame interaction has been interest of researchers and engineers for over five decades. Many experiments and studies have been conducted to develop numerical models that can anticipate this interaction by addressing the reaction of the infilled frames when subjected to lateral loads on their plane. Research is focused on how masonry infills behave and hold up against both in-plane and out-of-plane forces. Various researchers have proposed methods for calculating the effective width of the diagonal strut based on experimental results to address the impact of the effective width value on the stiffness and strength of the strut representing the infill. Stafford-Smith (1962) presented the findings of their mortar panel studies as a curve that connects the effective width of the strut model to the aspect ratio (l'/h') of the infill panel[12]. An analytical method was developed by Stafford-Smith and Carter (1969) to determine the effective width of the strut, as well as the crushing and cracking loads, based on the contact length between the frame and infill in its deformed shape[13].

The equivalent diagonal strut approach can model the infilled frame's global force-displacement behaviour, but it cannot model the masonry panel and frame interaction in a local sense, specifically the change in the moment and shear diagram along the column length caused by the presence of the panel. With models that differ in number of struts and orientation, some researchers have attempted to enhance the infill-frame interaction. One of the initial attempts to consider this infill-frame interaction was made by Syrmakezis and Vratsanou (1986) [Figure 6(a)] utilising five parallel compressive struts in each direction. Zarnic and Tomazevic (1988) tried to take this infill-frame interaction into account by shifting the struts' orientation. They created a comparable compressive strut model, as illustrated in Figure. 6(b), in which the strut is offset from the diagonal. This model uses the outcomes of numerous cyclic experiments carried out on RC frames that were filled with infill. By combining the concepts of off-diagonal struts and adding more struts, Schmidt (1989) proposed a strut model that has offsets at both ends, as seen in Figure 6(c). Using three parallel compressive struts one diagonal and two off-diagonal in each direction. Chrysostomou (1991) further modified the strut orientation to replicate the infill panel's reaction, as seen in Figure 6(d). The complexity and computing effort, however, grow. El-Dakhakhni et al. (2003) recently developed a model with three non-parallel struts, as shown in Figure 6(e), to reproduce the proper moment diagram of columns in an infilled frame due to masonry-frame interaction and to adequately capture the corner crushing failure

mechanism. By increasing the number of points linking the infill panel to the columns or modifying the location at which the infill transfers load to the columns, all these models can more precisely describe the interaction between the infill and frame[14].

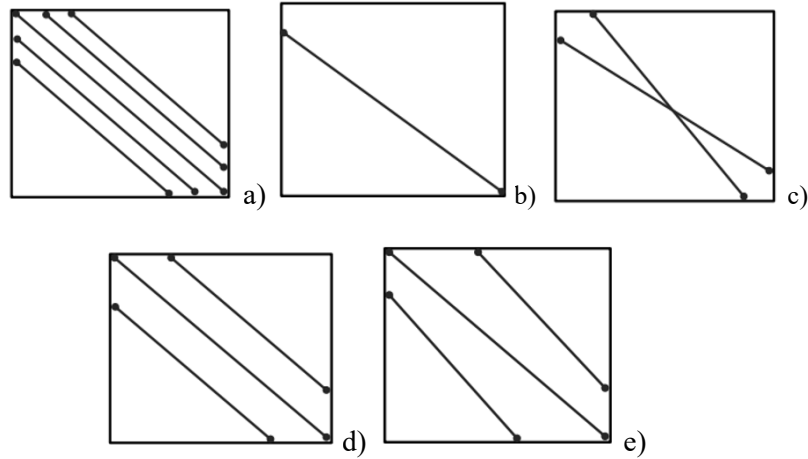


Figure 6. Different models of the frame infill interaction that use off-diagonal struts are proposed by (a) Symakezis and Vratsanou (1986), (b) Zarnic and Tomazevic (1988), (c) Schmidt (1989), (d) Chrysostomou (1991), (e) El-Dakhkhni (2003) [14].

Fiore et al. (2012) studied the effect of infills in the global (stiffness) and local response (effect on the frame) of RC buildings on the seismic loads. They proposed two non-parallel equivalent struts [Figure 7] of equally divided width whose position is expressed in function of the aspect ratio of the panel. They proposed the following expression to obtain the node position of two non-parallel strut. This method is validated by comparing with the experimental literature data and suitable Finite Element models under vertical and lateral loads[4].

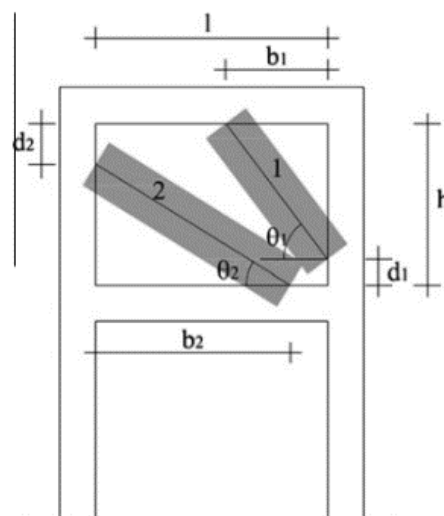


Figure 7. The infill is represented by two equivalent struts, and the extremities' positions are defined [4].

The position of strut-1 is expressed by eq. 3 and strut-2 by eq. 4.

$$d_1 = h * \left(0.10834 \left(\frac{l}{h} \right)^{-1} + 0.0073141 \left(\frac{l}{h} \right)^2 \right)$$

$$b_1 = l * \left(0.48689 \left(\frac{l}{h} \right)^{-2} + 0.16302 \left(\frac{l}{h} \right)^{0.5} \right) \quad (3)$$

$$d_2 = h * \left(0.157621 \left(\frac{l}{h} \right)^{-1} + 0.084484 \left(\frac{l}{h} \right)^{0.5} \right)$$

$$b_2 = l * \left(0.408621 \left(\frac{l}{h} \right)^{-0.5} + 0.44431 \left(\frac{l}{h} \right)^{0.5} \right) \quad (4)$$

The influence of masonry infill panels on seismic performance of reinforced concrete frames was studied by Mehrabi et al (1996). They considered two types of frames: one was designed for wind load and the other for strong earthquake forces. They tested twelve ½ scale, single-storey, single-bay, framed specimens. The influence of the frame aspect ratio and vertical load distribution on the lateral resistance of infilled frames was examined. Material tests were conducted on the reinforcing steel, and concrete and masonry samples for each infilled frame specimen. Investigated parameters included the panel aspect ratio, the distribution of vertical loads, the history of lateral loads, and the strength of the infill panels in relation to the enclosing frame. Based on the experimental results, it can be concluded that RC frames perform much better with infill panels. But in terms of load resistance and energy dissipation capacity, specimens with strong frames and strong panels performed better than those with weak frames and weak panels[15].

In order to demonstrate the impact of infill panels on strength, stiffness, and ductility, L. Cavaleri and F. Di Trapani (2014) carried out an experimental campaign on the cyclic response of RC completely infilled frames arranged with three different types of masonry infills. Calcarene masonry, Clay masonry, and Lightweight concrete masonry are used for infill panels and ordinary, lateral, and diagonal compressive experimental tests were carried out in order to assess their mechanical properties. The experiment was conducted on the infill-frame by subjecting the axial vertical constant load 200 kN on each column by hollow hydraulic jacks and lateral loads were applied by a horizontal double-acting jack. Using a transducer, the displacements at the top of each specimen were determined. Throughout the testing, damage mechanisms were observed to look for the spread of cracks on infills and frames. Stiffness, strength, and ductility evaluations were carried out. Both frames and infills were affected by crack propagation. First, about diagonal cracks appeared on frames near the higher joints near the columns. These cracks highlighted the joints' weakness in relation

to the strength of the most critical sections of columns and beams. This is usual in the existing structures; however, joints maintained the capacity to reciprocally transmit stresses from one RC member to another and from infill to RC members. In terms of modeling what was observed, when the strategy of infill substitution with an equivalent strut was used. Infills were primarily impacted by mortar joints and diagonal cracks that matched those at the beam-column joints. Consequently, the observed behaviour was successfully modeled by assuming the development of plastic hinges at the column ends and calibrating a corresponding strut that could correspond with the global phenomenon[16].

Di Trapani et al. (2018) conduct the assessment of inelastic response of infilled frames. Mechanical methods for analysing a strut's force-displacement curve were used, and they are based on assuming the damage mechanism that will occur in an infill-frame system subjected to lateral forces. A new stress-strain relationship is used for fiber-section modeling of equivalent struts [Figure 8]. Four parameters peak stress (f_{md0}), peak strain (ϵ_{md0}), ultimate stress (f_{mdu}) and ultimate strain (ϵ_{mdu}) define the stress-strain law which directly linked to geometrical and mechanical features of an infilled frame through analytical correlation laws. The identification of the equivalent strut cross-section geometry can be found by the procedure proposed by Asteris et al. (2016 a). The thickness (t) of the strut is equal to the actual thickness of the infill and the width (w) can be evaluated by the following semiempirical relationship[3].

$$w = k^\gamma \left(\frac{h}{l}\right) \frac{c^*}{\lambda^* \beta^*} d \quad (5)$$

where, h and l = actual length and height of the masonry panel; d = length of the equivalent diagonal strut; and κ = coefficient used to account for the lateral stiffening effect exerted by vertical load.

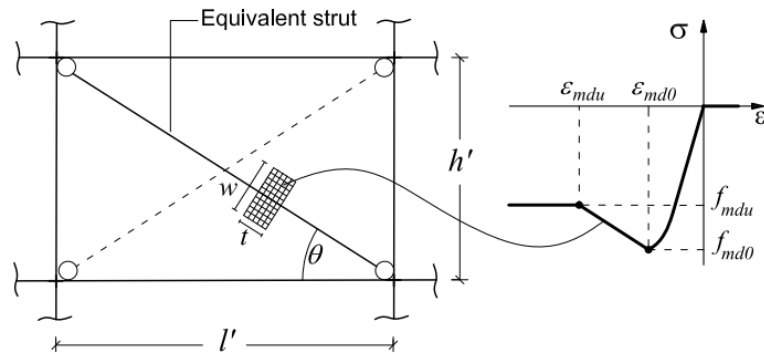


Figure 8. Fiber-section model for equivalent strut model [3].

Di Trapani et al. (2023) studied infill-frame interaction on refined modeling for the analysis and the estimation of the internal forces in seismic assessment of RC building structures. The study was based on the shear demand of the column due to infill. A refined micro-model for the infilled frame was formulated and realized with Open-Sees/STKO. The model validity was tested with four infilled frame specimens. Additional shear demand to the current axial force acting on the equivalent struts and depends on the effective contact length of the infill with the frame. The proposed micro-model allowed for the evaluation of the internal force distribution over the frame via a Python script that allowed for the integration of nodal forces across a specific cross-section. There was also a proposal for an analytical predictive model to assess the increased shear demand when using the equivalent strut macro-modeling approach. Assuming contact length values in the range of 0.25l to 0.40l, preliminary comparisons of the shear demand derived from the micromodel with that estimated by the macro-model and corrected by the suggested analytical formulation showed rather excellent agreement. This method ensures accurate shear safety tests at the ends of the columns while retaining the simplicity of the corresponding strut technique[5].

2.3 State of Art in Infill Analysis for Equivalent Strut Macro-models

Infill-frame interaction is still an open subject in both research and engineering practice. In most cases, computational models used to forecast this interaction address the estimation of the response of the infilled frames when subjected to actions parallel to their plane. The examination of post-seismic damage has revealed that infills that have been weakened by in-plane operations may fail out-of-plane, increasing potential risks associated with earthquake scenarios. Understanding the interaction of masonry and frame is difficult because it of dependency on several parameters such as brick materials (clay, concrete, etc.), mortar mechanical properties, brick geometry (hollow or solid, etc.), workmanship quality, relative stiffness between the frame and the panel, and so on. Although they are often regarded as non-structural features in the building model, infills clearly affect the seismic behaviour of the frame. In a relatively flexible frame, the bare frame carries the vertical loads, the frame and the infill jointly carry the horizontal seismic loads, and the truss mechanism predominates in the infill [Figure 9]. Typically, the infill reacts in the direction between the top corner of the windward column and the lower corner of the leeward column. For considerable displacements, the infill and frame are mostly in touch in the above corners along also called contact lengths.

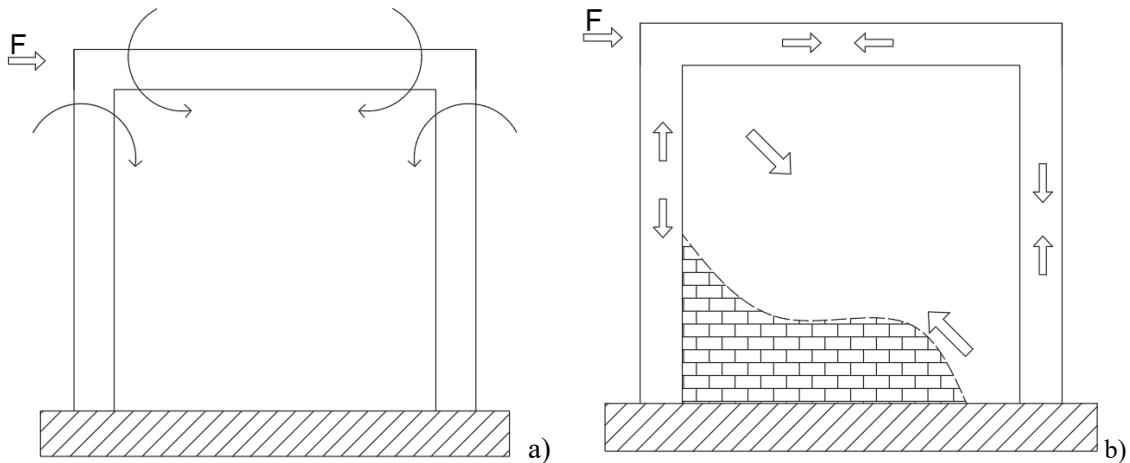


Figure 9. Behaviour of frames under lateral loads (a) bare frame, predominant frame action (b) infilled predominant truss action.

In the infilled frames, five unique in-plane failure mode are commonly found[17] and summarised as follows.

1. Frame failure mechanisms include the formation of plastic hinges in the beams and columns surrounding the joints, the failure of beam-column joints, and, in extreme cases, failure at column mid-height. Frame failure and infill failure may occur simultaneously [Figure 10(a)].
2. The panel encounters horizontal sliding across several bed joints in the infill sliding shear failure phase. It can happen when the mortar has weak mechanical qualities and the infill aspect ratio is extremely low, meaning that the truss action has a considerable horizontal component [Figure 10(a)].
3. Infill diagonal cracking failure mode, which is characterised by diffuse cracking along the panel compression diagonal and may occur when the frame is more flexible than the infill. It has a stepped diagonal design that runs down the mortar bed and the head joints. The cracking of the squeezed diagonal does not imply panel collapse, which may generate additional resisting ability. As a mixed mode, sliding shear and diagonal cracking may occur. [Figure 10(a)].
4. The panel centre is crushed because of the infill diagonal compression failure mechanism. This failure mechanism is most seen in narrow infills situated eccentrically with regard to the frame's axis, and it is accompanied by out-of-plane deformations and, finally, collapse. [Figure 10(b)].

5. Crushing at a loaded corner section of the infill panel owing to a biaxial compression condition is the failure mode of infill corner crushing. This is common when a weak infill panel is flanked by strong columns and beams with weak infill-joints at frame interfaces [Figure 10(b)].

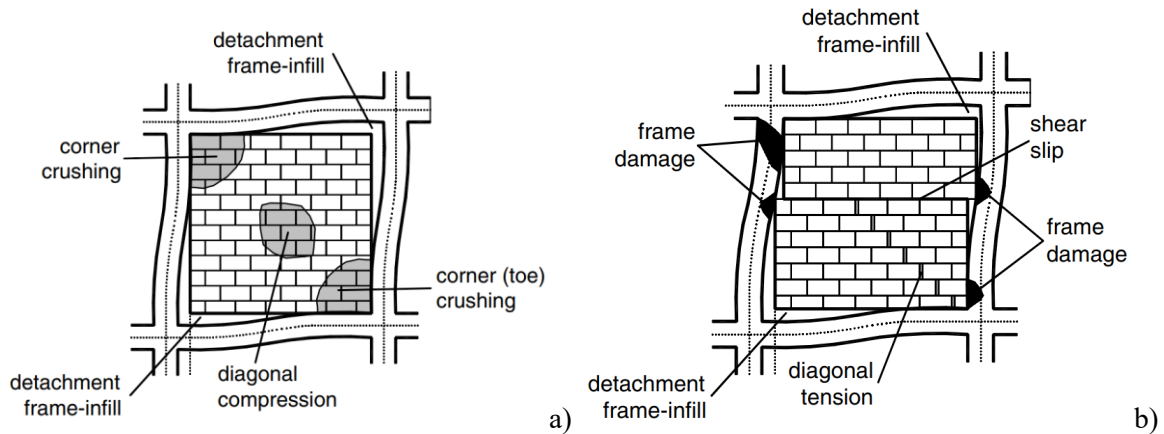


Figure 10. Failure modes for infilled RC frames: (a) frame failure, sliding shear and diagonal cracking (b) corner crushing and diagonal compression [17].

Numerous modeling approaches have been developed. These techniques are especially essential for the seismic evaluation and retrofit of existing RC structures. Infill frames modeling approaches are shown in the Figure 11.

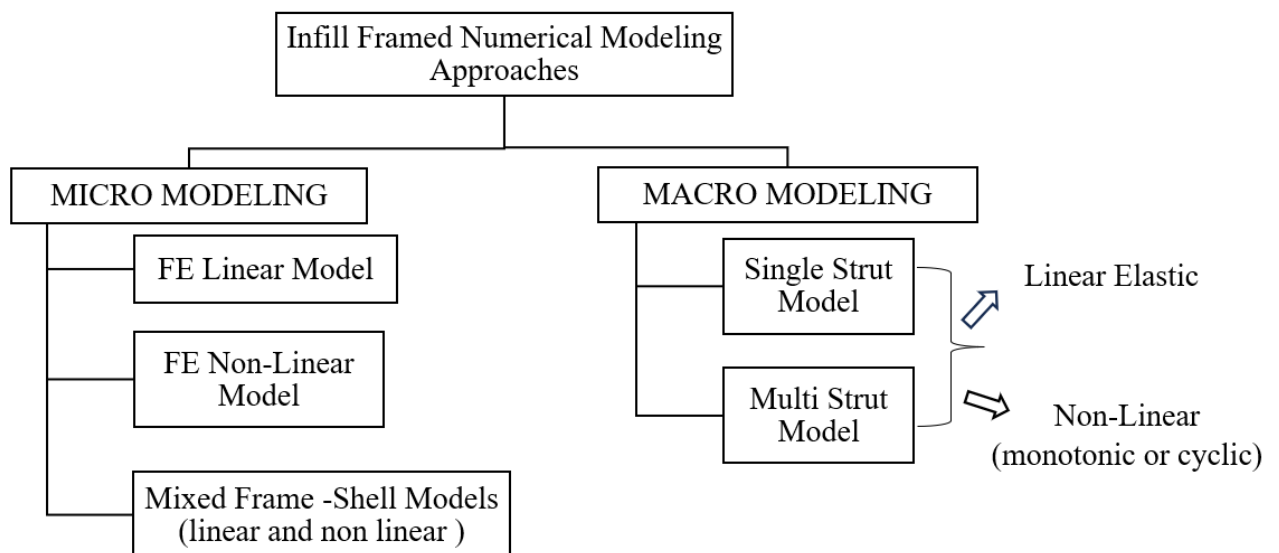


Figure 11. Numerical approaches for infilled frames modeling

More powerful computing platforms and faster computers have made it easier to build accurate micro-models over the previous two decades. This term refers to the detailed micro-modeling of each individual system part, such as the bricks and mortar layers of the masonry

infill panel or the concrete and reinforcement of the RC frame. FE micromodels are the most accurate method for capturing the frame-infill interaction, as well as the most similar to the real physics of the situation. Aside from stiffening effects, micromodels can accurately simulate complicated difficulties such as local frame-infill interaction, unit sliding along mortar joints, crack propagation on infills, and reinforced concrete sections using interface elements. Despite this advantage, they nonetheless face a twofold challenge. The first is a correct calibration, which can be extremely difficult to supply, needing knowledge of multiple factors and adequate experience to handle this type of modeling, especially in nonlinear circumstances. The second, and more important, factor is the high computing effort required. The application of micro-modeling to complicated structural systems is currently prohibitively expensive due to the long time required, limiting the usage of FE nonlinear micromodels to small case studies [18].

For monotonic loads, one strut along the compression diagonal is required, whereas cyclic loads normally require two struts along the two diagonals. The models proposed range from single to multiple struts, concentric to eccentric, linear elastic to non-linear hysteretic. The diagonal strut is often connected to the intersection sites of the beam and column centrelines. Single strut macro-models are the simplest technique to include the existence of infill panels into models in practical engineering. They are appropriate for complicated structure analysis and are simple to detect. Despite their simplicity, they can also provide a good approximation. Their fundamental limitation is the concentric configuration of the corresponding strut, which makes accounting for shear transmission in crucial components impossible. Although this concern may be less significant for structures with adequate shear reinforcement or weak infills, it becomes a very sensitive issue when non-seismically constructed buildings are examined. Multiple strut configurations can overcome this difficulty, but they are limited by uncertainties in calibration, particularly when doing nonlinear static or time history analysis[18].

CHAPTER 3

Methodology

3.1 Research outline

The research design for the study on the calibration of multi-strut macro models is exactly crafted to investigate the seismic performance and optimisation of multi-strut model frames with various infilled materials. The fundamental goal of this study is to improve calibrate and validate a multi-strut macro-model that accurately capture global and local effects. This could be essential for ensuring that macro models accurately reflect real structural behaviour. The research involves the utilization of advanced structural analysis software as *OenSeesPy* for modelling a dataset of ten experimental specimens under monotonic loads.

Seismic loading, performance evaluation, optimization using algorithms, validation against experimental data are integral components of the research design. A key component of the calibration design is experimental data, which can be obtained from previous research or from physical testing. The refined numerical micro-models are used in this research as a replica of the experimental tests. The high-fidelity micro-models (based on real tests) from Di Trapani & Di Benedetto work are selected to get the local shear demand on structural frame members. The multi-stut macro-models are implemented in this thesis work to reproduce the global and local response recorded in micro-models. Adjusting the model parameters iteratively helps minimise the discrepancies between the observed experimental data and the macro model's expected behaviour during the calibration phase. The model parameters are methodically adjusted using statistical analysis, and optimisation techniques. Until the numerical predictions and the experimental data agree to a reasonable degree, this iterative process is carried out. The research design's findings are important since a well-calibrated multi-strut macro model is a helpful predictive tool that allows engineers to quickly evaluate the seismic response both at a global and local level.

In next paragraphs an overview of the fundamental elements, physical constitutive laws and the optimization algorithm used for the proposed model are reported.

3.1.1 Fiber Elements and Material Model

When developing a structural model, it's important to consider the theory behind managing plasticity. Inelastic structural component models differ based on how plasticity is spread across member cross sections and length [Figure 12] compares five idealised models for

simulating the inelastic response of beam columns. Figure 12 illustrates how to represent various structural components, including beams, columns, braces, and flexural walls. Simple models concentrate inelastic deformations at the element's end, such as a rigid-plastic hinge [Figure 12(a)] or an inelastic spring with hysteretic characteristics [Figure 12(b)]. Concentrating the flexibility in zero-length hinges with moment-rotation model parameters allows for more efficient numerical formulations[19].

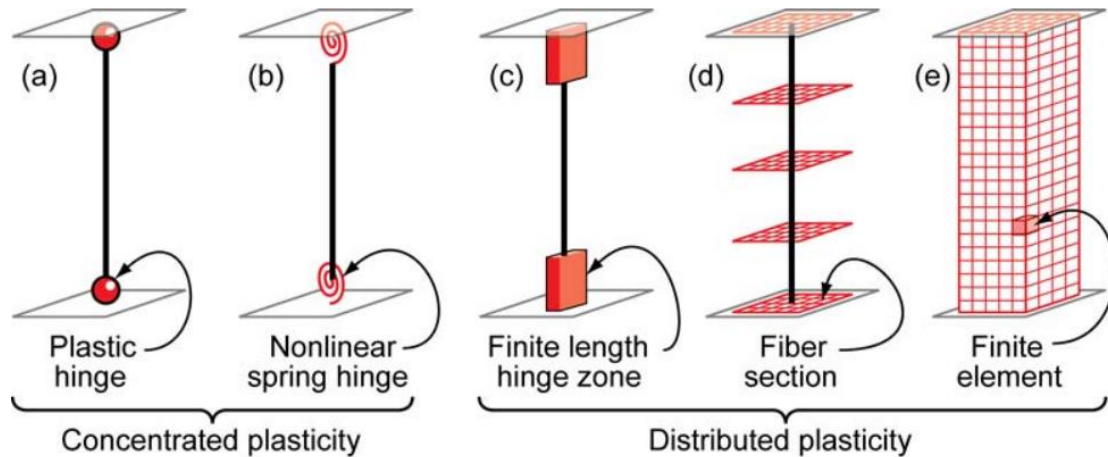


Figure 12. Idealized models of beam-column elements [19].

The finite length hinge model [Figure 12(c)] is a distributed plasticity formulation that includes hinge zones at the member ends. Cross sections in inelastic hinge zones are described using either nonlinear moment-curvature relationships or explicit fiber-section integrations that enforce the assumption that plane sections remain planar. The inelastic hinge length can be fixed or variable, depending on the section's moment curvature properties, contemporaneous moment gradient, and axial force. Integration of deformations along the hinge length captures the spread of yielding more realistically than concentrated hinges, although the finite hinge length simplifies hinge rotation calculation[19].

The fibre formulation [Figure 12(d)] uses numerical integrations to distribute plasticity across member cross sections and lengths. Uniaxial material models capture nonlinear, hysteretic axial stress-strain properties in cross-sections. The plane-sections-remain-plane assumption is enforced by statistically integrating uniaxial material "fibres" over the cross section to provide stress resultants (axial force and moments), incremental moment curvature, and axial force-strain equations. The cross-section parameters are numerically integrated at discrete member lengths using displacement or force interpolation methods. Distributed fibre formulas report strains in steel and concrete cross section fibres, not plastic

hinge rotations. Strain demands can vary based on moment gradient, element length, integration method, and strain hardening factors. Benchmarking the strain demands and acceptance criteria against concentrated hinge models, which have more publicly documented rotation acceptance criteria, is recommended[19].

Complex models [Figure 12(e)] discretize the continuum along member length and cross-sections into small finite elements with nonlinear hysteretic features and several input parameters. While this level of modeling is the most versatile, it also requires the most calibration and processing resources. Finite element stresses can be challenging to interpret in comparison to acceptance criteria based on hinge rotations and deformations, similar to fibre formulations[19].

The advantage of fibre elements is that they allow to analyse the cross-sectional response of the beam and how this influences the axial-deformation, moment curvature, and response of the beam. This is especially useful for composite cross-sections like those found in reinforced concrete beams and columns. We can consider various shapes, layouts, and material responses for the components. Because the drawback of fibre elements is insufficient to account for shear stresses, shear forces and torsion cannot be combined. It is only useful for accurately describing the reaction of slender flexure-dominated parts.

There are basically two types of non-linear fibre elements: Force Based Elements (FBE) and Displacement Based Elements (DBE). The classic finite element approach involves interpolating the element's deformation based on an approximate displacement field. Nodal forces are derived using the virtual works principle. To interpolate deformations, a linear shape function is employed for axial displacement and quadratic functions for transverse displacement. This results in a constant axial deformation and linear curvature. The shape functions are assessed using the exact solution of the Bernoulli beam equation.

- **Displacement-based element (DBE)**

The displacement-based technique employs standard finite element procedures, with section deformation interpolated from an approximate displacement field and the Principle of Virtual Displacement (PVD) used to build the element equilibrium relationship. Only prismatic linear elastic elements are subject to the approximate nonlinear element response, constant axial deformation, and linear curvature distribution over the element length [Figure 13]. To represent higher order deformation distributions, mesh refinement is required.

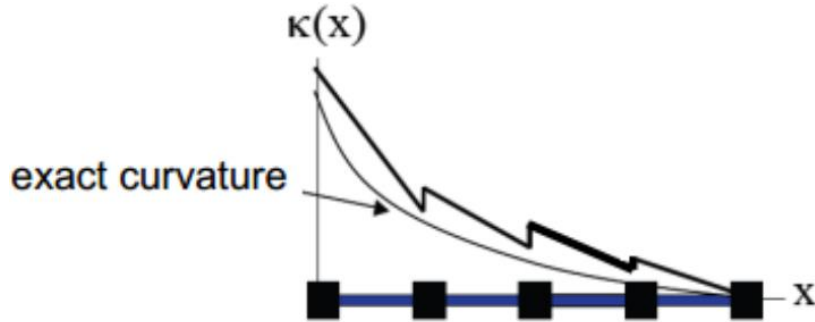


Figure 13. Non-linear displacement-based element.

- **Force-based element (FBE)**

The force-based technique relies on the existence of an accurate equilibrium solution within the basic system of a beam-column element. The equilibrium between element and section forces is accurately, which is valid within the range of constitutive nonlinearity. Section forces are derived from basic forces through interpolation inside the basic system. Interpolation is based on static equilibrium and provides constant axial force and linear bending moment distribution in the absence of distributed element loads [Figure 14]. Principle of virtual force (PVF) is used to determine compatibility between section and element deformations.

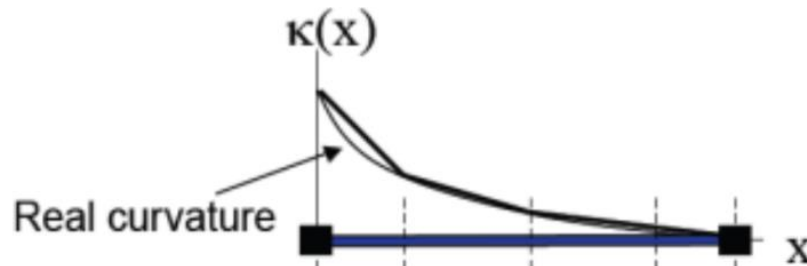


Figure 14. Non-linear force-based element

Difference between Displacement-based element (DBE) and Force-based element (FBE):

Displacement-based element (DBE)	Force-based element (FBE)
- Based on displacement shape functions.	-Based on internal force shape functions.
-Weak form of equilibrium is satisfied	-Strong form of equilibrium is satisfied
-Need several elements to describe inelastic behaviour of a beam column member accurately.	-Only one element per beam-column member is sufficient to represent inelastic behaviour.
-Discrepancies from exact solution can arise from both numerical integration errors and inaccurate shape functions.	-Discrepancies from exact solution can only arise from numerical integration errors.
-Gauss-Legendre is the commonly used integration method.	-Gauss-Lobatto is the commonly used integration method

3.1.2 Concrete Model Proposed by Kent and Park Model (1971)

In order to explain how concrete behaves under different loading scenarios, Kent and Park (1971) proposed a constitutive model. This model is especially well-known for its ability to represent the pre-peak and post-peak responses in concrete, as well as its nonlinear behaviour. It offers a mathematical expression for the concrete's stress-strain relationship during compression. The elastic section and the plastic segment make up the two segments of a bilinear stress-strain relationship, which is the foundation of the Kent and Park model [Figure 15].

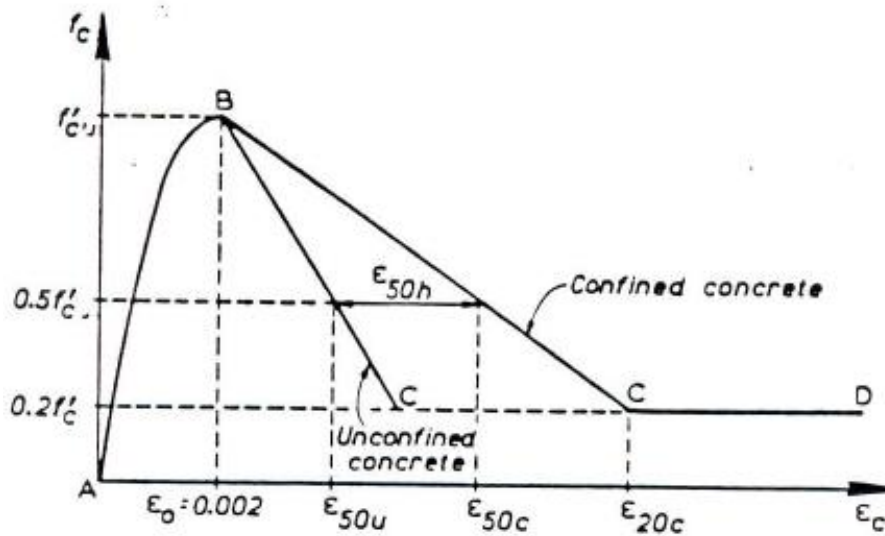


Figure 15. Stress-Strain model for confined and unconfined concrete [20].

The elastic segment exhibits a stress-strain relationship where stress (σ) is linearly proportional to strain (ϵ), as per Hooke's Law. The slope of this segment can be represented by the elastic modulus (E). When the strain threshold is exceeded, which usually corresponds to the peak stress, the behaviour shifts to the plastic segment. It is expected that the plastic segment's stress-strain relationship exhibits a power-law behaviour, with stress growing nonlinearly with strain. The strength degradation factor and the strain hardening ratio, for example, control the rate at which stress increases with strain [20].

The Kent and Park model is frequently used in finite element analysis and structural engineering to simulate the behaviour of concrete structures under a variety of loading circumstances, including static and dynamic loads, as well as earthquakes. It gives a simple yet effective method of capturing concrete's nonlinear behaviour, making it useful for analysing and constructing reinforced concrete buildings under realistic loading scenarios.

3.1.3 Concrete Model Proposed by Mander Model (1971)

One well-known issue with reinforced concrete beams is their flexural behaviour. The flexural behaviour of the reinforced concrete beams section can be simulated using a number of classical research on this topic; however, the concrete confinement is frequently ignored in these studies. Stirrups or rectilinear ties in reinforced concrete significantly improve strength and ductility. Under axial pressures, concrete pressure in the lateral direction of the sections acts on the lateral ties, and the links' resistance may limit the core of concrete to some extent. The mechanical behaviour of confined concrete is defined by an increase in strength and ductility. The size of the increase is determined by a variety of confinement characteristics, including the compressive strength of the concrete, the volumetric, the diameter, the configuration and strength of the ties, the ratio and diameter of the longitudinal bars, and the section geometry, among others. Mander et al. proposed a stress-strain relation of confined concrete with according the confinement effects to the various configurations of lateral ties. This model is built up of empirical relationships that describe the behaviour of constrained concrete. In the case of the rectangular section, when the axial stress increases from the earliest stages of loading, the concrete contracts longitudinally and expands laterally, resulting in internal micro fractures. The transversal reinforcement can withstand high expanded pressure, and good confinement of the by lateral ties increases the axial load-carrying capability. Figure 16 shows the effective limited area, which Mander et al. [21]. describe as:

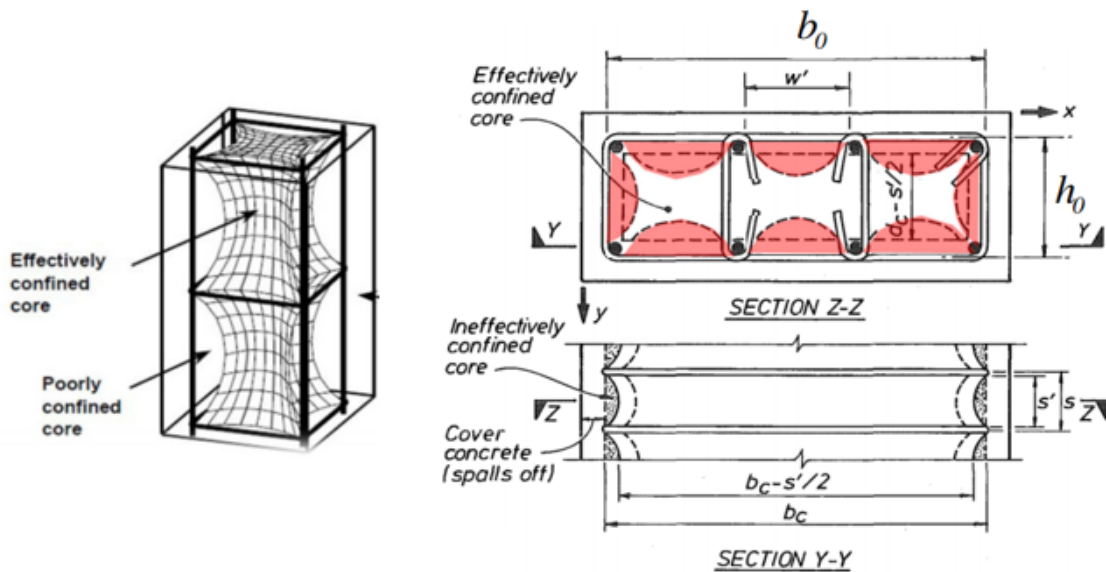


Figure 16. Concrete confinement effective area by Mander et al.

For one section with n bares, the unconfined area can be written as:

$$A_i = \sum_{i=1}^n \frac{(w'_i)^2}{6} \quad (5)$$

Confined concrete area is given by:

$$A_e = \left(b_0 h_0 - \sum_{i=1}^n \frac{(w_i)^2}{6} \right) \left(1 - \frac{s'}{2b_0} \right) \left(1 - \frac{s'}{2h_0} \right) \quad (6)$$

s': Internal distance between a successive longitudinal bares.

The confinement coefficient is defined as:

$$k_e = \frac{\left(1 - \sum_{i=1}^n \frac{w_i^2}{6b_0 h_0} \right) \left(1 - \frac{s'}{2b_0} \right) \left(1 - \frac{s'}{2h_0} \right)}{1 - \sigma_{cc}} \quad (7)$$

σ_{cc} : Confined concrete stress

Lateral pressures from x and y direction are defined by Mander and al given by:

$$f_{lex} = \rho_{sx} f_{yh} k_e \quad (8)$$

$$f_{ley} = \rho_{sy} f_{yh} k_e \quad (9)$$

ρ_{sx} : Volumetric ration of ties on x direction, ρ_{sy} : Volumetric ration of ties on y direction

f_{yh} : Yield strength of lateral ties.

Three coordinates can be used to predict the stress-strain curve of confined concrete. The coordinate $(\varepsilon_{cc0} - f_{cc})$ corresponding to the peak stress-strain, $(\varepsilon_{65} - 0.65f_{cc})$ corresponding to the representative point of the stress – strain curve at $0.65f_{cc}$ after the peak and $(\varepsilon_{ccu} - 0.65f_{cc})$ corresponding to the ultimate strain as shown by the Figure 17. In the ascending region between the zero and the first coordinate can be derived bay an equation based on the Sargin equation for unconfined concrete as:

$$\sigma_{cc} = f_{cc} \times \frac{k_c \times \bar{\varepsilon}_c + (k'_c - 1) \times \bar{\varepsilon}_c^2}{1 + (k_c - 2) \times \bar{\varepsilon}_c + k'_c \times \bar{\varepsilon}_c^2} \quad 0 \leq \varepsilon_c \leq \varepsilon_{cc0} \quad (10)$$

$$\text{Where: } \bar{\varepsilon}_c = \frac{\varepsilon_c}{\varepsilon_{cc0}} \quad \text{and } \varepsilon_{cc0} = \varepsilon_{c0} \times \left[1 + 5 \left(\frac{f_{cc}}{f_{c0}} - 1 \right) \right]$$

ε_c : Confined concrete strain

ε_{c0} : Unconfined concrete strain corresponding to the peak stress

ε_{cc0} : Confined concrete strain compounding to the peak stress

ε_{ccu} : Confined concrete ultimate strain

ε_{65} : The strain corresponding to the stress equal $0.65f_{cc}$.

The stress-strain relation of the descending part between the first and the second coordinates can be determined by:

$$\sigma_{cc} = f_{cc} - E_s(\varepsilon_c - \varepsilon_{cc0}) \text{ for: } \varepsilon_{cc0} < \varepsilon_c \leq \varepsilon_{65} \quad (11)$$

E_s : The slope of the descending curve and can be defined as:

$$E_s = \frac{6 \times f_{c0}^2}{k_e \times \rho_s \times f_y} \quad (12)$$

f_{c0} : Compressive strength of unconfined concrete.

ρ_s : Volumetric ration of ties.

And ε_{65} is the strain corresponding to the stress equal $0.65f_{cc}$. It can be defined by:

$$\varepsilon_{65} = \frac{0.35 \times f_{cc}}{E_s} + \varepsilon_{cc0} \quad (13)$$

After reaching the stress $0.65f_{cc}$, the stress of the confined concrete is a constant value $0.65f_{cc}$ regardless of the increasing strain until the ultimate strain (ε_{ccu}). The ultimate strain of confined concrete adopted in this study can be defined taking account the transverse reinforcement ultimate strain as:

$$\varepsilon_{ccu} = 0.4 \times \frac{f_l}{f_{c0}} + \varepsilon_{cu} = 0.0035 + 0.4 \times \frac{f_l}{f_{c0}} \quad (14)$$

f_l : Lateral confinement stress.

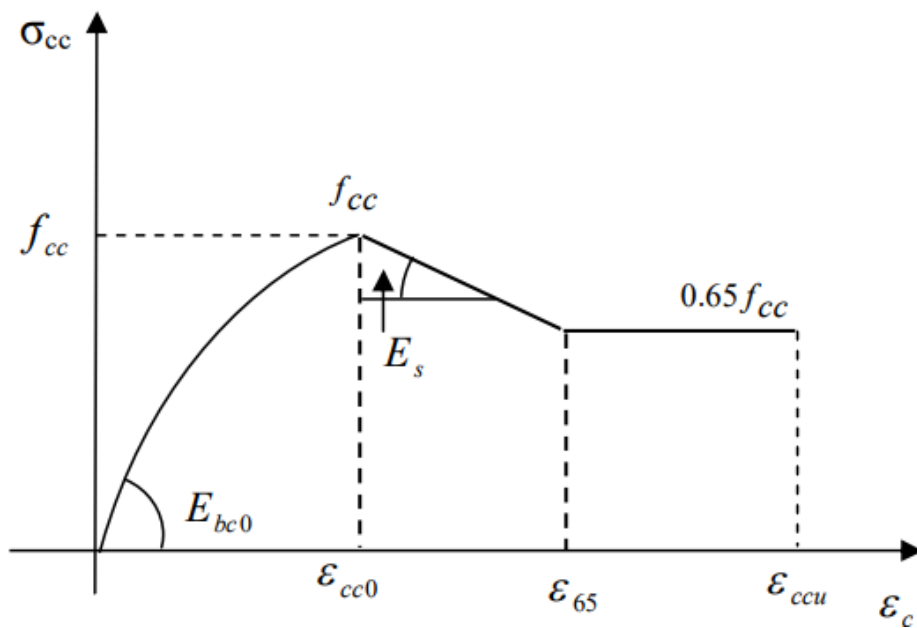


Figure 17. Stress-strain curve for the confined concrete.

3.1.4 Genetic Algorithm

A genetic algorithm (GA) is a kind of optimisation algorithm that receives inspiration from the concepts of genetics and natural selection. It is often utilised for modelling the process of natural selection to find approximations for solutions to optimisation and search problems. They were originally introduced by Holland at around the same time when other evolutionary methods were being developed and popularized by Goldberg's. They are characterized by the maintenance of a population of search points, rather than a single point, and the evolution of the system involves comparisons and interaction between the points in the population[22]. This typology of optimization method belongs to the class of Evolutionary Algorithm, the metaheuristic algorithm inspired to the Darwin's "evolution of specie" presented for the first time in the "On the Origin of Species by Means of Natural Selection" [23].

Genetic algorithms analogy seeks to find the optimal solution for a given problem. Whereas Darwinian evolution maintains a population of individual specimens, genetic algorithms maintain a population of candidate solution, called individuals, for that given problem. These candidate solutions are iteratively evaluated and used to create a new generation of solution. Those who are better at solving this problem have a greater chance of being selected and passing their qualities to the next generation of candidate solution. This way as generation goes by candidate solutions get better at solving the problem at hand [24] . The decision variables are inputs to the simulation model. Then, the state variables, which are outputs of the simulation model, are evaluated. Thereafter, the objective function is evaluated. In the next step, the problem constraints are determined, and lastly the fitness value of the current decision variables is calculated. At this time, the optimization algorithm generates a new possible solution of decision variables to continue the iterations if a termination criterion is not reached[25]. Figure 18 is illustrated the relation between the simulation model and the optimization algorithm.

The following outline summarizes how the genetic algorithm works[24]:

1. The algorithm begins by creating a random initial population.
2. The algorithm then creates a sequence of new populations. At each step, the algorithm uses the individuals in the current generation to create the next population. To create the new population, the algorithm performs the following steps:

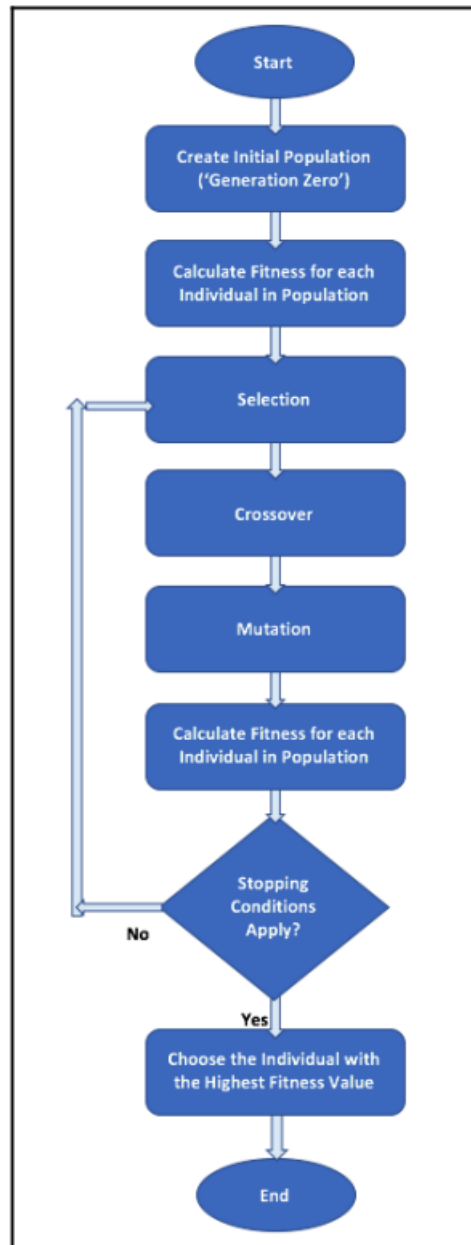


Figure 18. Relation between a simulation model and GA optimization algorithm [25]

- Scores each member of the current population by computing its fitness value. These values are called the raw fitness scores.
- Scales the raw fitness scores to convert them into a more usable range of values. These scaled values are called expectation values.
- Selects members, called parents, based on their expectation.
- Some of the individuals in the current population that have lower fitness are chosen as *elite*. These elite individuals are passed to the next population.

- e. Produces children from the parents. Children are produced either by making random changes to a single parent—*mutation*—or by combining the vector entries of a pair of parents—*crossover*.
- f. Replaces the current population with the children to form the next generation.
3. The algorithm stops when one of the stopping criteria is met.
4. The algorithm takes modified steps for linear and integer constraints.
5. The algorithm is further modified for nonlinear constraints.

3.2 Implementation of Multi-Strut Model in OpenSeesPy

The structural analyses were conducted using OpenSees software (Open System for Earthquake Engineering Simulation). PEER (Pacific Earthquake Engineering Research Centre) developed software with support from the National Science Foundation to analyse and simulate complex structural models to better understand their behaviour and performance during earthquakes. OpenSees is classified as open-source software, meaning it is fully free. The open-source approach and software architecture offer numerous advantages for users seeking to create accurate simulations of structural systems, including linear behaviour.

OpenSeesPy is a Python wrapper for *OpenSees*, a software framework used to simulate the behaviour of structural and geotechnical systems under earthquake conditions. This wrapper enables users to access *OpenSees* features via Python scripting, making it more accessible and user-friendly because of its huge library. *OpenSeesPy* allows users to construct complex structural models, apply different loading conditions, and analyse the reaction of structures to earthquakes and other dynamic loads. It offers a simple interface for researchers, engineers, and students to do complex structural analysis and study. *OpenSeesPy* allows users to define structural elements such as beams, columns, braces, and foundations. Specify material attributes such as stiffness, strength, and damping. Use boundary conditions such as supports, displacements, and loads. Analyse structural systems in static, dynamic, and nonlinear modes. Displacements, forces, and stresses are examples of extracted and visualised outcomes.

3.3 Description of OpenSeesPy model

In *OpenSeesPy*, a multi-strut model consists of building masonry components as equivalent struts, linking them to form the desired structural system, and then applying loads and

boundary conditions as required. Each strut element's behaviour can be determined by providing its attributes, including length, cross-sectional area, material qualities, and any other relevant data. This section will describe the *OpenSeesPy* based algorithm that contains the core model for our multi-strut frame model. The algorithm will be changed to meet future needs, as shown in the Appendix.

3.3.1 Number of dimensions and degree of freedom

The model will undergo in-plane analyses. The system described must have two dimensions. All nodes/elements will have three degrees of freedom. The software receives this information via the model command `basic`, which needs the definition of two values:

- `ndm` (number of dimensions) is equal to 2.
- `ndf` (number of degrees of freedom) is equal to 3.

3.3.2 Node

To define nodes, use the `node` command with a tag number and three coordinates (X, Y, and Z). We have to turn to the global reference system. To define these coordinates, we ensured that the infill plane was parallel to the X-Y plane. The Z axis is used to identify the direction out of plane.

3.3.3 Constraints

To define constraints, use the `fix` command with the desired node tag and six digits. Each of the six numerals represents a degree of freedom: DX, DY, DZ, RX, RY, and RZ (D represents movement and R represents rotation). Adding a 1 prevents a degree of freedom, while adding 0 leaves it free.

The numerous dynamic analyses that will be performed on the various models can be modified according to the necessity, the modification of the types of constraints that are imposed to the different model nodes. The study multi-strut model is 2D in-plane analysis, so considered degree of freedom is 3 and constraints along DX, DY, and RZ. Column connected with the foundation beam is constraint as fixed and one of the struts connected with the same foundation beam is constraints as roller support.

3.3.4 Materials

The materials are defined by the `unial` command. The material command is followed by the appropriate type of material and mechanical characteristics that describe the curve's trend in the σ - ϵ plane. Kent Park's constitutive link is described in previous paragraphs. Among

the materials accessible in the software library, *Concrete02* is the best fit for multi-strut model study. Figure 19 (a) depicts the constitutive law applicable to the *Concrete02* material. The *Concrete02* material was also used to distinguish between confined and unconfined concrete in the beams and pillars that comprise the reinforced concrete structure. In terms of reinforcement steel, *Steel02* was chosen as the material, and its simplified constitutive law (without the representation of the hysteresis loop) is presented in Figure 19(b).

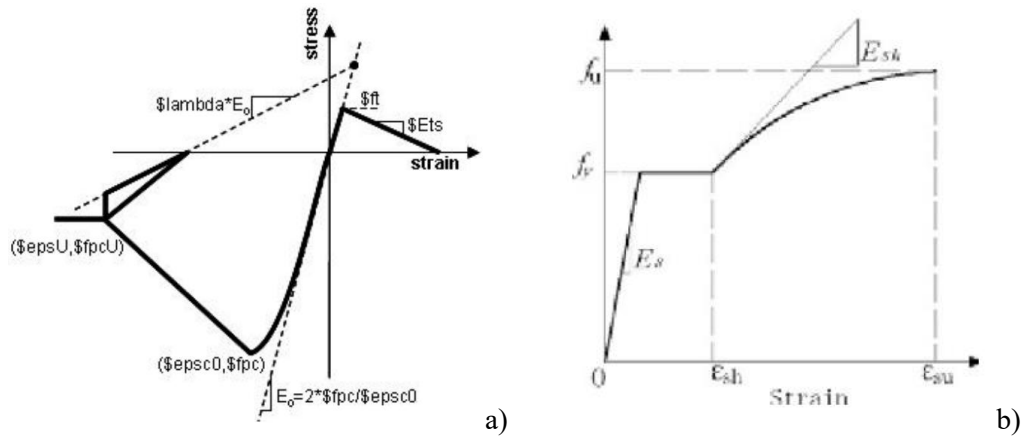


Figure 19. Constitutive laws of the materials used to define the model (a) *concrete2* (b) *steel2* [28]

3.3.5 Sections

To specify the fibre sections of different items, use the "Fibre" command followed by the "section" tag. This command requires a description of the geometry and materials for the patches that define the section fibres. To assign a relative tag material, use the patch *rect* command followed by the number of fibres in the local z and y direction from the local Cartesian coordinates defining the bottom left and top right vertex of the patch. The local reference system originates in the section's centre of gravity. Fiber elements are the most effective technique to model reinforced concrete beams (Figures 20-21).

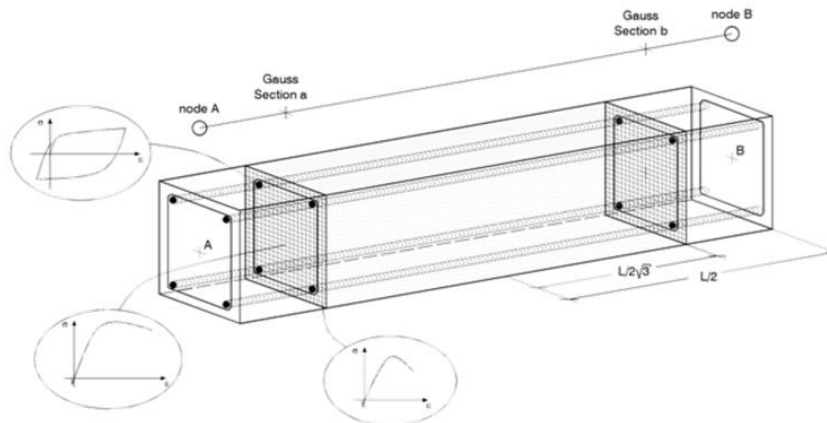


Figure 20. Diagram of the fibre modeling of a reinforced concrete beam

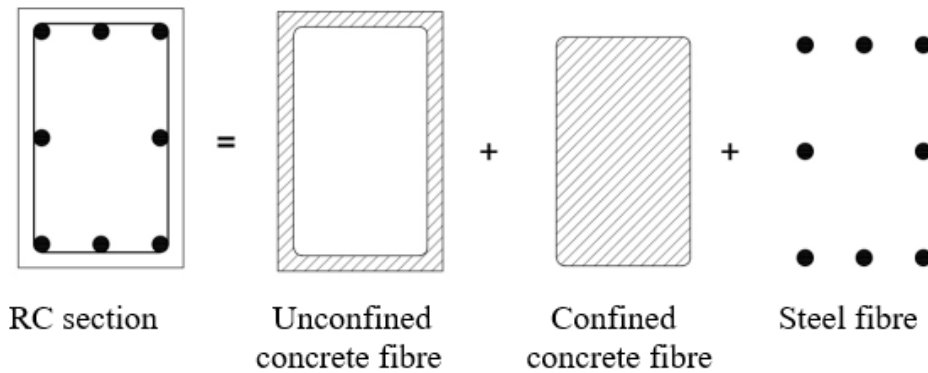


Figure 21. Fibre modeling of a conventional beam or pillar in a confinement frame

3.3.6 Elements

The element command is used to define the elements, which is followed by the element type selected. The model uses three types of elements: *forcebeamcolumn* for the beam and column, *elasticbeamcolumn* for the foundation beam, and *truss* element for the masonry struts. The software library contains two types of beam-column non-linear elements, both of which have diffuse plasticity: Force Based Elements (FBE) and Displacement Based Elements (DBE).

As explained in the literature review chapter, DBE elements are distinguished by linear curvature shape functions. This means that in order to accurately record the change in curvature that characterises a structural element such as a pillar or a beam. It is required to use an appropriate discretization of the element itself, that is, to refine the mesh by shortening the length of the individual elements while increasing their number. Whereas FBE elements overcome this issue, their definition necessitates the inclusion of a fixed number of control sections. Because of the mathematical framework that characterizes these elements, the system can perform a Gauss integration between these control sections and so capture curvature variation without undue discretization.

It is incorrect to claim that one element is superior to another; instead, DBE elements adapt better to particular conditions than FBE components. However, it is important to remember throughout the modeling phase that in order to appropriately capture curvature variation, the discretization, and hence the number of elements, must be increased if DBE elements are used. Using FBE elements can increase the number of integration points included within a single element.

In *OpenSeesPy*, the *ElasticBeamColumn* element is a specialised finite element used to simulate the behaviour of beams and columns in structural analysis; in this model, it represents the foundation beam. It combines the features of beam and column elements, allowing for the simulation of bending, axial, and shear deformations in the same element. This element is particularly helpful in replicating the behaviour of components that are subjected to axial and bending loads, as columns in frame systems. Hooke's Law governs the relationship between bending moments, axial force, and displacements when this element exhibits linear elastic behaviour by default. The material characteristics (elastic modulus, cross-sectional properties) and geometric characteristics (length, moment of inertia) of the element determine its stiffness. If given, the *ElasticBeamColumn* element can also take geometric and material nonlinearities into consideration. With the right material models, material nonlinearities like yielding and post-yield behaviour can be included. With the right analysis methods, geometric nonlinearities such significant displacements and rotations can be explained.

A *truss* element is a kind of structural element that can be used in *OpenSeesPy* to simulate axial forces in a construction. In this similar strut model, the masonry is treated as a *truss* element. One-dimensional *truss* elements are straight members that are solely subjected to axial loading. They have nodes at both ends, and the axial displacement along the element axis is the only degree of freedom taken into account. *OpenSeesPy* truss elements assume linear elastic behaviour by default, which means that Hooke's Law enforces a linear connection between axial force and axial displacement. In this element users can provide material parameters, such as elastic modulus and other applicable material nonlinearities, to precisely reflect the member material's behaviour.

3.4 Experimental Setup for Calibration Model

The calibration of the proposed multi-strut macro-model is based on the representative response of refined micro-models from Di Trapani and Di Benedetto research work. For this master thesis 10 experimental test were selected from the one already modelled by Di Trapani and Di Benedetto with micro-modelling technique. These specimens are here presented and modelled for the current research with multi-strut macro-model technique.

In next paragraphs the references of each experimental test are showed, reporting fundamentals details of the selected specimens.

3.4.1 Experimental Details of Specimen S1A and S1B

Experimental campaigns on single-storey, single-bay RC fully infilled frames subjected to lateral cyclic actions was conducted by Fabio Di Trapani (2014) on his research study of “Masonry infilled RC frames: Experimental results and development of predictive techniques for the assessment of seismic response”. Masonry infills selected for the execution of experimental tests was calcarenite blocks, clay blocks, and lightweight concrete blocks which represent three main traditional typologies used to realize infill panels. The experimental investigation included eight infilled frames known as the S1 series, which were supposed to simulate a common configuration found in existing buildings constructed for gravity loads and with no seismic detail. The geometric ratios between beam and column cross-sections define a weak column-strong beam arrangement shows in Figure 22 for specimen S1A and S1B. The ratio of bay length to storey height was around one. Specimens were placed with three distinct types of brickwork, the most common in practical applications: two specimens were filled with calcarenite masonry (S1A specimens), two with clay masonry (S1B specimens), and four with lightweight concrete masonry (S1C specimens). The average concrete strength after 28 days was 25 MPa, while the elastic Young modulus was approximately 23000 MPa. The reinforcement steel bars were of medium strength, measuring 450 MPa. Specimen Reference specimens S1A and S1B are used to validate calibration in this thesis study and its geometrical and typological details are tabulated in Table 1. To evaluate the mechanical characteristics of the masonry used to assemble the specimens, preliminary experimental testing was conducted. There were compressive tests conducted, including ordinary, lateral, and diagonal. In both orthogonal directions, compressive tests were conducted on mortars and units.

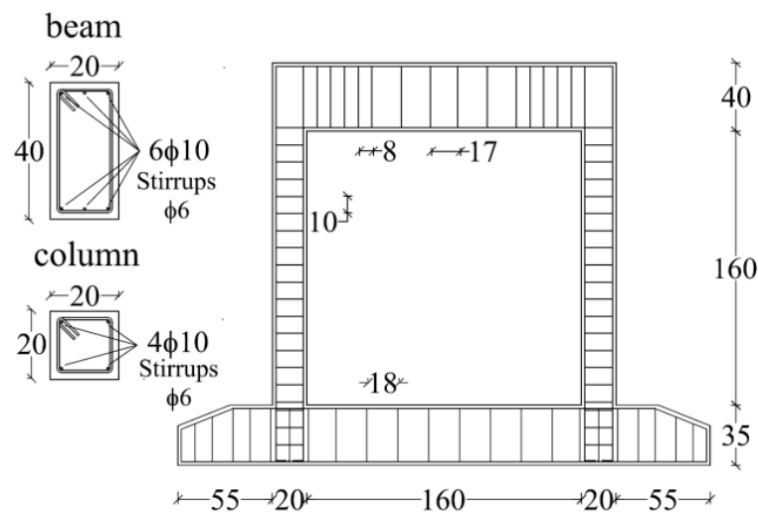


Figure 22. S1A and S1B specimen details (measures in cm) [16].

Specimens were subjected to an axial vertical constant load (200 kN on each column), which was applied by four manually operated hollow hydraulic jacks. Figure 23 illustrates the test setup. To maintain verticality and allow for free sliding of the head of each frame, the device for applying the vertical load was constrained in terms of horizontal displacement. The resulting force was determined by measuring the oil pressure in the jacks. Lateral loads were delivered using a horizontal double-acting jack monitored by a load cell with a 500 kN capacity that was interfaced with the acquisition system. The displacements at the top of each specimen were measured using a transducer with a measurement range of 0-200 mm. In addition to the lateral displacement of each frame head, four digital gauges with a measurement range of 0-12.5 mm were used to monitor the horizontal displacement and rotation (in the plane of each frame) of the base, thereby verifying the restricting efficacy.

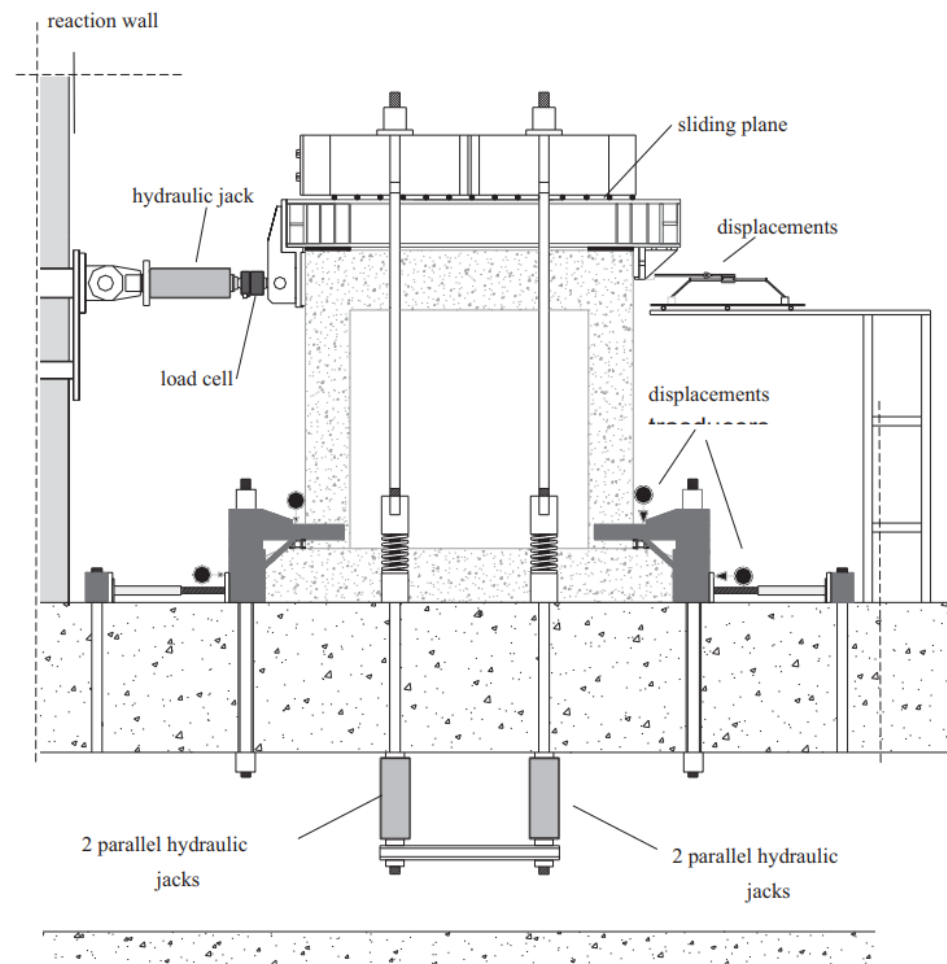


Figure 23. Test setup for specimen S1A and S1B[16] .

3.4.2 Experimental Details of Specimens 5,6 and 11

The performance of infilled frames under lateral loadings has been experimentally investigated by Mehrabi et al. (1996) on their research study "Performance of Masonry-Infilled R/C Frames Under In-plane Lateral Loads". The single-bay specimens 1–12 was chosen for the test, and they were modeled on half scale size, representing the internal bay of the bottom story frame. These frames were assessed in two different categories: weak frame and strong frame. The design of the weak frame is shown in Figure 24, which had weak columns and a strong beam, comparatively. In the strong frame, as seen in Figure 25, yielding was anticipated to start in the beam because the columns were heavier and had closer ties near the ends. The strong frame's beam design is the same as the weak frame's, with the exception that the former has additional shear reinforcement in the critical regions.

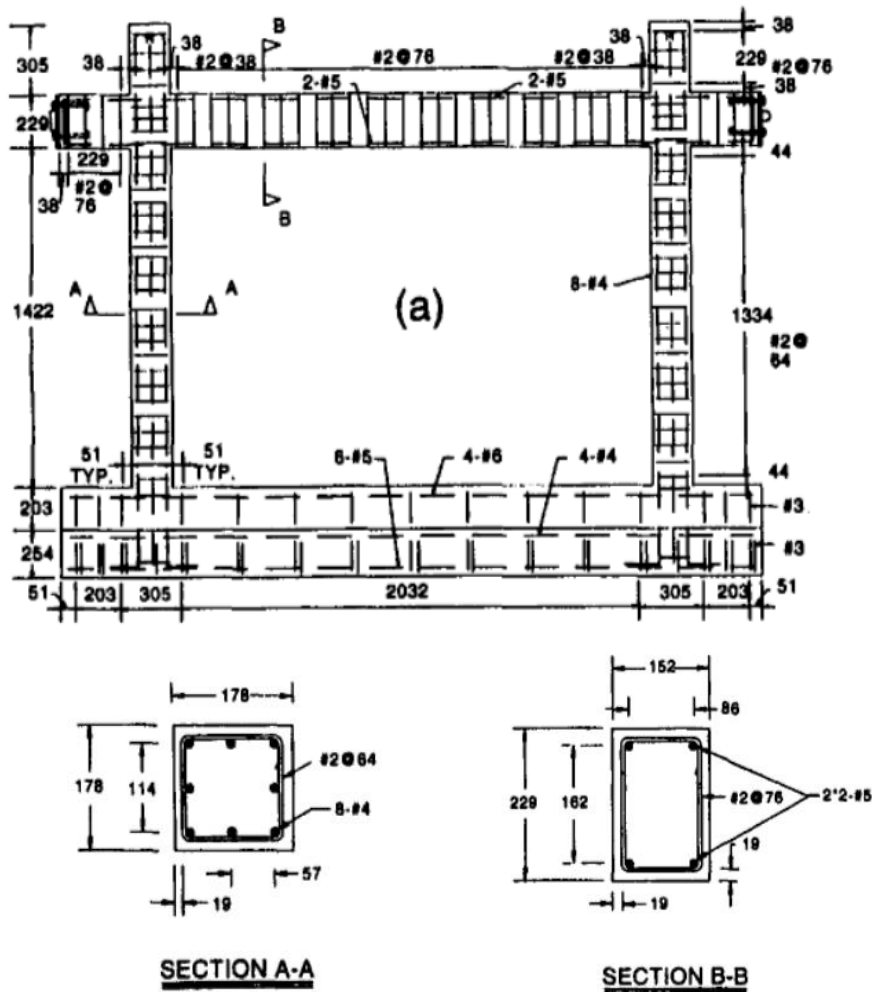


Figure 24. Design of weak frame test specimen 5, $h/l = 0.67$ (measure in mm) [29].

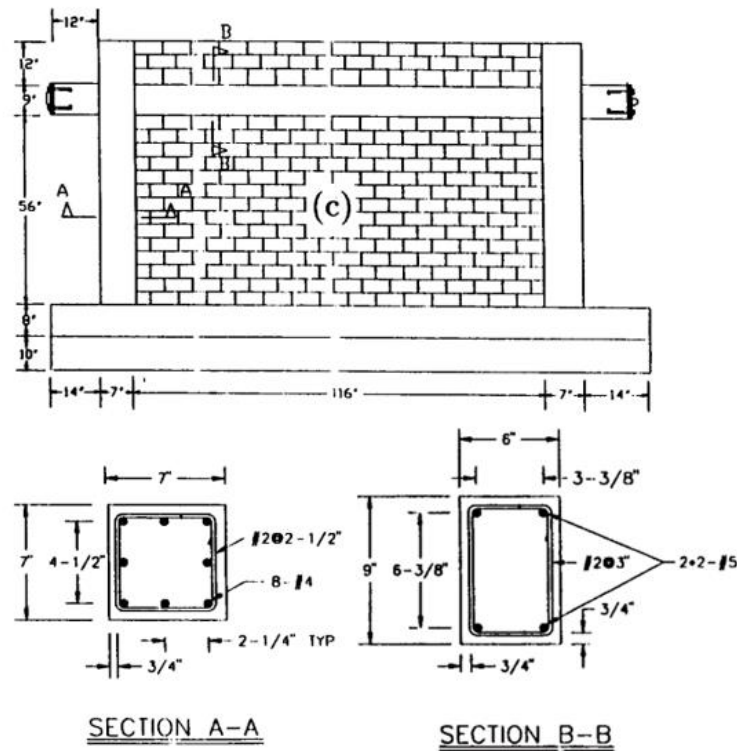


Figure 26. Design of weak frame test specimen 11, $h/l = 0.48$ (measure in inch, 1 in. = 25.4 mm) [15].

The lateral load was provided using two servocontrolled hydraulic actuators with a load capacity of 489 kN and stroke of ± 127 mm, as indicated in Figure 27. The vertical loads were applied by manually controlled hydraulic jacks, and their forces were immediately measured by strain gauges mounted to the vertical loading rods. Strain gauges and displacement transducers (LVDTs) were mounted in each test to monitor the strains in the reinforcing bars and the specimen's deformations at various points.

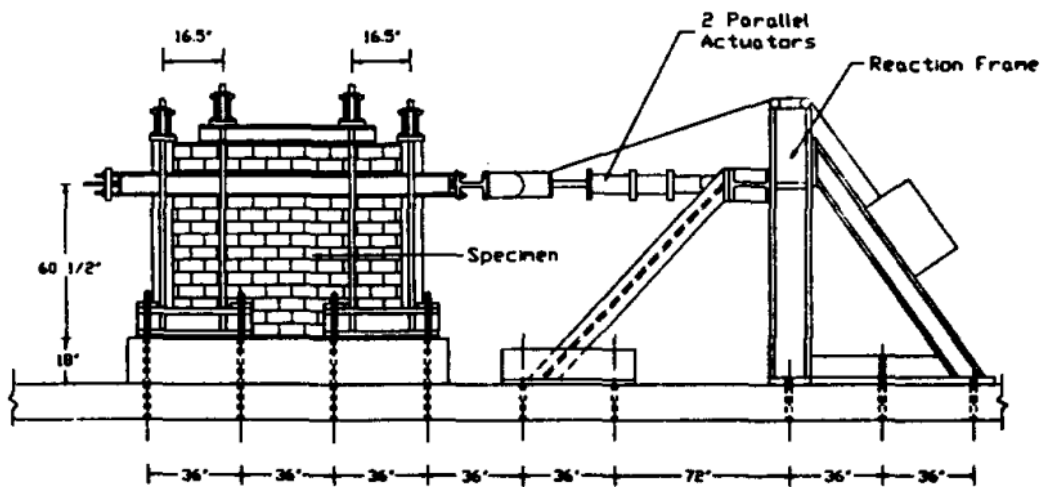


Figure 27. Test setup for specimen 5,6,11 (1 in = 25.4 mm)

3.4.3 Experimental Details of Specimen C1, L2 and N1

A single-degree-of-freedom (SDOF) pseudo-dynamic (PD) test system has been established for the experimental evaluation of the seismic behaviour of RC frames with unreinforced-masonry infills made of perforated brick and cement mortar. F. Colangelo (2004) conducted a series of experiments on half-size-scale single-bay single-story specimens in his research article "Pseudo-dynamic seismic response of reinforced concrete frames infilled with non-structural brick masonry". Out of thirteen infilled-frame specimens investigated, only three (C1, L2, N1) were chosen for calibration in this thesis study, and their structures are depicted in Figure 28. The specimens represent the first floor of a four-story building with a normal system frame. It is vital to note that a single horizontal seismic force is considered to act in the centre of the beam, where seismic displacement occurs. Gravity loads are defined as vertical forces applied to the beam-column joint. Each force originating from four stories is 400 kN. C and L frames are designed as medium-ductility structures using the ENV (pre-standard) version of seismic Eurocode, whereas N frames represent some older structures that follow Italy's prior seismic code. The N frames differ mostly from the C and L frames in terms of detail. The hoop is widely spaced and anchored by 90° overlapping hooks. There are no column crossties, and a straight lapped splice is inserted at the bottom. The N frames differ from each other in terms of steel grade since both deformed and round bar were used in Italy some decades ago. Geometric and typological details of reference specimens are tabulated in Table 1.

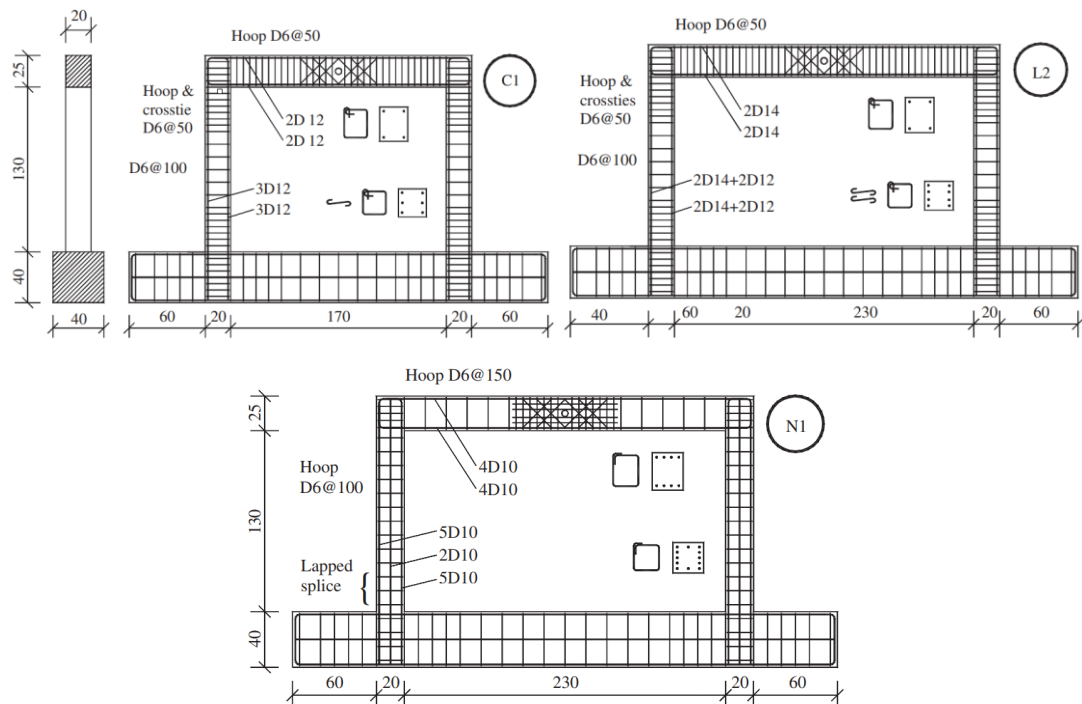


Figure 28. RC frame dimension for specimen C1, L2, N1 (measured in cm)

3.4.4 Experimental Details of Specimen TA2 and FIF

Morandi et al. (2018) tested TA2 and Trapani et al. (2023) tested FIF (Fully Infilled Frame). Every specimen is a fully filled RC frame with a distinctive geometry and set of mechanical masonry parameters. The following describes the experimental specimen in detail.

- **Specimen TA2**

Morandi et al. (2018) conducted an experimental campaign was carried out on six frame specimens in which a series of cyclic static in-plane and out-of-plane tests were performed on bare and fully or partially infilled full-scale single-storey, single-bay RC frames [Figure 29] developed in accordance with European (and Italian) code requirements. After tabulating the full geometry of the RC frame in Table 1 and characterising material components i.e., concrete, reinforcing steel is summarised in Table 2. Specimen TA2 was a fully infilled specimen, and the proportions of the RC frame specimen were chosen to realistically depict a component of a full-scale RC structure; a clear span of 4.22 m and a height of 2.95 m were used, respectively. Beam and column lengths have been extended beyond the beam-column panel zone to provide for adequate reinforcing rebar anchorage and force introduction during the test. The frame's foundation has an inverted T-shaped cross section. The RC frame specimen was designed with a single-story, single-bay frame on the ground floor of a simple four-story bare frame structural structure with a regular plan and elevation[26].

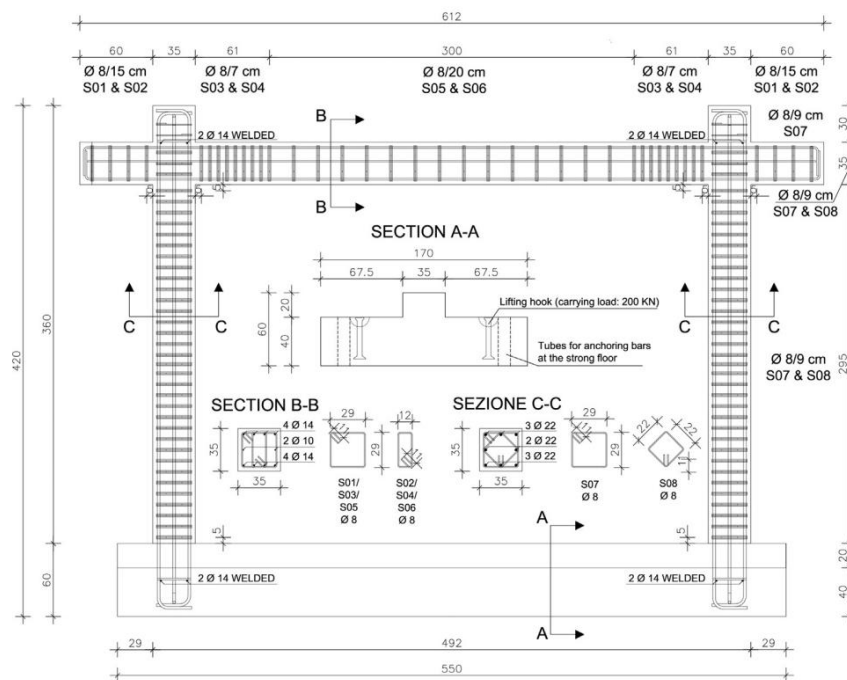


Figure 29. Reinforcement details of the RC frame for specimen TA2 (measured in cm) [30].

- **Specimen FIF**

The experimental program entailed by Trapani et al. (2023) subjected eight 2/3 scaled specimens to a quasi-static cyclic loading protocol. The specimens were designed in accordance with the Chinese standard GB 50011-201055 and represent a sub-frame taken from a typical three-story residential building in a moderate-to-low seismic hazard location. The eight examples consisted of a bare frame, one with a solid infill, and six infilled frames with openings. The geometric dimensions of the specimens shown in Table 1 correspond to the system presented in Figure 30 and characterising material components i.e., concrete, reinforcing steel is summarised in Table 2. The infills measured 2200 x 2100 mm and consisted of two wythes of hollow clay masonry bricks ($230 \times 110 \times 80$ mm). At the mid-height of the beam, a double-action hydraulic actuator that was attached to the steel beam on one side and the reaction wall on the other applied the horizontal lateral load. The steel beam was subjected to a system consisting of four prestressed rebars and two steel plates in order to transfer the horizontal force to the frame during reverse loading cycles. In addition, the RC columns received a concentrated vertical load applied by means of two separate hydraulic jacks. Two vertical hydraulic jacks were used to apply the constant vertical load of 390 kN. A horizontal steel beam that was in contact with the frame's columns via two steel plates carried the vertical weight from the jacks to the specimen. These plates made it possible to recreate the effects of gravity loads by distributing the vertical load to the columns at a rate of 195 kN per column [27].

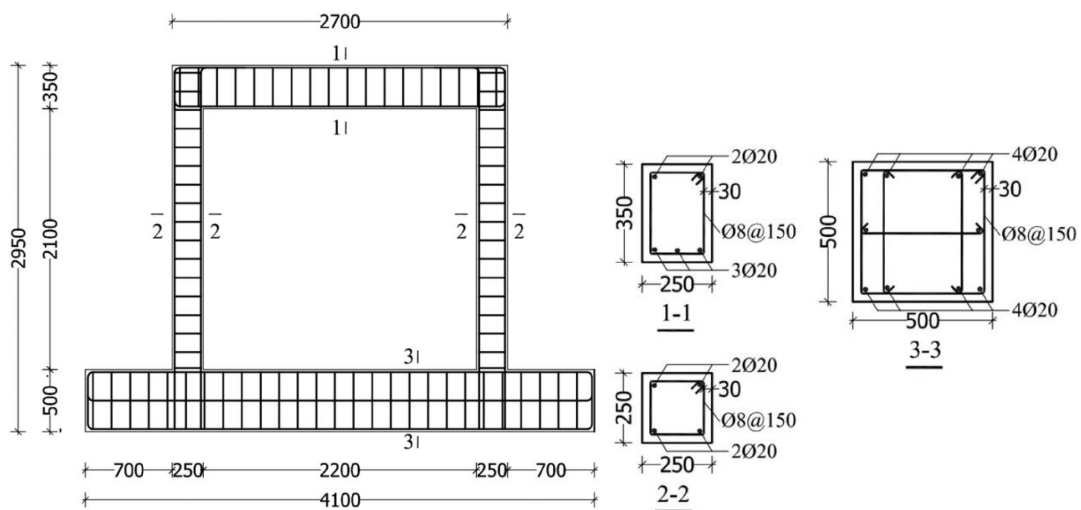


Figure 30. Reinforcement details of the RC frame for specimen FIF (measured in mm) [31].

Summarising, Table 1 provides the geometric and typological details of the reference specimens, whereas Table 2 lists the properties of the steel rebar reinforcement.

Table 1. Geometric and typological details of reference specimens

References	Spec. number	Masonry units type	h (mm)	h' (mm)	l (mm)	l' (mm)	l'/h'	b_c (mm)	h_c (mm)	b_b (mm)	h_b (mm)
Cavaleri and Di. Trapani (2014)	S1A	Calcarenite	1600	1975	1600	1800	0.91	200	200	200	400
Cavaleri and Di. Trapani (2014)	S1B	Clay / Hollow	1600	1975	1600	1800	0.91	200	200	200	400
Mehrabi et al. (1996)	5	Brick / Solid	1422	1638	2133	2311	1.41	178	178	152.4	228.6
Mehrabi et al. (1996)	6	Brick / Hollow	1422	1638	2133	2311	1.41	203.2	203.2	152.4	228.6
Mehrabi et al. (1996)	11	Brick / Solid	1422	1638	2946	3124	1.91	178	178	152.4	228.6
Colangelo (2005)	C1	Clay / Hollow	1300	1625	1700	1900	1.17	200	200	200	250
Colangelo (2005)	L2	Clay / Hollow	1300	1625	2300	2500	1.54	200	200	200	250
Colangelo (2005)	N1	Clay / Hollow	1300	1625	2300	2500	1.54	200	200	200	250
Morandi et al. (2018)	TA2	Clay / Hollow	2950	3125	4220	4570	1.46	350	350	350	350
Di Trapani et al. (2023)	FIF	Clay / Hollow	2100	2525	2200	2450	0.97	250	250	250	350

Where,

h = actual height of the masonry

h' = height from base to center of beam

l = actual length of masonry

b_c = width of column

h_c = depth of column

b_b = width of beam

h_b = depth of beam

Table 2. Concrete and steel rebar properties of reference specimen

References	Spec. number	Concrete Strength f_c (MPa)		Steel rebar			
Cavaleri and Di. Trapani (2014)	S1A	25.0		Bar size (mm)	6	10	12
Cavaleri and Di. Trapani (2014)	S1B	25.0	Deformed	Yield strength. (MPa)	450	450	450
Mehrabi et al. (1996)	5	20.9	no 2-plane	Bar size (mm)	no. 2 6.35	no. 4 12.7	no. 5 15.9
Mehrabi et al. (1996)	6	25.9	no 4- deformed.				
Mehrabi et al. (1996)	11	25.7	no 5 – deformed	Yield strength. (MPa)	367.6	420.7	413.8
Colangelo (2005)	C1	43.7	Deformed	Bar size (mm)	6	12	
Colangelo (2005)	L2	48.9	Deformed	Yield strength (MPa)	508	531	
Colangelo (2005)	N1	44.5	Round	Bar size (mm)	6	10	14
Colangelo (2005)				Yield strength (MPa)	377	346	
Morandi et al. (2018)	TA2	0.83 x 34 =28.22	Deformed	Bar size (mm)	10	14	22
Di Trapani et al. (2023)	FIF	0.83 x 13.53 = 11.23	Deformed	Yield strength. (MPa)	521.0	521.0	521.0
				Bar size (mm)	8	20	
				Yield strength. (MPa)	473.33	441.50	

3.5 Influence of Masonry Property in Calibration

The reinforced concrete frames are flexible structures that become extremely rigid when brick masonry walls are erected within them. However, buildings are still being analysed without simulating the masonry infill within the frames. Frames might be fully or partially infilled. It is commonly known that a bare frame has lower rigidity than a completely infilled frame. The stiffness of the frame and infill work together to increase the overall strength of the structure. Infills, on the one hand, are viewed as features that strengthen the lateral resistance of frame constructions; nevertheless, when put within the frame, they are thought to cause damage to the columns during lateral loading. So far, investigations have suggested that the damage is caused by the shear stress exerted by the walls within the frame at a particular distance from the beam column node, which can be referred to as the column's critical zone. If the critical zone and shear force exerted by the infilled walls are known, it will be easier to design column elements for shear force values at any point inside the column. The equivalent diagonal strut model is useful in the study of infilled frames due to its simplicity in determining strut width and its ability to be utilised in various analysis software as a single strut truss model linking the diagonal nodes. According to the different

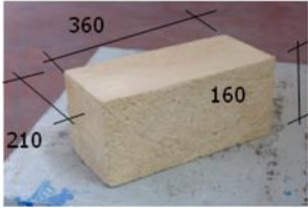


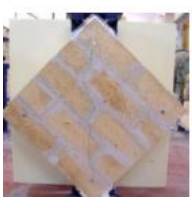
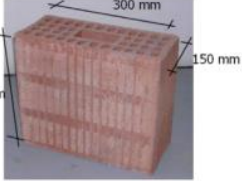



studies discussed in the literature review chapter, equivalent single strut models can provide a sufficient estimate of the stiffness of the infilled frame but cannot be used to achieve actual bending moments and shear forces in frames. At this point, the multi-strut model is useful.

To represent the intricate relationship between the masonry infill and the surrounding frame, two distinct modeling approaches can be found in the scientific literature: (i) local or micromodels and (ii) global or macro models. Micromodels are often FE models that provide a detailed description of the infill and frame interaction. Based on a physical understanding of the infill panel's behaviour, macro-models use equivalent trusses to simulate the infill's effect and replicate the overall stiffness, strength, and hysteretic response caused by the frame-to-infill interaction. The effect of the mortar joints is considered as a discrete feature in the model using the micro-modeling approach. It can be suggested that this method is the most accurate because mortar joints are the weakest plane in a masonry infill wall. Two-dimensional components for the masonry infill, interface elements for the infill-to-frame interaction, and beam elements for the frame (beams and columns) are all necessary due to the complex relationship between the infills and the surrounding frame. It is evident that, even with increased processing cost, the use of a complex two-dimensional mesh of finite elements offers a more accurate depiction of the geometry and local effects like crushing, cracking, and local interaction. To overcome the long computational time, the masonry infill walls can be analysed through simplified macro models that use different strategies such as equivalent single strut models to complex multi-strut models. Different scientific literature suggested the possibility of considering the effect of modeling the infills as equivalent to one diagonal strut that replaced the infill panel with an equivalent pin-jointed diagonal strut made of the same material and having the same thickness of the masonry infill wall and effective diagonal strut width based on experimental tests. To address the considerable computational time, brick infill walls can be evaluated using simplified micromodels that employ a variety of techniques, from similar single strut models to complicated multi-strut models. Based on experimental tests, different scientific literature suggested the possibility of considering the effect of modeling the infills as equivalent to one diagonal strut that replaced the infill panel with an equivalent pin-jointed diagonal strut made of the same material and having the same thicknesses the masonry infill wall and effective diagonal strut width. At the aim to perform a global analysis, the struts can be placed concentrically across the diagonals of the frame, as to local analysis, compression struts may be placed eccentrically.

3.5.1 Masonry Details for Specimen S1A and S1B

Masonry that was used in Fabio Di Trapani's (2014) research study, "Masonry infilled RC frames: Experimental results and development of predictive techniques for the assessment of seismic response" were arranged with three different kinds of: 2 specimens were infilled with calcarenite masonry (S1A specimens), 2 with clay masonry (S1B specimens), and 4 with lightweight concrete masonry (S1C specimens). In this thesis study for calibration only two specimens (S1A and S1B) are selected. During his research, experimental tests were conducted to evaluate mechanical properties. Ordinary, lateral, and diagonal compressive tests were performed. Compressive tests on mortars and units (both orthogonal directions) were also carried out. Table 3 summarises all relevant results in mechanical elastic characteristics and strengths.

Table 3. Mechanical properties of masonry for specimen S1A and S1B[16].

Calcarenite masonry				
S1A	Mortar - $f_m=3.06$ Units - $f_{bm}=7.06$	$E_2=3933$ $f_m=2.67$	$E_1=7408$ $f_m=3.08$	$G_{12}=1348$ $\nu_{12}=0.22; \nu_{21}=0.1$ $f_{vm}=0.73$
Clay masonry				
S1B	Mortar - $f_m=9.16$ Units - $f_{bm,v}=37.6$ $-f_{bm,h}=2.0$	$E_2=6401$ $f_m=8.81$	$E_1=5038$ $f_m=4.18$	$G_{12}=2547$ $\nu_{12}=0.07;$ $\nu_{21}=0.09$ $f_{vm}=1.07$

3.5.2 Masonry Details for Specimen 5,6 and 11

The mechanical property of masonry has been experimentally investigated by Mehrabi et al. (1996) on their research study "Performance of Masonry-Infilled R/C Frames Under In-plane Lateral Loads". For infill panels, 4 x 4 x 8-in. hollow and solid concrete masonry blocks were used in respective specimens. Their configurations are shown in Figure 31.

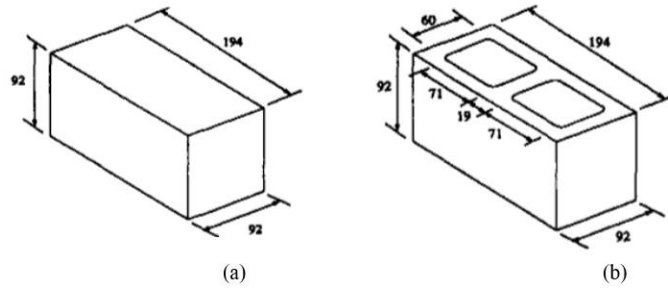


Figure 31. Geometric details of masonry units for specimen 5,6,11[29]

The compression test of 3-course masonry prisms was performed, and it can be noted that compressive strength of the 3-course masonry prisms is considerably lower than those of individual units and mortar. Average strength of masonry materials is tabulated in Table 4.

Table 4. Average strength of masonry materials for specimen 5,6,11[28]

Specimen number	Type of masonry units	Secant modulus (MPa)	Compressive strength (MPa)	Strain at peak stress	Compressive strength of masonry units (MPa)	Compressive strength of masonry (MPa)
5	Solid	8950	13.86	0.0023	15.57	17.57
6	Hollow	4200	10.14	0.0032	11.84	11.84
11	Solid	9610	11.45	0.0025	15.57	13.02

3.5.3 Masonry Details for Specimen C1, L2 and N1

F. Colangelo (2004) conducted an experiment on brick, mortar, and masonry in his research study "Pseudo-dynamic seismic response of reinforced concrete frames infilled with non-structural brick masonry". The average property of the infill brick, mortar and small-size wall are shown in Table 5. The greater thickness roughly compensates for the lesser properties, as measured by compression test performed in the vertical, horizontal, and diagonal direction of small -size walls.

Table 5. Average properties of the brick, mortar and masonry for specimen C1, L2 and N1[29]

Specimen		C1 and L2	N1
	Dimension (mm)	121 x 251 x 120	77 x 246 x 242
Brick	Vertical strength (MPa)	18.7	2.19
	Horizontal strength (MPa)	2.74	16.4
	Flexure strength (MPa)	4.35	3.49
Mortar	Compressive strength (MPa)	15.5	10.4
	Vertical strength (MPa)	5.1	2.74
	Horizontal strength (MPa)	3.39	3.9
Masonry	Shear strength (MPa)	0.87	0.58
	Vertical modulus (MPa)	4230	1212
	Horizontal modulus (MPa)	1688	2623
	Shear modulus (MPa)	1636	1409

3.5.4 Masonry Details for Specimen TA2, FIF

The masonry infill and the units are tested for the Specimen TA2 by Morandi et al. (2018) and Specimen FIF by Trapani et al. (2023). Experimental details of each specimen are described as follows.

- **Specimen TA2**

The selected infill typology is a traditional, strong single-leaf unreinforced masonry infill of 35 cm thickness. It consists of vertically hollowed lightweight tongue and groove clay block units with nominal dimensions of $235 \times 350 \times 235$ mm, a nominal volumetric percentage of holes of 50%, and a minimum thickness of webs and shells equal to 6.8 mm and 4.8 mm, respectively, as shown in Figure 32. The use of a general-purpose mortar type "M5" (compressive strength of 5 MPa) was deemed appropriate in light of usual construction practice. This masonry typology has a specific weight of 8.80 kN/m³. Table 6 shows the average properties of infill bricks, mortar, and small-size walls [26].

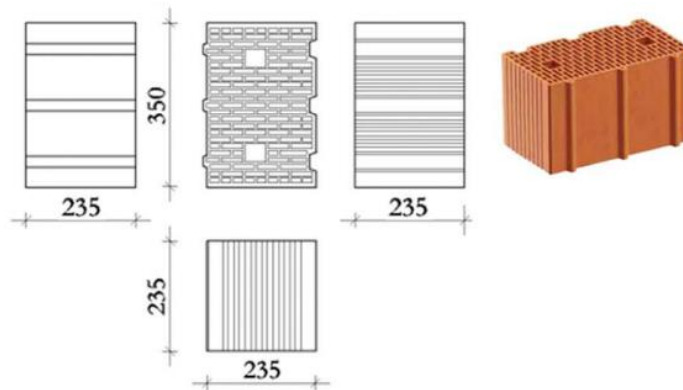


Figure 32. Detail of Masonry Unit for Specimen TA2 (measured in mm) [30]

- **Specimen FIF**

For the Specimen FIF (Full Infilled Frame), Trapani et al. (2023) conducted extensive material tests. Compressive tests on concrete cubes measuring 150 x 150 x 150 mm, tensile tests on steel rebars, compressive tests on bricks, and mortar cubes measuring 50 x 50 x 50 mm were among the material tests conducted. Bricks' opening percentage was 20%. Bricks were placed through compressive testing in a direction parallel to the holes. The test findings are presented in Table 6. The bricks' average compressive strength (f_b) was found to be 14.43 MPa. To provide an efficient transverse connection, the two masonries are formed of parallel brick layers stacked alternately throughout the layer's

length and thickness [Figure 33]. The accepted brick typology, as well as the masonry arrangement, is widely used in China and its South Asian neighbours, such as Pakistan, India, and Iran. The mortar layers were around 10 mm thick. The bricks were unscaled relative to the overall specimen's scale (2/3), but they were small enough that the scale effects were minimal. Three masonry prisms measuring $900 \times 750 \times 230$ mm were tested. The tests were carried out in the direction of the brick holes, which is orthogonal to the mortar bed joints. The average compressive strength of the masonry specimens (f_m) was found to be 3.36 MPa. The average elastic Young's modulus (E_m) measured 3730 MPa. Compressive tests on masonry prisms orthogonal to the hole direction were also performed. However, the results of these tests are excluded from this report due to differences caused by specimen anomalies. The horizontal resistance of masonry (f_{mh}) to be 75% of the vertical resistance. Diagonal shear tests were performed on masonry wall specimens measuring $620 \times 620 \times 230$ mm. The tests allowed for the evaluation of average shear resistance in the absence of compressive pressures by dividing the peak load by the diagonal transverse area of the specimen, which is the diagonal length divided by the thickness of the specimen. $f_{vm} = 0.356$ MPa is the result of the shear resistance.

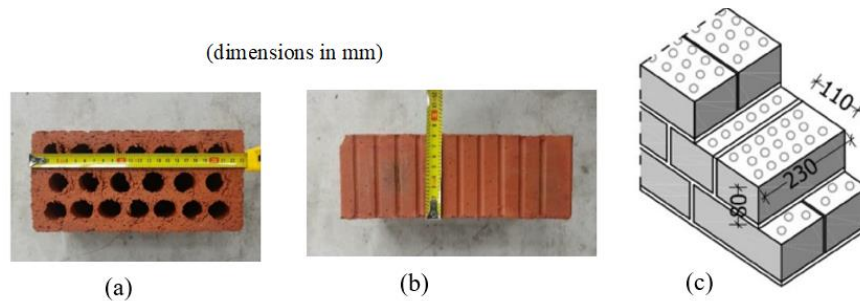


Figure 33. Brick units: (a) top view (b) side view and (c) arrangement of the masonry for specimen (FIF).

Table 6. Average properties of the brick, mortar and masonry for specimen TA2, FIF

Specimen		TA2	FIF
Brick	Dimension (mm)	235 x 350 x 235	110 x 230 x 80
	Vertical strength (MPa)	9.81	14.43
	Horizontal strength (MPa)	3.15	2.88
Mortar	Flexure strength (MPa)	2.15	
	Compressive strength (MPa)	7.68	3.25
	Vertical strength (MPa)	4.64	3.36
Masonry	Vertical modulus (MPa)	5299	3730
	Horizontal strength (MPa)	1.08	0.75×3.36 $= 2.52$
	Horizontal modulus (MPa)	494	0.75×3730 $= 2797.5$
Initial shear strength of bed-joints (MPa)		0.36	0.356

3.6 Equivalent Strut Macro-modeling for Calibration

As previously stated, the interaction between frame and infill is represented only by compression trusses. This research presents a simple macro-model first for evaluating the global response of the structure. The macro-model should be characterised by simple statements and use, short computational effort, and reliability of stiffness and of local effects on columns. In this case three struts are proposed, one of them is central strut connecting the diagonal nodes and other two struts are eccentric with diagonal strut. The modeling scheme for the infilled frame is illustrated in Figures 34. As the stress-strain law for the strut fibre section, a parabolic concrete model of the Kent-Scott-Park type (with linear tension softening) was used. The *Concrete02* model, implemented in OpenSeesPy, was used. This model is entirely defined by assigning peak strength (f_{md0}), peak strain (ϵ_{md0}), ultimate strength (f_{mdu}) and ultimate strain (ϵ_{mdu}) as shown in Figure 34(b).

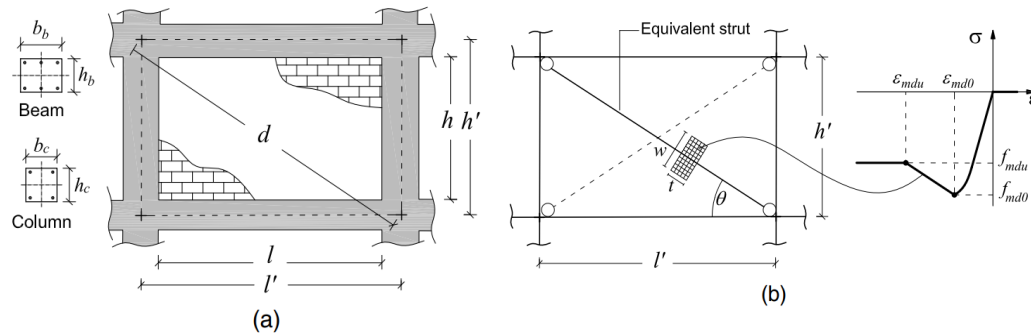


Figure 34. Modeling scheme for the infilled frame

The stress-strain characteristics differ from those of the masonry that makes up the infill wall under compression. This is an evident consequence of using diagonal struts to record a more complex mechanism involving the entire infilled frame subjected to lateral stress. For example, if the collapse modality for the infilled frame is sliding mortar joints or diagonal cracking, it is acceptable to expect a lower lateral resistance than that predicted by pure compression. Stress-strain characteristics of the strut have a strict dependence on masonry mechanical qualities, but their values depend on the geometrical and mechanical features of the entire infilled frame[3].

The identification of the equivalent strut cross-section geometry was performed by the following procedure. An example of calculation for specimen S1B is performed according to the sample calculation shown below. The stress-strain parameters of the equivalent struts are obtained using the empirical equations showed in the following sections. The thickness (t) of the strut is equal to the actual thickness of the infill and the width (W_s) calculated

according to following expressions is divided between the three struts to obtain the good result also with the approximation.

$$W_S = k\gamma^* \left(\frac{h}{l}\right) \frac{c^*}{\lambda^*\beta^*} d \quad (15)$$

where, referring to Figure 34, h and l = actual length and height of the masonry panel; d = length of the equivalent diagonal strut; and κ = coefficient used to account for the lateral stiffening effect exerted by vertical load. Expression for determining masonry stress-strain, including sample calculations for strut width of specimen S1B.

The frame is constituted by concrete having compressive strength $f_c = 25$ MPa and steel rebars with yielding stress $f_y = 450$ MPa. The hardening coefficient b is 0.001.

1. Calculation of elastic modulus (\tilde{E}_m) and compressive strength (\tilde{f}_m) of masonry

$$\tilde{E}_m = \sqrt{E_{m1}E_{m2}} = \sqrt{5070 \times 6040} = 5533.78 \text{ MPa} \quad (16)$$

$$\tilde{f}_m = \sqrt{f_{m1}f_{m2}} = \sqrt{4.18 \times 8.70} = 6.03 \text{ MPa} \quad (17)$$

E_{m1} and E_{m2} are the Young moduli of masonry along the horizontal and vertical direction, respectively. f_{m1} and f_{m2} compressive strength along orthogonal directions.

2. The parameter λ^* is evaluated by means of the formula proposed by Papia et al. (2003) as follows:

$$\lambda^* = \frac{\tilde{E}_m t h'}{E_c A_c} \left(\frac{h'^2}{l'^2} + \frac{1}{4} \frac{A_c}{A_b} \frac{l'}{h'} \right) \quad (18)$$

$$\lambda^* = \frac{5533.78}{25000} \frac{150 \times 1975}{200 \times 200} \left(\frac{1975^2}{1800^2} + \frac{1}{4} \frac{200 \times 200}{200 \times 400} \frac{1800}{1975} \right) = 2.16$$

A_b and A_c are the area of the cross-sections Elastic and columns, and the other symbols in Eq. (16) are deducible from Figure 34 and E_c is Elastic modulus of concrete.

3. Calculation of c^* and β^*

$$c^* = 0.249 - 0.00116 v + 0.567 v^2 \quad (19)$$

$$c^* = 0.249 - 0.00116 \times 0.15 + 0.567 \times 0.15^2 = 0.26$$

$$\beta^* = 0.146 - 0.0073 v + 0.126 v^2 \quad (20)$$

$$\beta^* = 0.146 - 0.0073 \times 0.15 + 0.126 \times 0.15^2 = 0.15$$

ν is Poisson's ratio of the masonry infill, evaluated along the diagonal direction of the masonry infill.

4. Calculation of total load (F_v) acting on the columns and vertical stiffness (σ_n) of columns and infill.

$$F_v = 2 \times 200 = 400 \text{ kN}$$

$$\sigma_n = \frac{F_v}{A_m} \left(\frac{E_m z A_m}{2E_c A_c + E_m z A_m} \right) \quad (21)$$

$$\sigma_n = \frac{400,000 \times 6040}{2 \times 25,000 \times 200 \times 200 + 6040 \times 150 \times 1600} = 0.7 \text{ MPa}$$

$A_m = t \times l$: transversal area of the infill panel.

5. Calculation of parameters k and γ^*

$$k = 1 + (18\lambda^* + 200)\varepsilon_v \quad (22)$$

$$k = 1 + (18 * 2.16 + 200) \frac{400,000}{2 \times 25,000 \times 200 \times 200} = 1.048$$

ε_v is axial strain evaluated on the two lateral columns.

$$\gamma^* = 1 + 0.5x \frac{r}{(l/h)^4} \quad (23)$$

$$\gamma^* = 1 + \frac{0.5}{(1600/1600)^4} = 1.5$$

$r = 1$ for the current case of solid infills.

6. Calculation of strut width W_s

$$W_s = k\gamma^* \left(\frac{h}{l} \right) \frac{c^*}{\lambda^* \beta^*} d$$

$$W_s = 1.048^{1.5} \times \left(\frac{1600}{1600} \right) \times \frac{0.26}{2.16^{0.15}} \times 2672.2 = 664.07 \text{ mm} \quad (24)$$

7. Calculation of f_{md0} , ε_{md0} , f_{mdu} and ε_{mdu}

Correlation parameters: α , β , γ , δ

$$\alpha = \frac{\bar{f}_m^2 \times W_s \times t}{(f_{vm} + \mu\sigma_n)^{0.2} \left(\frac{l}{h} \right) \times \lambda^{*0.2}} \quad (25)$$

$$= \frac{6.03^2 \times 664.07 \times 150}{(1.07 + 0.7 \times 0.7)^{0.2} \left(\frac{1600}{1600} \right) \times 2.16^{0.2}} = 2.84 \times 10^6$$

μ is Friction coefficient and f_{vm} is tensile strength of masonry.

$$f_{mdo} = \tilde{f}_m \times 26.9\alpha^{-0.287} = 6.03 \times 26.9 \times (2.84 \times 10^6)^2 = 2.28 \text{ Mpa} \quad (26)$$

$$\beta = \frac{f_{mdo}^{0.7} \times W_s \times t}{\tilde{E}_m^{0.2} \times d} = \frac{2.28^{0.7} \times 664.07 \times 150}{5533.78^{0.2} \times 2672.2} = 11.84 \quad (27)$$

$$f_{mdu} = f_{mdo}(0.043\beta - 0.06) = 2.28(0.043 \times 11.84 - 0.06) = 1.02 \quad (28)$$

$$\gamma = \left(\frac{f_{mdu}^2}{f_{mdo}}\right) \left(\frac{E_c}{\tilde{E}_m^{1.5}}\right) = \left(\frac{1.02^2}{2.28}\right) \left(\frac{25000}{5533.78^{1.5}}\right) = 0.027 \quad (29)$$

$$\varepsilon_{mdo} = 3.024 \times \varepsilon_{m0} \times \gamma^{0.347} = 3.024 \times 0.0015 \times 0.027^{0.347} = 0.0013 \quad (30)$$

$$\delta = \tilde{E}_m^{0.2} \times \varepsilon_{mdo} = 5533.78^{0.2} \times 0.0013 = 0.0074 \quad (31)$$

$$\varepsilon_{mdu} = 0.0184 \times \varepsilon_{mdo} \times \delta^{-1.166} \quad (32)$$

$$= 0.0184 \times 0.0013 \times 0.0074^{-1.166} = 0.0073$$

Similar calculations have been performed on various experimental test specimens. Table 6 shows the corresponding strut width and geometrical parameters of the S1A, 5, 6, 11, C1, L2, N1, TA2, and FIF specimens, as well as the mechanical and stress-strain parameters.

Table 7. Geometrical, mechanical, stress-strain parameters and equivalent strut width of infills.

References	Spec. number	F _v (kN)	t (mm)	E _{m1} (MPa)	E _{m2} (MPa)	E _c (MPa)	f _{md0} (MPa)	f _{mdu} (MPa)	ε _{md0}	ε _{mdu}	W _s (mm)
Cavaleri and Di. Trapani (2014)	S1A	400	200	7408	3933	25000	1.52	0.69	0.0012	0.0076	636.2
Cavaleri and Di. Trapani (2014)	S1B	400	150	5070	6040	25000	2.28	1.02	0.0013	0.0074	664.07
Mehrabi et al. (1996)	5	294	92	8949	8949	18064	4.47	1.28	0.0008	0.0071	552.37
Mehrabi et al. (1996)	6	294	92	2168	4198	19856	2.96	0.91	0.0014	0.0085	628.7
Mehrabi et al. (1996)	11	294	92	9604	9604	18133	4.09	1.18	0.0008	0.0071	741.46
Colangelo (2005)	C1	400	120	1688	4230	34200	2.04	0.74	0.0017	0.0084	604.75
Colangelo (2005)	L2	400	120	1688	4230	35417	2.17	0.68	0.0017	0.0084	614.05
Colangelo (2005)	N1	400	160	2623	1212	33354.1	1.75	0.73	0.0023	0.0088	625.47
Morandi et al. (2018)	TA2	800	350	494	5299	29000	0.93	0.6	0.0025	0.0089	1212.1
Di Trapani et al. (2023)	FIF	390	230	2798	3730	15750	1.34	0.67	0.0013	0.0084	827.95

CHAPTER 4

Analysis of Selected Specimens

4.1 Gravity Load Analysis

Gravity load simulation is essential for accurately representing real structures. Typical compressive stress values on concrete columns were determined, and the associated vertical loads were calculated. The vertical loads applied to the columns were $\frac{F_v}{2}$ per column, dimension of frame and applied load F_v of calibrated specimens are shown in Table 8. These stresses were selected to approximate normal gravity loads that are transferred from the upper stories to the bottom story.

Table 8. Gravity load and the dimension of frame for different specimens

Specimen reference	S1A	S1B	5	6	11	C1	L2	N1	TA2	FIF
Gravity load (F_v) kN	400	400	294	294	294	400	400	400	800	390
Length c/c l' mm	1800	1800	2311	2235	3124	1900	2500	2500	4570	2450
Height c/c h' mm	1975	1975	1638	1533	1638	1625	1625	1625	3125	2525

As seen in Figure 35, a series of hydraulic jacks was positioned atop the load cell to apply a vertical load. The electric power hydraulic pump was operated by hand to pressurize the jacks to a predetermined level of pressure. Throughout the testing, the jacks' pressure was maintained at the same level.

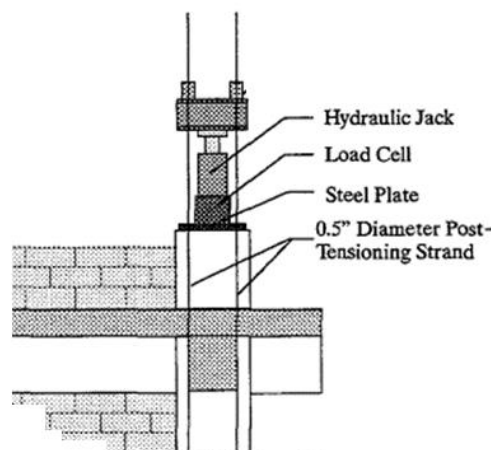


Figure 35. Elevation of vertical loading system

Using the generic infilled frame as a model, whose mechanical and geometric characteristics are shown in Figure 36(a). *OpenSeesPy* simulates the real specimen under the supposition that infill is replaced with the three equivalent multi-struts shown in Figure 36(b). When doing nonlinear analysis, this model is incredibly efficient and needs very little computational work. It has also the benefit that this model can capture the additional shear demand in the RC column due to infill.

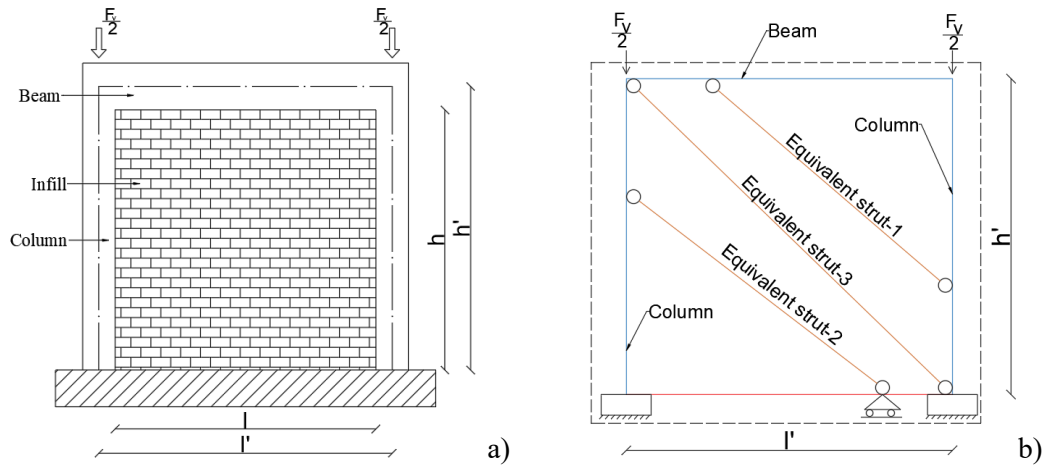


Figure 36. Gravity load (a) Mechanical and geometric features (b) *OpenSeesPy* model

Gravity loads are regarded as a component of the structural model since they are unaffected by the kind of lateral loading. Nodal forces $P = \frac{F_y}{2}$ can be applied to represent the vertical load distributed over the horizontal member because the beam is an elastic element. The two end nodes receive an equal share of the nodal forces. Below are the syntaxes for the gravity analysis used in *OpenSeesPy*, along with a description of its purpose.

- ***ops.system('BandGeneral')*** # Create the system of equation, a sparse solver with partial pivoting
The system Command creates the LinearSOE and LinearSolver objects, which are used to store and solve the analysis's system of equations. LinearSOEs include *BandGeneral SOE*, *BandSPD SOE*, *ProfileSPD SOE*, *SuperLU SOE*, *UmfPack SOE*, *FullGeneral*, *SparseSYM SOE*, *Mumps*, and *Cusp*. In this calibration study, the *BandGeneral* command is used to create a *BandGeneralSOE* linear system of equations object. As the name implies, this class applies to matrix systems with a banded profile. The matrix is stored in a one-dimensional array with a size equal to the bandwidth multiplied by the number of unknowns. When a solution is necessary, the Lapack routines *DGBSV* and *SGBTRS* are applied.

- ***ops.constraints('Transformation')*** # Create the constraint handler, the transformation method

The *constraints* Command is used to construct the *ConstraintHandler* object. Constraints enforce a relationship between degrees-of-freedom. The *ConstraintHandler* object determines how the constraint equations are enforced in the analysis. The different available constraint handler types in *OpenSeesPy* are *Plain Constraints*, *Transformation Method*, *Lagrange Multipliers*, *Penalty Method*. In this study *Transformation* constraints is used because this method performs single-point constraints directly. The matrix equation is not changed to enforce them; instead, the trial displacements are set directly at the nodes at the beginning of each analysis phase. If a node is fixed, constrain it using the *fix* command rather than *equalDOF*.

- ***ops.numberer('RCM')*** # Create the DOF numberer, the reverse Cuthill-McKee algorithm

The *numberer* command is used to create the *DOF_Numberer* object. The *DOF_Numberer* object defines the mapping between equation numbers and degrees of freedom. The *RCM* numberer assigns degrees of freedom to nodes using the *Reverse Cuthill-McKee* technique, making the analysis more efficient for big models. In addition to *RCM* numbers, *Plain* and *AMD* numbers can also be utilised, depending on the situation.

- ***ops.test('NormDispIncr', 1.0e-9, 1000, 0)*** # Create the convergence test, the norm of the residual with a tolerance of # 1e-9 and a max number of iterations of 1000

To create a Convergence Test object, use the *test* Command. A *ConvergenceTest* object is necessary for some *Solution Algorithm* objects in order to assess if convergence has been reached at the conclusion of an iteration phase. Relatively, the convergence test is used. Some other types of convergence test can be created additional arguments required depends on the *test Type*.

- ***ops.algorithm('Newton')*** # Create the solution algorithm, a Newton-Raphson algorithm

The *algorithm* Command is used to create a *Solution Algorithm* object, which specifies the steps required to solve the non-linear problem. This command creates a *Newton Raphson* algorithm object, which employs the *Newton-Raphson* algorithm to solve the nonlinear residual equations. The *Newton-Raphson* method is the most popular and reliable approach for solving nonlinear algebraic problems.

-
- ***ops.integrator('LoadControl', 1/n_steps)*** # Create the integration scheme, the LoadControl scheme using steps of 0.1 where $n_steps = 10$

The *integrator* Command is used to create the Integrator object. The *Integrator* object defines the meaning of the phrases in the System of Equations object. This object is used to calculate the predictive step for time $t+dt$, which specifies the tangent matrix and residual vector at each iteration to compute the corrective step based on the displacement increment dU . This Command specifies the kind of integrator based on whether the analysis is static or transient.

- ***ops.analysis('Static')*** # Create the analysis object

To create the Analysis object, use the *analysis* Command. The analyst's previously produced component objects are used to construct this analysis object. Incremental solution techniques are used in all currently available analysis items.

4.2 Pushover Analysis

Pushover analysis is an important technique in structural engineering for assessing seismic performance of buildings and other structures. While dynamic analysis methods model how a building reacts to ground motion over time, pushover analysis takes a different approach. Instead, it entails subjecting the structure to gradually increasing lateral loads that simulate the lateral pressures that would occur during a seismic event. Structure performs under varying amounts of lateral force by applying these loads incrementally, which aids in the identification of potential vulnerabilities and failure modes. This method provides significant information on the structure's total seismic performance, assisting in the design of a safer and more resilient building. Focusing on the single infilled frame subjected to lateral action [Figure. 37], it is clear that the masonry infills contribute to a considerable stiffening effect, which is typically associated with increased strength and decreased lateral displacement capacity. Even if the behaviour of a single infilled frame is simple to anticipate, the contribution made at the size of an entire building is influenced by a number of uncertainties that cannot be quantified without doing comprehensive analyses.

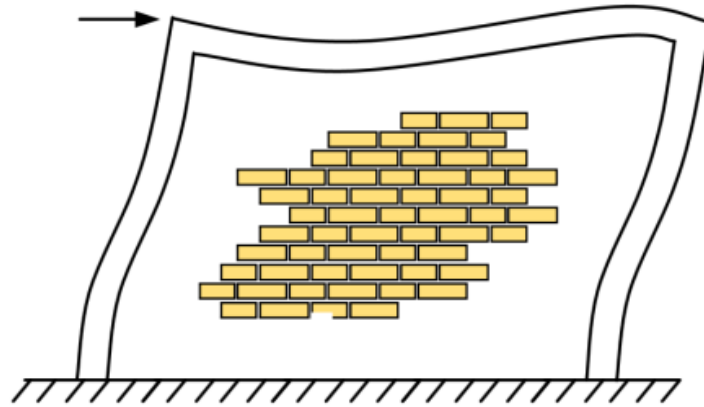


Figure 37. Infilled frame subjected to lateral actions.

Pushover analysis is carried out by gradually introducing lateral loads to a structure, often beginning at a low level, and gradually increasing the load until a preset limit is achieved. This loading pattern is intended to simulate the slow escalation of lateral forces encountered during a seismic event, in which the intensity of ground motion increases over time. The behaviour of masonry-infilled reinforced concrete frames subjected to in-plane lateral loads was investigated by a number of researchers. In late 1996 Mehrabi et al.[15] tested specimen of 1/2 -scale non-ductile reinforced concrete frames infilled with masonry under monotonically increasing as well as cyclic lateral loads to evaluate several elements of structural performance, including determining collapse causes, identifying weak places in the structure, and estimating capacity and demand ratios. Fabio Di Trapani (2014) on his research study the specimens were subjected to an axial vertical constant load and lateral loads were applied by a horizontal double-acting jack [Figure. 38] monitored by a load cell having 500kN as the nominal load interfaced with the acquisition system.

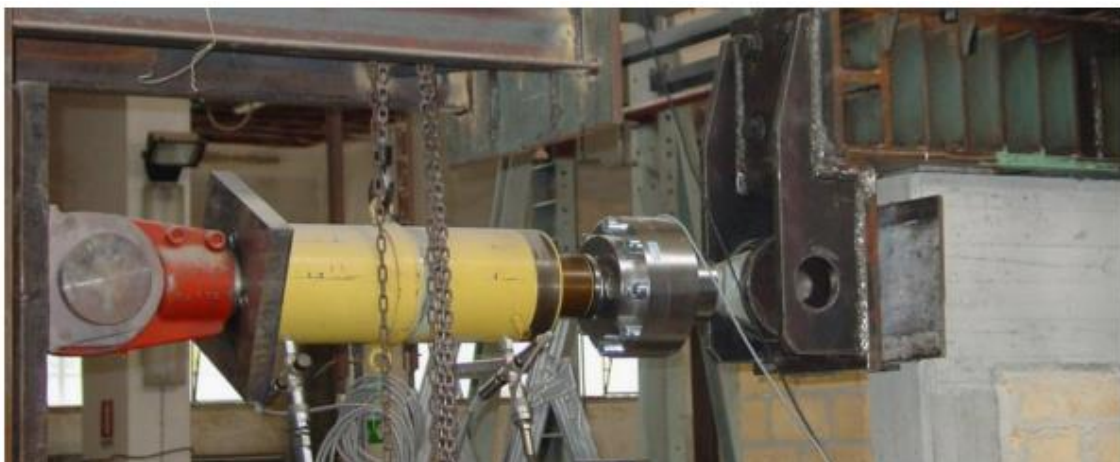


Figure 38. Hydraulic jack for lateral load application [16].

In *OpenSeesPy*, a pushover analysis implies scripting the progressive application of lateral loads to the structure and running a series of analyses to capture its reaction at each load stage. Using *OpenSeesPy* command to create the real structure Figure 39(a) into finite element model shown in Figure 39(b). This includes specifying nodes, elements, materials, sections, and boundary conditions. Specify uniform lateral load will be applied incrementally throughout the pushover analysis. In the annexe, the reinforced concrete portal frame that has undergone gravity load analysis is subjected to a pushover study in order to perform the nonlinear analysis using the *OpenSeesPy* software. In the analysis, a displacement control method is used, in which incremental displacement is imposed by a nodal dof, and the strategy iterates to determine the pseudo-time required to enforce that incremental displacement.

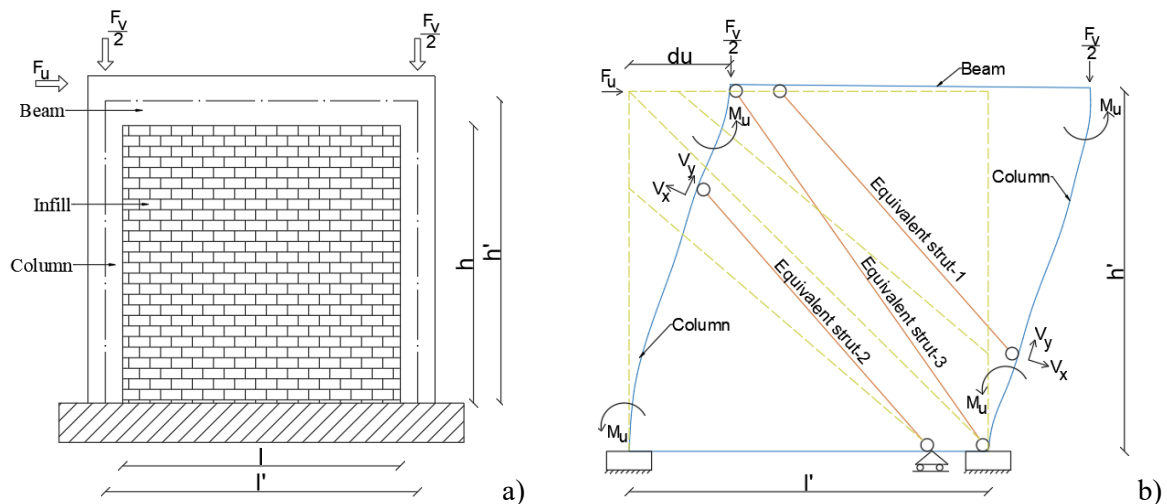


Figure 39. Lateral load applied incrementally throughout the pushover analysis.

(a) Real structure (b) *OpenSeesPy* FE model

In appendix the *OpenSeespy* command, at each new step in the analysis, the integrator will calculate the load increment required to increase the horizontal displacement at node 3 by 1 mm. A maximum displacement of 40 mm is sought. The analysis is done inside a while loop as the example is nonlinear and nonlinear models don't always converge. The model will either succeed in attaining its target displacement 'du' as a result of the loop, or it will not. A single analysis step is carried out at each phase. An alternative approach employing initial stiffness iterations will be tried if the analysis phase of the standard Newton solution technique fails. The models do not always converge for the preferred analysis options when dealing with nonlinear situations.

4.3 Evaluation of Numerical-Experimental Results Goodness

RMSD is an abbreviation for Root Mean Square Deviation, a statistical measure of the variations between values predicted by a model or theory and actual values. The difference between the predicted and actual values for each data point is known as the residual, and it may be computed by taking the square root of the mean of the residuals. This process also yields the RMSD for each data point. Because RMSD requires and uses real measurements at each projected data point, it is frequently employed in supervised learning applications. Mathematically, the RMSD is represented by the following formula:

$$RMSD = \sqrt{\frac{\sum_{i=0}^n (x_i - y_i)^2}{n}} \quad (33)$$

Where,

- n is the number of data point
- x_i is the i^{th} value in the first set (observed value)
- y_i is the i^{th} value in the second set (modeled value)

For this research work, the macro-macro-modelled data set is used to calibrate the experimental pushover data and the micro-model local shear data. As a result, the RMSD between the experimental pushover curve and the macro-model curve must be determined. The method for calculating the RMSD of different test specimens is explained.

The specimens from the S1A and S1B series were evaluated by increasing the displacement at each cycle to a drift of 2.5%. The cycle amplitude increment was variable throughout the loading pattern, reaching a maximum of 10 mm for the final cycles. Damage mechanisms were monitored during the testing to detect the propagation of cracks on infills and frames. Stiffness, strength, and ductility tests were conducted. So, a simplified force-displacement curve of monotonic strength envelopes of the experimental cyclic test is found [16]. The four experimental force-displacement curves in each specimen, S1A, and S1B, represent the envelopes of the cyclic experimental test. The RMSD value between these two curves is computed by averaging the four-experiment force-displacement curves [Figure 40] that were calibrated using the multi-strut model curve as a starting point. As shown in Figure 40, displacement is in the abscissa, and reaction force is in the ordinate, and the displacement values of each experimental curve differ based on the data recorded. Those curves are interpolated to find a common set of x-values. Then, it calculates corresponding y-values for each curve at those common x-values using linear interpolation as shown in the Annex. Linear interpolation is created in which the x-coordinate (displacement) and y-coordinate

(force) is taken then a sequence of x -common values is generated from the maximum of the minimum x -value of both curves to the minimum of the maximum x -value of both curves with a step size of 0.1. For each of the four curves, a new x -common value is generated, and the average reaction force is calculated and presented as the average experimental curve.

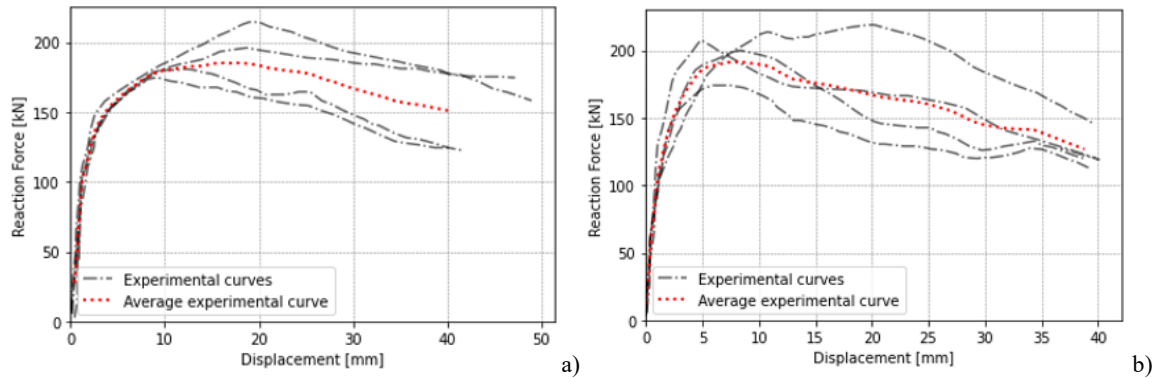


Figure 40. Experimental curves and average experimental curves for specimens (a) S1A (b) S1B

The average curve is also calculated for the remaining experimental tests using the previously mentioned method. Since specimens 5, 6 and 11 have two experimental curves, their average experimental curve is calculated using the same procedure as that of the S1A and S1B specimens, which is then used to calculate the RMSD. Since specimens C1, L2, and N1 have just one experimental curve, it is not necessary to determine the average curve. However, the RMSD value is determined by comparing the single force-displacement curve of each specimen with the multi-strut equivalent curve.

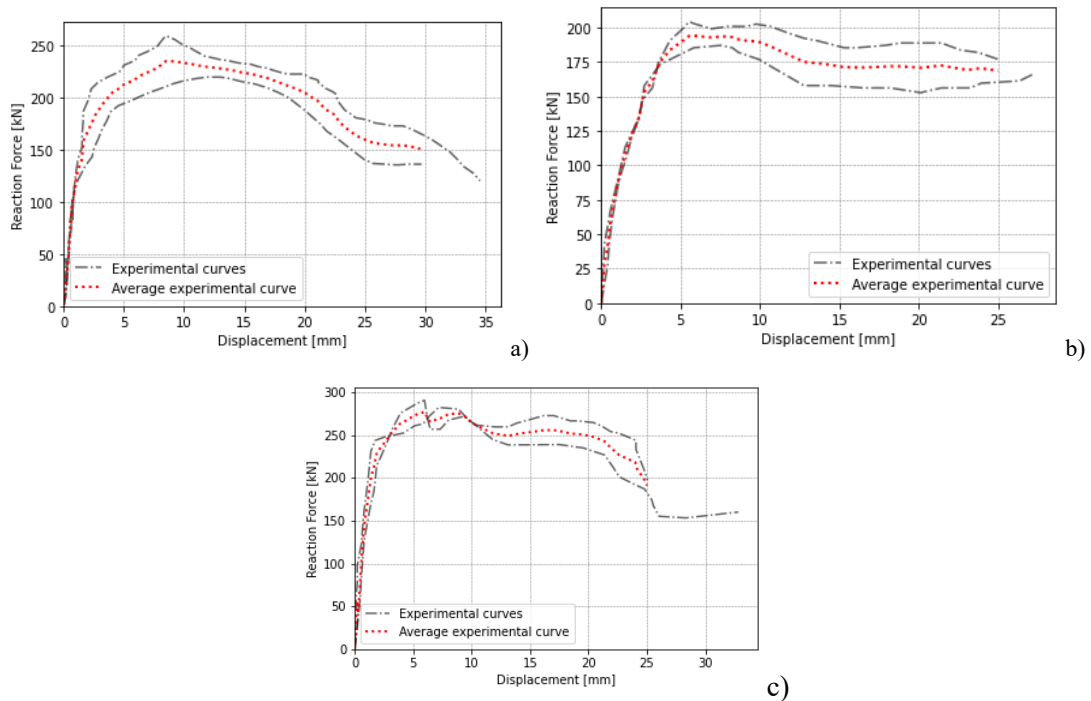


Figure 41. Experimental curves and average experimental curves for specimen (a) 5 (b) 6 (c) 11

The RMSD provides a measure of the average deviation between the predicted and observed values. A smaller RMSD indicates a better fit between the model and the data, while a greater RMSD suggests a poorer fit. The measured RMSD values of all the experimental tests is further described in Chapter 5.

4.4 Optimization with Genetic Algorithm (GA)

One of the most exciting problem-solving strategies, inspired by Charles Darwin's notion of natural evolution, is the algorithm family appropriately titled evolution computing. A genetic algorithm is the most well-known and commonly utilized branch of this family. In this calibration study genetic algorithms are used for the optimization of global and local response of the multi-strut macro model. Analogy to Darwinian evolution, and dive into their basic principles of operations as well as their underlying theory. Genetic algorithms implement a simplified version of the Darwinian evolution that takes place in nature and utilize their fundamental working principles and underlying theory of Darwinian evolution for optimization of the solution. Darwinian evolution theory worked in the principles of variation, inheritance, selection, crossover, and mutation. Evolution keeps a population of individual specimens that differ from one another. Those that are better adapted to their environment have a better chance of living, reproducing, and passing on their characteristics to future generations. As generations pass, organisms adapt to their surroundings and the problems they face. Crossover, in which kids inherit characteristics from both parents, is an important evolutionary facilitator. Crossover contributes to population diversity and the evolution of superior features throughout time. Furthermore, mutations, which are random variations in features, can play a part in evolution by introducing alterations that can result in a leap forward now and again.

Genetic algorithms attempt to identify the best solution to a given problem. Whereas Darwinian evolution maintains a population of individual specimens, genetic algorithms maintain a population of possible solutions, known as individuals, for any given problem. These candidate solutions are iteratively reviewed before being used to build a new generation of solutions. Those who are better at addressing this problem stand a better chance of getting chosen and passing on their skills to the next generation of candidate solutions. This way, as generations pass, possible solutions improve their ability to solve the problem. This technique is used in this thesis study to find the optimal position of the eccentric struts and calibrate the multi-strut micro model with the global response i.e. experimental force-displacement curve, and the peak shear demand at the column end due to infill panels.

In the following sections, various components of genetic algorithms are described how this theory of Darwinian evolution is used for the optimization process in this research study and also the related *PyGAD* code is in the Appendix.

- **Genotype:**

In nature, the genotype - a collection of genes organized into chromosomes - facilitates breeding, reproduction, and mutation. If two specimens breed, the offspring's chromosomes will include genes from both parents. In genetic algorithms, each individual is represented by a chromosome, which represents a collection of genes. A chromosome, for example, can be expressed as a node distance of eccentric struts, with each distance representing a single gene also known as an individual. For this research study 250 individuals are considered.

- **Initial Population**

The initial population is a sample of valid possible solutions (individuals) picked at random, in this research study initial population is taken as 10. Because genetic algorithms represent each individual with a chromosome, the beginning population consists of chromosomes. These chromosomes should comply to the chromosome format that we selected for the situation at hand, such as distance between the nodes. Instead of focusing on a single candidate, the genetic search is carried out over a population of candidate solutions. At any stage throughout the search, the algorithm saves a set of individuals from the current generation. A group of individuals selected at random who are genuine candidate solutions make up the starting population. The original population is essentially a collection of chromosomes since genetic algorithms utilize a chromosome to represent each individual. These chromosomes should match the format we selected for the chromosomes in concern.

- **Calculating the fitness function**

Each iteration of the algorithm evaluates the individuals using a fitness function, commonly known as the target function. This is the function we want to optimize or the problem we want to address. Individuals with a higher fitness score offer superior solutions and are more likely to be selected to reproduce and represent the future generation. The fitness function is determined for each individual. This is done once for

the initial population and then again for each subsequent generation using the genetic operators' selection, crossover, and mutation. This calculation can be done concurrently because each individual's fitness is independent of the others. Because the selection stage that follows the fitness calculation typically estimates people with higher fitness scores to be superior solutions, genetic algorithms are inherently biased toward identifying the maximum values of the fitness function. The quality of the solutions improves with time, as do the fitness values, and the process can be stopped once a solution with a good fitness value has been discovered.

$$\text{Fitness function} = \frac{1}{((RMSD_{global} + \alpha(\Delta_{WW} + \Delta_{LL}))/1000)} \quad (34)$$

Whereas,

$$\alpha = 6$$

$$\Delta_{WW} = |\text{shear}_{\text{max_micromodel}} - \text{shear}_{\text{max_propoesdmodel}}| \text{ for windward column}$$

$$\Delta_{LL} = |\text{shear}_{\text{max_micromodel}} - \text{shear}_{\text{max_propoesdmodel}}| \text{ for leeward column}$$

- **Selection, crossover, and mutation**

The **selection** operator is in charge of selecting individuals from the current population in such a way that better individuals have an advantage. After determining the fitness of each member in the population, a selection procedure is employed to determine which individuals will be allowed to reproduce and generate offspring that will constitute the next generation. This selection method is based on the individuals' fitness scores. Those with better scores are more likely to be selected and pass on their genetic material to the next generation. Individuals with poor fitness levels can still be selected, albeit with a lesser chance. This manner, their genetic material is not fully removed.

The **crossover** (or recombination) operator generates offspring from the selected individuals. This is typically accomplished by selecting two individuals at a time and interchanging sections of their chromosomes to produce two new chromosomes representing the offspring. The Crossover techniques section provides examples of selection operators. To generate a pair of new humans, two parents are typically chosen from the current generation, and sections of their chromosomes are swapped to form two new chromosomes representing the children. Crossover is also known as recombination. The **mutation** operator has the ability to randomly change one or more of the chromosome values of each newly produced individual. The mutation happens with an extremely low chance. The Mutation Methods section contains examples of mutation

operators. The mutation operator's objective is to refresh the population, introduce new patterns into the chromosomes, and promote exploration in unexplored portions of the solution space periodically and randomly. A mutation can show up as a random alteration in a gene. Mutations are implemented as random adjustments to one or more chromosomal variables.

- **Stopping conditions**

When assessing if the process can stop, there may be several conditions to consider. The maximum number of generations has been achieved. This also helps to minimize the algorithm's runtime and processing resources. Accepts a function that can be called only once, either before the genetic algorithm finishes or after all generations are completed. This function must accept two parameters: the first represents the genetic algorithm instance, and the second is a list of fitness values for the last population's solutions. The lower range of stopping condition is the size of the column and higher range is half of maximum of beam length or column height.

In summary, a population of randomly produced candidate solutions, or people, constitute the starting point of the genetic algorithm flow and are assessed in relation to the fitness function. Table 9 shows the Parameters that used in genetic algorithm for optimisation of the global and local response. The core of the flow is a loop in which the individuals are reevaluated after the genetic operators of crossover, mutation, and selection are applied in turn. The best member of the current population is chosen as the solution when the loop stops, which happens when a stopping condition is met. Genetic algorithms' primary benefits are their ability to handle difficult mathematical problems with global optimization and their inability to handle issues with no mathematical representation.

Table 9. Parameters that used in genetic algorithm for optimisation of the global and local response.

Attributes	Parameters
Number of generations	10
Number of individuals	250
Numbers of parents mating	3
Number of genes	4
Fitness function	As eqn. 34
Genes to mutate	1
Keep elitism	2
Lower stopping criteria	Width of column
Upper stopping criteria	$\max 0.5 (\text{Beam}_{\text{length}} \text{ or } \text{Column}_{\text{height}})$

CHAPTER 5

Calibration Result

5.1 Integrating Masonry Infill with the Macro-Model

The equivalent multi-strut macro-model can be used to simulate the global and local responses of the infilled frame. The model makes use of fibre beam elements with distributed plasticity, therefore determining the mechanical properties of similar struts begins with the calibrating global and local response. The calibration process begins by creating a simplified force-displacement rule for a single-bay, single-story infilled frame. The equivalent multi-strut is identified by calibrating the material's constitutive law and the position of non-diagonal struts so that the infilled frame fits best in plane global response and has maximum shear force (local response) in windward and leeward columns with the simplified curve.

This research studies a simple macro-model able to provide an appropriate evaluation of stresses in columns even in a global structural model. The macro-model is calibrated using the findings obtained with the FE model, validated by comparisons with experimental data and used to calculate the lateral stiffness of infilled frames. The proposed solution is based on three struts: one diagonal and two non-diagonal approaches. In this scenario, the two non-diagonal strut placements [Figure 42] are identified by matching the peak shear force on columns and calibrating the shear-displacement curves produced from the micromodel technique. The total width of the strut (W_s) is calculated using the single-strut model presented in previous Chapter 3.6, and the strut width (W_s) for all referenced specimens is already listed in Table 7.

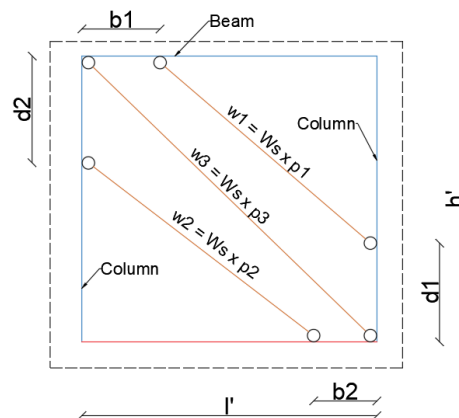


Figure 42. Schematization of the infill by three equivalent struts and definition of the position.

The aim is to present a simple macro-model in which the width (W_s) estimated according to Eq. (24) is divided among three struts with different weightage (p_1, p_2, p_3) according to the length-to-height ratio (l'/h') of the RC frame with different trial and error until good results obtained with this approximation as shown in Table 9. To apply the three-strut model, appropriate relationships specifying the position of the extremities of the two non-diagonal equivalent struts' behaviour have been stated that based on the most significant parameters influencing the infill-frame behaviour. After determining the weightage of each strut p_1, p_2 , and p_3 with different trial and the positions of the eccentric struts shown in Figure 42 by using GA, the reaction force and peak shear force on column values were calibrated to find the optimise solution. Weightage of each strut and the position of non-diagonal struts after calibration are shown in Table 10.

Table 10. Width of each strut and position of eccentric struts by GA

References	Spec. number	l'/h' (mm)	$w_1=p_1 \times W_s$ (mm)	$w_2=p_2 \times W_s$ (mm)	$w_3=p_3 \times W_s$ (mm)	d_1 (mm)	d_2 (mm)	b_1 (mm)	b_2 (mm)
Cavaleri and Di. Trapani (2014)	S1A	0.91	$0.45 \times 636.2 = 286.3$	$0.35 \times 636.2 = 222.67$	$0.25 \times 636.2 = 159.05$	330	482	205	396
Cavaleri and Di. Trapani (2014)	S1B	0.91	$0.45 \times 664.07 = 298.83$	$0.35 \times 664.07 = 232.42$	$0.25 \times 664.07 = 166.01$	498	332	390	208
Mehrabi et al. (1996)	5	1.41	$0.5 \times 552.37 = 276.18$	$0.35 \times 552.37 = 198.32$	$0.20 \times 552.37 = 110.47$	291	351	280	187
Mehrabi et al. (1996)	6	1.41	$0.5 \times 628.7 = 314.35$	$0.35 \times 628.7 = 220.04$	$0.20 \times 628.7 = 125.74$	281	325	193	145
Mehrabi et al. (1996)	11	1.91	$0.50 \times 741.46 = 370.73$	$0.45 \times 741.46 = 333.65$	$0.15 \times 741.46 = 111.22$	580	350	550	240
Colangelo (2005)	C1	1.17	$0.50 \times 604.75 = 302.37$	$0.35 \times 604.75 = 211.66$	$0.20 \times 604.75 = 120.95$	290	210	209	153
Colangelo (2005)	L2	1.54	$0.50 \times 614.05 = 307.02$	$0.40 \times 614.05 = 245.62$	$0.15 \times 614.05 = 92.10$	413	290	280	172
Colangelo (2005)	N1	1.54	$0.50 \times 625.47 = 312.78$	$0.40 \times 625.47 = 250.18$	$0.15 \times 625.47 = 93.82$	405	235	250	173
Morandi et al. (2018)	TA2	1.46	$0.50 \times 1212.1 = 606.05$	$0.35 \times 1212.1 = 424.23$	$0.20 \times 1212.1 = 242.42$	465	229	356	152
Di Trapani et al. (2023)	FIF	0.97	$0.45 \times 827.95 = 372.52$	$0.35 \times 827.95 = 289.78$	$0.25 \times 827.95 = 206.98235$	235	261	171	140

5.2 Calibration with Experimental Data (Global Response) using GA

Calibration with experimental data is an important phase in research studies that involves comparing experimental results to numerical models to assure the accuracy, reliability, and consistency of findings. This technique assists researchers in confirming the validity of their

methodologies, assessing the precision of measurements, and detecting any numerical inaccuracies. Experimental pushover curves are obtained by physically testing structures under gradually increasing lateral loads or cyclic loads until they fail. These curves provide significant information about the structure's behaviour and ability to withstand seismic forces. In contrast, macro-model multi-strut pushover curves are created using computational models that predict the structural reaction to lateral load. These models reduce the structure's complicated behaviour to a set of parameters and equations, allowing for more efficient study and prediction of structural performance.

To calibrate the proposed multi-strut macro model and experimental force-displacement data, blind prediction of several test specimens was carried out. This database contains 10 infilled frame specimens with various characteristics and aspect ratio. The specimens are those by Cavaleri and Di Trapani (2014), Mehrabi et al. (1996), Colangelo (2005), Morandi et al. (2018), Trapani et al. (2023), Morandi et al. (2018). All these specimens are single-bay and single-story, and they are laterally loaded by cyclic or monotonic load as described in previous chapter. Using the modeling approach described earlier, the model for each specimen was created and analysed. The specimens subjected to monotonic loading are compared in Figures 43–45 between the experimental backbone curves and the multi-strut macro model load-displacement. In particular, the stiffness and peak strength of all specimens show good agreement between the GA model data and the experiment. The comparison of the *OpenSeesPy* model curves found out by GA with the experimental backbone curve for several referenced specimens is presented in the subsequent section.

- **Calibration with Cavaleri and Di Trapani specimens S1A and S1B**

The multi-strut macro model used to model the reinforced concrete framed specimens S1A and S1B, which were filled with clay hollow brick and calcarenite, respectively, is subjected to cyclic loading. The force-displacement curve derived from the model is compared to the positive and negative experimental monotonic envelopes depicted in Figure 43. S1A and S1B, the discrepancy between the *OpenSeesPy* multi-strut model curve by using GA and the average experimental curve shown in the same figure. Table 11 below shows the goodness function RMSD value of this deviation.

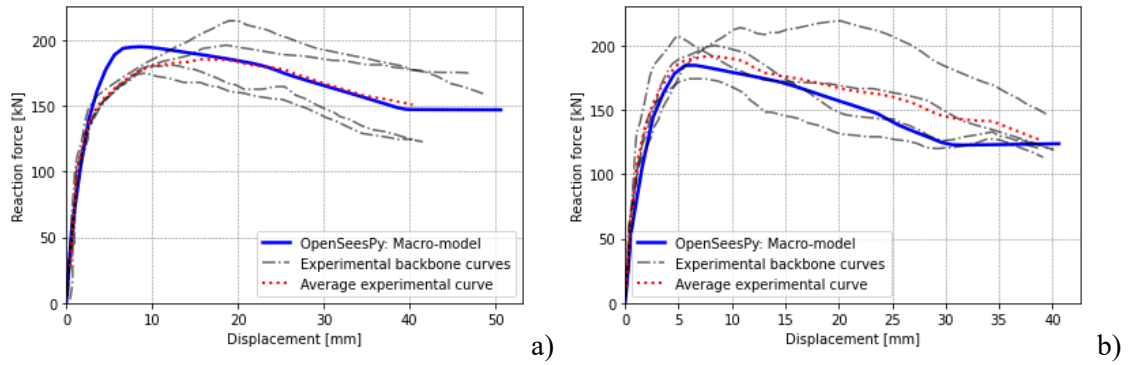


Figure 43. Experimental backbone curve and pushover curve by GA for specimens (a) S1A (b) S1B

- **Calibration with Mehrabi et al. specimens 5, 6 and 11**

Mehrabi and Shing experimented with specimens subjected to cyclic loads with a constant vertical force. For the calibration investigation, both solid and hollow concrete masonry panels with strong and weak infills were evaluated. In their investigation, they conclude that specimens with strong frames and strong panels performed better than those with weak frames and weak panels in terms of load resistance and energy dissipation. The variation between the *OpenSeesPy* multi-strut model pushover curve by GA and the average experimental curve is shown in Figure 44-45 for the referenced specimen. The goodness function RMSD value of this deviation is displayed in Table 11 below.

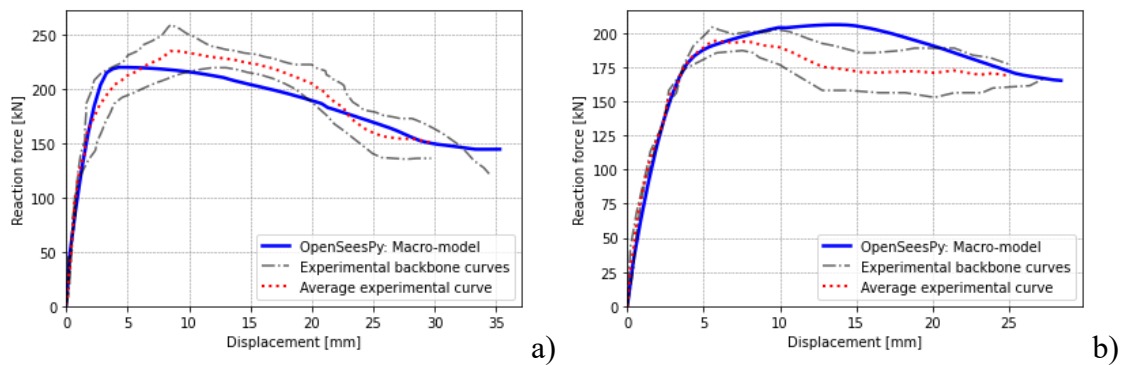


Figure 44. Experimental backbone curve and pushover curve by GA for specimens (a) 5 (b) 6

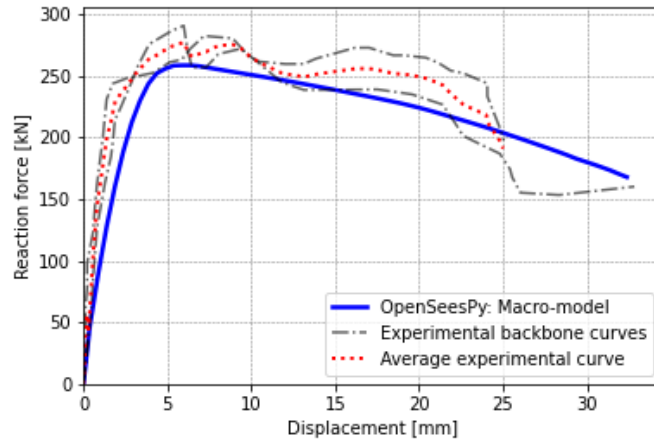


Figure 45. Experimental backbone curve and pushover curve by GA for specimen 11

- **Calibration with Colangelo specimens C1, L2 and N1**

Colangelo experimented with specimens subjected to cyclic loads with a constant vertical force filled with clay hollow bricks. Infills consisting of cement mortar and perforated bricks being relatively great, results confirm that infills substantially affect the basic global properties. On his experimental investigation he compared to the bare specimen and conclude the initial stiffness increases by approximately one order of magnitude and the peak strength, on average, more than doubles. In this calibration research study, the infill is modeled as multi-strut in *OpenSeesPy* and the variation of the numerical pushover curve by GA with an average experimental curve is shown in Figure 46. Table 11 below shows the goodness function RMSD value of this deviation.

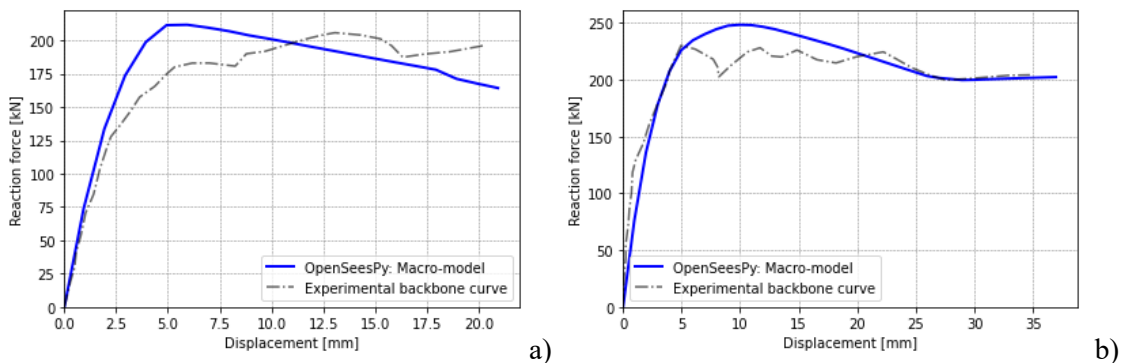


Figure 46. Experimental backbone curve and pushover curve by GA for specimens (a) C1 (b) L2

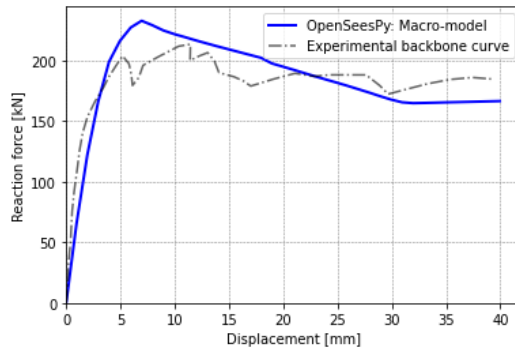


Figure 47. Experimental backbone curve and pushover curve by GA for specimen N1

- **Validation with specimens TA2 and FIF**

Morandi et al. (2018) and Trapani et al. (2023) each test the referenced infilled frame specimens TA2 and FIF respectively. The cyclic in-plane tests on infilled frame TA2 specimens were assessed in terms of applied force as a function of top displacement measured at half-height of the top beam, which corresponds to the horizontal actuator's centreline. Force-displacement curves and their related envelopes per cycle were obtained. Similarly, the study focused on completely infilled frame cases (FIF), with results analysed and compared in terms of strength, stiffness, energy dissipation capacity, and damage evolution. His extensive study of the results revealed that all infilled frame specimens demonstrated a significant change in response when compared to bared frame specimens, showing that the infills played a critical role. Both cases of infilled frames with and without apertures showed an overall improvement in stiffness and resistance. Figure 48 depicts the backbone curves (positive and negative) for the various specimens where strength and stiffness are more easily observed. In this calibration research study, the infill is represented as a multi-strut in *OpenSeesPy* by GA, and Figure 48 shows the change of the numerical pushover curve by GA with an average experimental curve. Table 11 displays the goodness function RMSD value for this deviation.

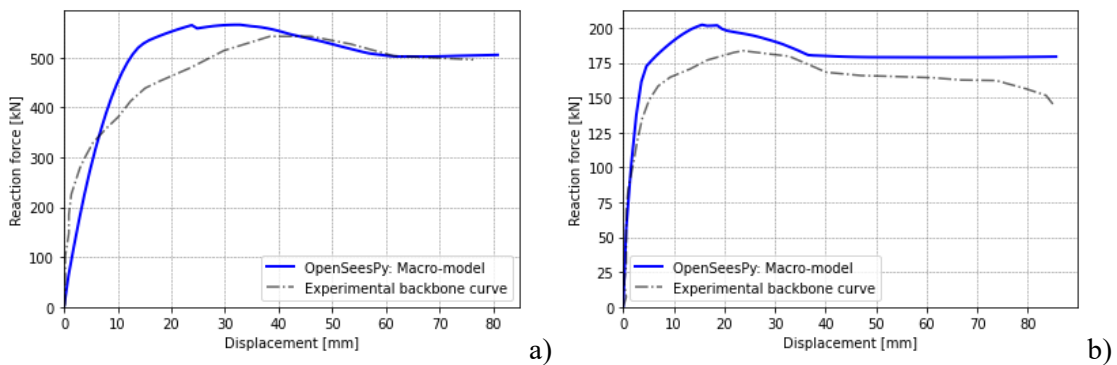


Figure 48. Experimental backbone curve and pushover curve by GA for specimens (a) TA2 (b) FIF

Table 11. RMSD value of referenced specimen using GA

References	Spec. number	RMSD Value
Cavaleri and Di. Trapani (2014)	S1A	191.43
Cavaleri and Di. Trapani (2014)	S1B	271.33
Mehrabi et al. (1996)	5	232.5
Mehrabi et al. (1996)	6	295.81
Mehrabi et al. (1996)	11	390.68
Colangelo (2005)	C1	293.32
Colangelo (2005)	L2	292.19
Colangelo (2005)	N1	369.75
Morandi et al. (2018)	TA2	1400.74
Di Trapani et al. (2023)	FIF	520.89

5.3 Calibration with Micro-Modal Analysis (Local Response) using GA

Numerical models must as closely as possibly simulate the behaviour of real-world structures and the physics that support them. Modeling technologies are just as important as experimental investigations, and when done correctly, they are the most cost-effective method of conducting research. The micro- model was also able to accurately predict the main cracking patterns in the masonry (bricks cracking and mortar joints sliding) as well as reinforced concrete members shear and flexural damage. However, these models necessitate the calibration of many parameters as well as extensive computational resources. As a result, micro-modelling methodologies are typically limited to certain study scopes and objectives. The micro-model uses a 2D scale damage model to simulate the non-linear behaviour of masonry components (units and mortar) and concrete members. The internal force was evaluated using a TCL script in the STKO post-processing module.

Normal stresses given by the infill to the column, shear demand at the column ends of an infilled frame increases significantly [Figure 49] and allows us to define a node set and collect nodal forces. The forces are then integrated across the given segment, which is known as a "cut"[30]. Because of this interaction, the shear diagram assumes a cubic trend in these locations, creating some uncertainty about the reference value to use as the nominal shear demand at the ends. To account for this uncertainty, the reference shear demand was

calculated as the average of the shear demand values obtained from three section cuts made at the ends and in the middle of a critical as shown in in Figure 49.

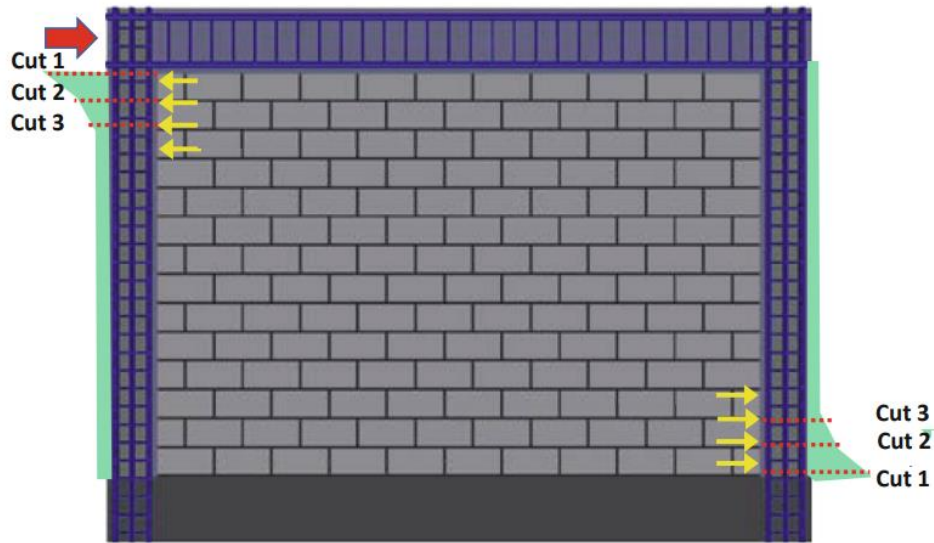


Figure 49. Identifying section cuts and predicting shear demand at infilled frame columns.

The results of OpenSees/STKO micro-model are shown below with damage, where the leeward and windward columns' section cut shear forces are also illustrated. As stated above, simple equivalent strut macro-models do not allow assessing local shear demand due to frame infill interaction. Hence, two non-diagonal struts are positioned in such a way that it the maximum shear on the column match with the refined micro-model. Figures below report the outcomes of the implementation of the macro-model to adjust the peak shear demand, in comparison with the actual shear demand derived from the micro-model. Though calibration results by using GA for all the referenced specimens shows good agreement between the micro-model and macro-model results in terms of local responses, deviation on the peak shear force on column by these two-modeling analysis is reported in Table 12.

- **Calibration with Cavaleri and Di Trapani specimens S1A and S1B**

Trapani et al. (2014) presented a study of the local shear effects produced at the ends of beams and columns of non-ductile RC-infilled frames under lateral loads. During his experimental campaign with S1 series specimens, he observed that considerable strength loss occurs only after a 1.8% drift. Crack propagation impacted both frames and infills. Initially, about diagonal cracks appeared on the frames at the higher joints. Corresponding diagonal cracks primarily impacted infills near mortar joints. For

bigger displacements (more than 20 mm), more visible cracking propagation, corresponding to the start of strength loss, was noted, along with the production of sub-horizontal cracks in the middle of columns and more severe damage at beam column junctions. For a single infilled frame, a comparison was made between the force arising in the frame members when an infill is treated as an equivalent concentric strut and when an infill is "exactly" modelled by finite shell components, at different drift levels. To express the local shear forces acting on beam and column ends as a fraction of the axial load experienced by the equivalent strut, it can be considered a basis for a predictive tool to be used for the assessment of shear demand on RC member critical sections that would otherwise be undetectable when a simple equivalent concentric strut model is used. An improved micro-model for the infilled frame specimens S1A and S1B was developed and implemented using OpenSees/STKO. The proposed micro-model, shown in Figure 51 (a) S1A and Figure 52 (b) S1B, enabled the evaluation of the internal force distribution over the frame, as well as the integration of nodal forces across a given cross-section. The shear-displacement curve obtained using the multi-struts micro-model by GA calibrate with the maximum shear force achieved on the column using multi-strut macro-model analysis, and the difference between peak shear force is shown in Table 12.

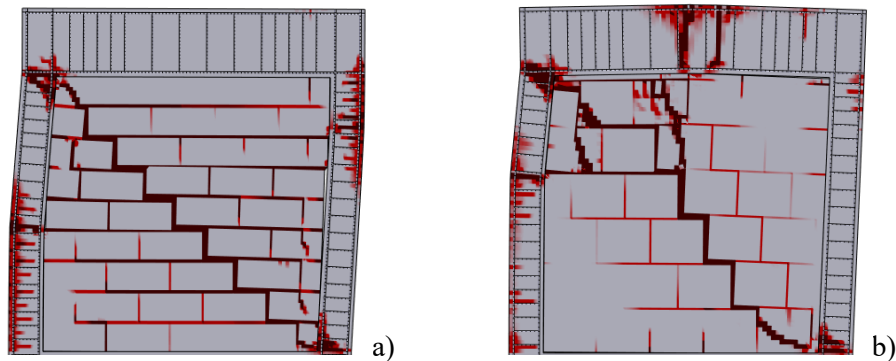


Figure 50. Micro-model analysis; damage pattern on infilled-frame specimen (a) S1A (b) S1B

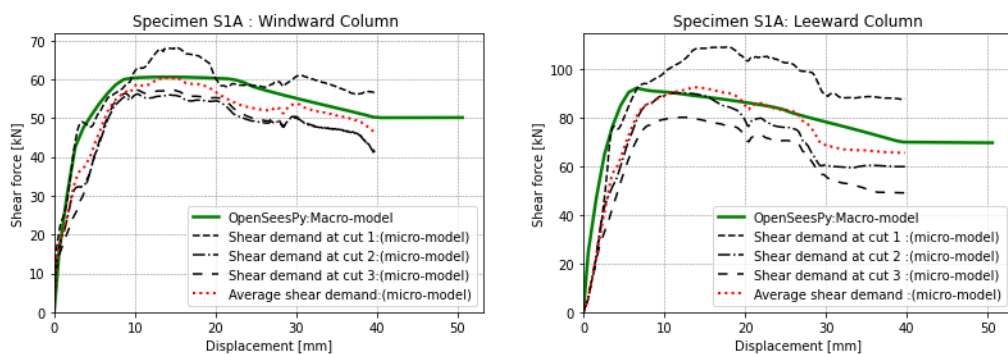


Figure 51. Shear demand calibration of macro model-GA with micro-model at column ends: S1A

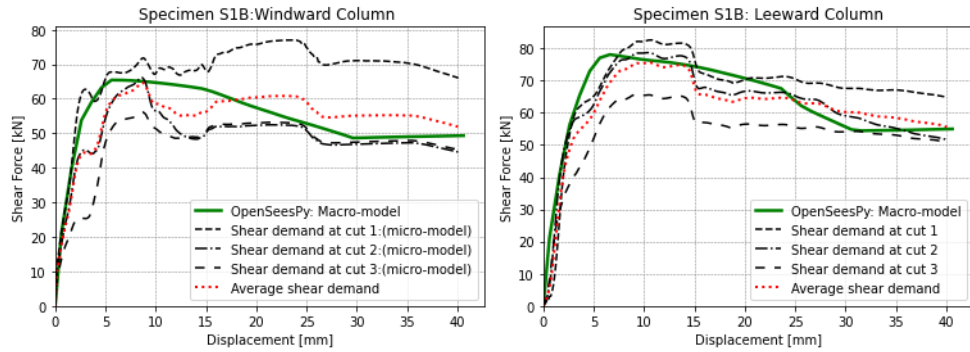


Figure 52. Shear demand calibration of macro model-GA with micro-model at column ends: S1B

- **Calibration with Mehrabi et al. specimens 5, 6 and 11**

Form experimental campaigning conducted by Mehrabi et al. (1996) specimens 5,6 and 11 are taken as reference for the calibration. On their research study for specimens 5 and 11 are weak frames and strong panels whereas specimen 6 had strong frame with weak panel. For specimen 5 and 11 diagonal sliding cracks in the infills were first observed at the maximum lateral loads and followed by the shear cracks in the columns. Due to the presence of the strong panel no shear failure was observed in the columns for specimen 6. The failure pattern of the specimens on the experiments is simulated in micro-model analysis [Figure 53-54] and the shear demand obtained by using GA on the columns shown in Figure 55 is compared with the micro-model shear-displacement curve. The difference in the maximum shear demand predicted by macro-model using GA and micro-model is in Table 12.

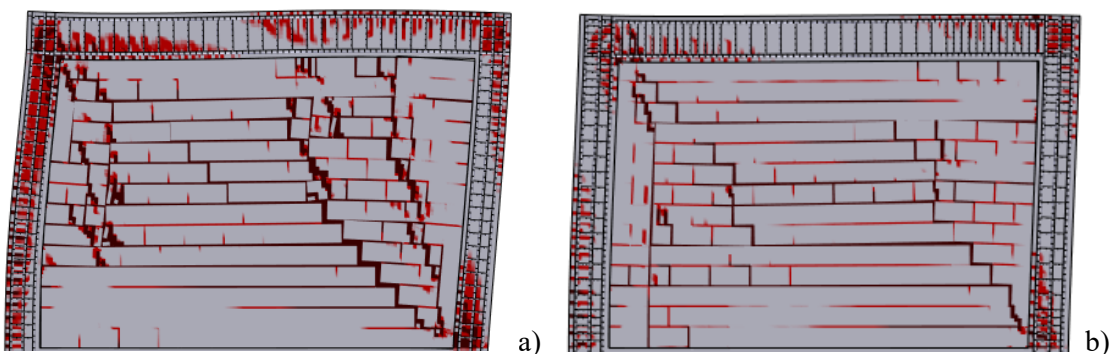


Figure 53. Micro-model analysis; damage pattern on infilled-frame specimen (a) 5 (b) 6

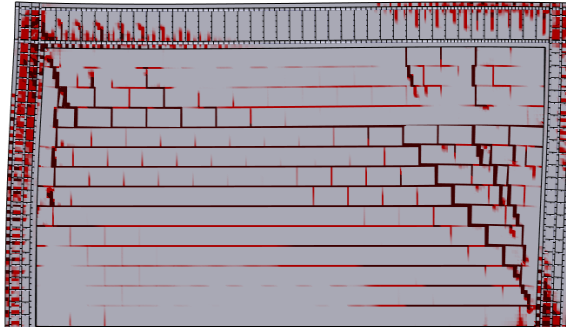


Figure 54. Micro-model analysis; damage pattern on infilled-frame specimen 11

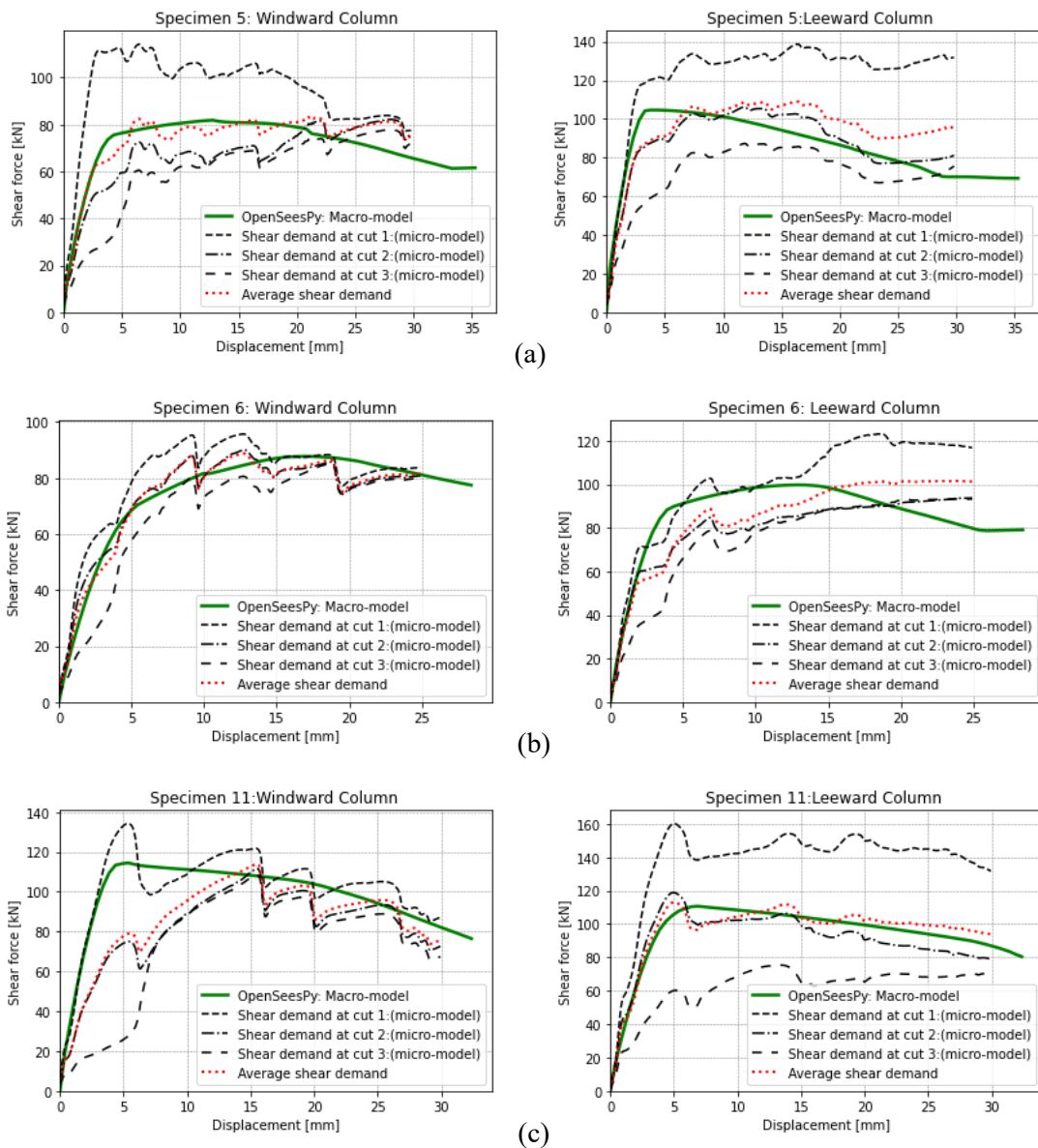


Figure 55. Shear demand calibration of macro model-GA with micro-model at column ends: (a) 5 (b) 6 (c) 11

- **Validation with Colangelo specimens C1, L2 and N1**

Seismic pseudo dynamic tests done by Colangelo for research study of infilled frame revealed that the referenced specimen C, L, and N frames, which were seismically resistant, only suffered flexural cracking at sight. A few cracks formed at the weak beam ends, some of which extended the whole depth of the cross-section. Columns fractured evenly along their height on the side not in contact with the infill. These cracks opened to a smaller extent, and most of them closed in the zero-force position. Longitudinal cracking was occasionally found in combination with lapped splices at the column bottom, including those on the N frames. During the test, infills were severely damaged. C1 specimen demonstrates Cracking damaged both bricks and mortar, and failure resulted in masonry crushing. Infills are found to influence the local deformation of frames, in addition to affecting global characteristics and responsiveness, as previously demonstrated. Micro-model analysis is done in OpenSees/STKO for all these referenced specimens [Figure 56]. The shear force at the columns determined by using GA for multi-strut macro-model is compared with the shear force-displacement average curve for the calibration shown in Figure 57 and difference of maximum shear demand between macro-model and micro-model is Table 12.

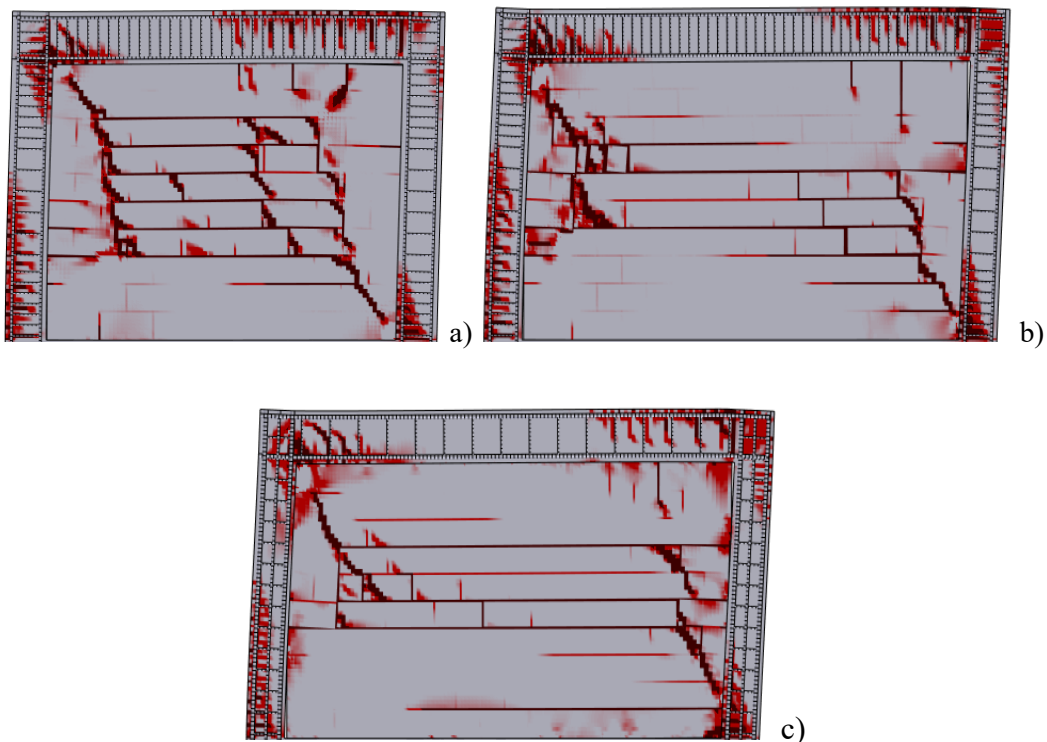


Figure 56. Micro-model analysis; damage pattern on infilled-frame specimen (a) C1 (b) L2 (c) N1

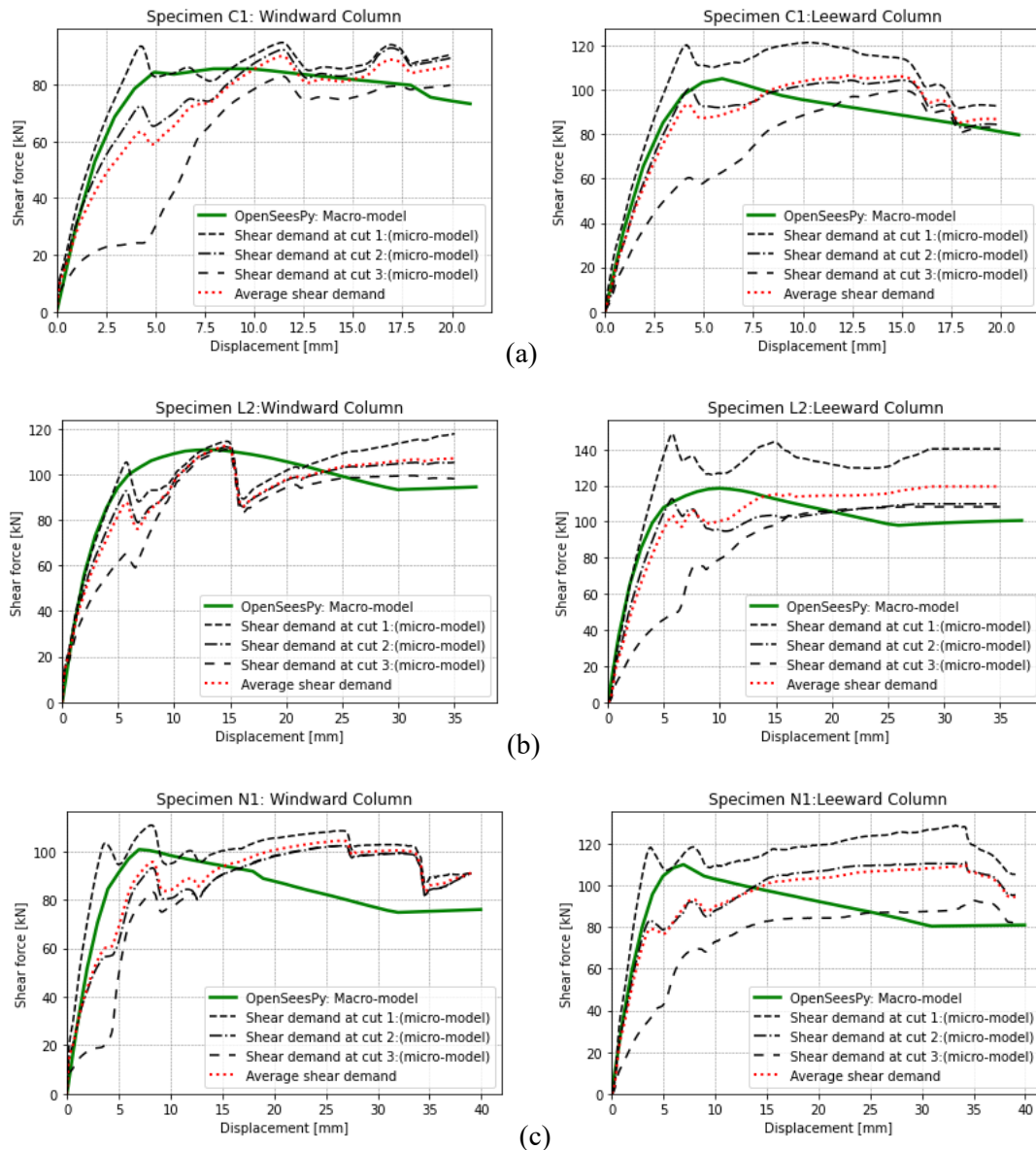


Figure 57. Shear demand calibration of macro model-GA with micro-model at column ends: (a) C1 (b) L2 (c) N1

- **Calibration with specimens TA2 and FIF**

Morandi et al. (2018) investigated the response of fully infilled frame TA2 taken as a reference for the solid infill specimens, was found to be characterised by a significant deformation capacity and a gradual attainment of a relatively high peak resistance, accompanied by slow and relatively low strength degradation, resulting in a substantial residual resistance, even at higher levels of drift. Even though no shear failure occurred, the strong infill's comparatively high resistance created the formation of diagonal shear

cracks in the RC columns as a result of the infill strut action. Trapani et al.'s (2023) examination on specimen FIF found that the infill began to crack lightly and separate from the surrounding frame quite early. The damage pattern revealed diagonal-stepped fissures caused by the mortar joints slipping, with no serious damage to the bricks. This sliding process persisted at high drift levels, resulting in the creation of new sliding fracture patterns. This behaviour is consistent with the specimen's ability to sustain high energy dissipation capacity, as it shows no significant post-peak resistance losses. The damage pattern at collapse revealed considerable mortar joint sliding, as well as localised brick crushing at the upper-right corners and the centre of the infill. There were also moderate shear and flexural cracks at the columns' mid-height and the top. The representation of infilled frames can be achieved by a variety of numerical modelling techniques, ranging from complex micro-modelling to simple macro-modelling methods. For each of these referred specimens, a micro-model analysis is performed in OpenSees/STKO [Figure 58]. The multi-strut macro-model's determined shear force by using GA at the columns is compared to the calibration's shear force-displacement average curve [Figure 59-60], and Table 12 shows the difference in maximum shear demand between the macro modal and micro-models.

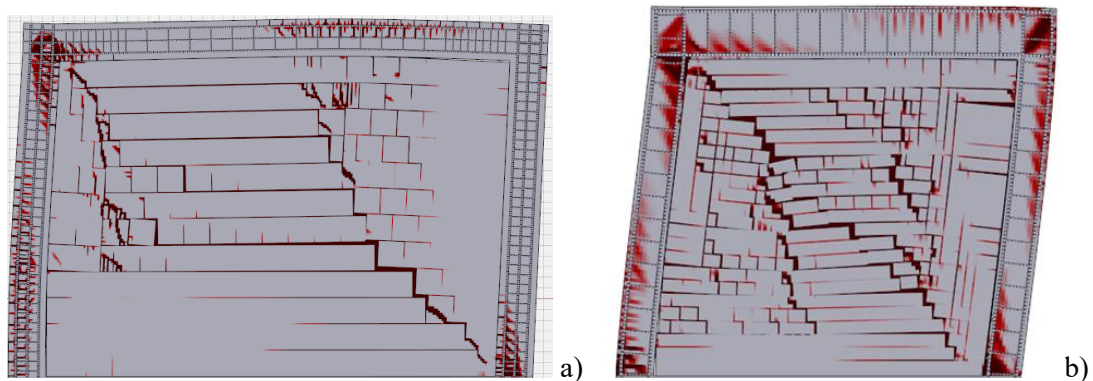


Figure 58. Micro-model analysis; damage pattern on infilled-frame specimen (a) TA2 (b) FIF

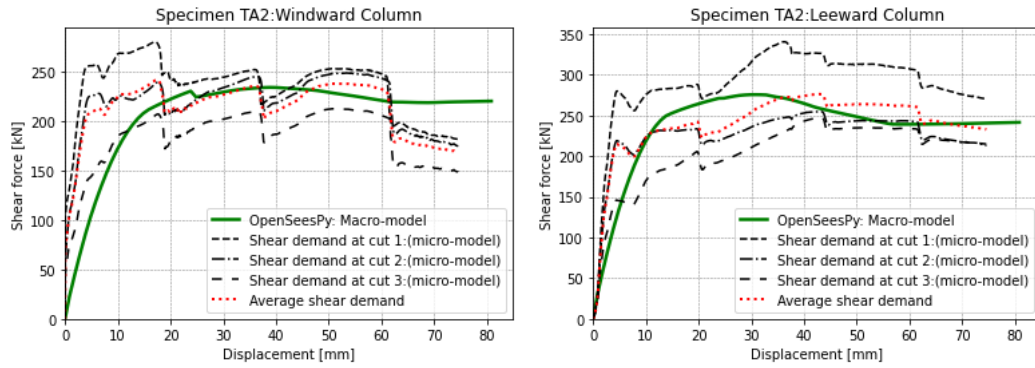


Figure 59. Shear demand calibration of macro model-GA with micro-model at column ends: TA2

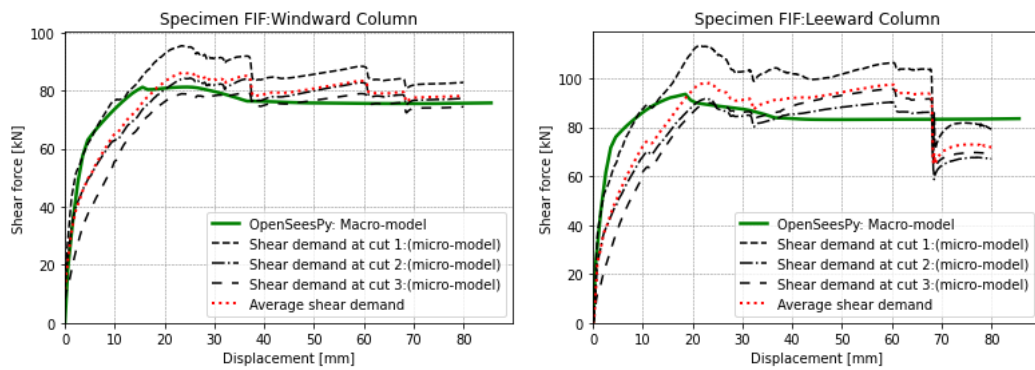


Figure 60. Shear demand calibration of macro model-GA with micro-model at column ends: FIF

Table 12. Maximum shear force comparison between micro model and GA macro modal

References	Spec. number	Windward Column max. shear (kN)			Leeward Column max. shear (kN)		
		Macro-model	Micro-model	Difference %	Macro-model	Micro-model	Difference %
Cavaleri and Di. Trapani (2014)	S1A	60.47	60.59	-0.2	92.59	92.29	+0.3
Cavaleri and Di. Trapani (2014)	S1B	64.64	65.43	-1.2	75.60	78.09	-3.2
Mehrabi et al. (1996)	5	83.14	84.85	+1.5	108.89	104.58	+3.9
Mehrabi et al. (1996)	6	88.81	87.77	+1.1	101.60	99.74	+1.8
Mehrabi et al. (1996)	11	113.97	114.51	-0.5	113.02	110.64	+2.1
Colangelo (2005)	C1	90.08	85.63	+4.5	106.42	105.03	+1.3
Colangelo (2005)	L2	112.50	110.82	+1.5	119.43	118.48	+0.8
Colangelo (2005)	N1	104.43	100.81	+3.5	110.03	110.12	-0.8
Morandi et al. (2018)	TA2	241.900	234.27	+3.2	276.20	275.48	+0.26
Di Trapani et al. (2023)	FIF	86.12	81.17	+5.7	98.12	93.52	+4.6

5.4 Validation of the Proposed Model

To achieve the best outcome in terms of both global and local response, the relationship between the weightage p_1 , p_2 , and p_3 [Figure 42] of each strut is found using various trial and error techniques based on the aspect ratio (l'/h') of the RC frame. The length to height ratio (l'/h') is plotted against the weightage of p_1 , p_2 , and p_3 , and relationship that results is as follows.

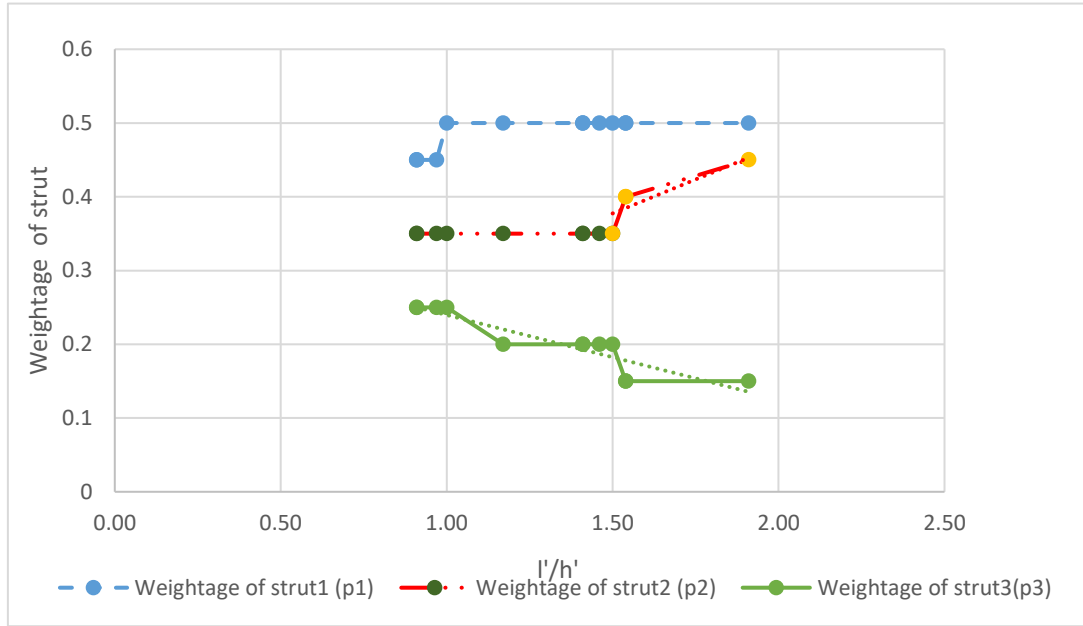


Figure 61. Relationship between strut weightage and the aspect ratio of the RC frame.

$$\tilde{p}_1 = \begin{cases} 0.45 & \text{if } \frac{l'}{h'} \leq 1 \\ 0.50 & \text{if } \frac{l'}{h'} > 1 \end{cases} \quad (35)$$

$$\tilde{p}_2 = \begin{cases} 0.45 & \text{if } \frac{l'}{h'} \leq 1.5 \\ 0.184 \left(\frac{l'}{h'} \right) + 0.1 & \text{if } \frac{l'}{h'} > 1.5 \end{cases} \quad (36)$$

$$\tilde{p}_3 = -0.11 \left(\frac{l'}{h'} \right) + 0.35 \quad (37)$$

Table 13 displays the updated weightage \tilde{p}_2 and \tilde{p}_3 mainly for strut2 and strut3, based on the above relation.

Table 13. Updated weightage of each equivalent struts

References	Specimen ID	$\frac{l'}{h'}$	\tilde{p}_1	\tilde{p}_2	\tilde{p}_3
Cavaleri and Di. Trapani (2014)	S1A	0.91	0.45	0.35	0.25
Cavaleri and Di. Trapani (2014)	S1B	0.91	0.45	0.35	0.25
Di Trapani et al. (2023)	FIF	0.97	0.45	0.35	0.24
Colangelo (2005)	C1	1.17	0.5	0.35	0.22
Mehrabi et al. (1996)	S5	1.41	0.50	0.35	0.19
Mehrabi et al. (1996)	S6	1.41	0.50	0.35	0.19
Morandi et al. (2018)	TA2	1.46	0.50	0.35	0.18
Colangelo (2005)	L2	1.54	0.50	0.39	0.18
Colangelo (2005)	N1	1.54	0.50	0.39	0.18
Mehrabi et al. (1996)	S11	1.91	0.50	0.45	0.13

The position d_1 , d_2 , and b_1 , b_2 of the off-diagonal struts for the various specimens are previously determined using the genetic algorithm (GA) with the pre-defined weightage p_1 , p_2 , p_3 of the equivalent struts for the proposed multi-strut macro model [Figure 42] in order to obtain the optimal solution with respect to both the global and local response. A new empirical equation is found out by using the position (d_1, d_2, b_1, b_2) from the GA to estimate the ideal position of the off-diagonal struts is as follows.

$$\tilde{d}_1 = 49.39 \left(\frac{l'}{h'} \right)^3 + \frac{1}{0.39 \cdot \frac{f_b}{f_m} - 0.37} + 227.18 \quad (38)$$

$$\tilde{d}_2 = \frac{1}{-0.0048\lambda^* + 0.017} + \frac{1}{-0.039 \cdot \frac{f_b}{f_m} + 0.063} + 153.59 \quad (39)$$

$$\tilde{b}_1 = 0.96d_1 - 74.04 \quad (40)$$

$$\tilde{b}_2 = 0.82d_2 - 55.80 \quad (41)$$

λ^* can be determined according to equation 18.
 f_b is the compressive strength of masonry unit.

f_m is the compressive strength of the masonry.

The off-diagonal strut's new positions \tilde{d}_1 , \tilde{d}_2 , \tilde{b}_1 , \tilde{b}_2 are evaluated using the analytical equation above, which is shown in Table 14. Figure 62 illustrates the discrepancy between the position of the off-diagonal struts generated by GA and the empirical equation of proposed model.

Table 14. Updated position of off-diagonal struts evaluated by empirical equation.

References	Specimen ID	$\frac{l'}{h'}$	\tilde{d}_1	\tilde{d}_2	\tilde{b}_1	\tilde{b}_2
Cavaleri and Di. Trapani (2014)	S1A	0.91	266.44	481.56	180.89	340.76
Cavaleri and Di. Trapani (2014)	S1B	0.91	464.20	344.94	370.11	228.26
Di Trapani et al. (2023)	FIF	0.97	274.74	260.39	188.84	158.63
Colangelo (2005)	C1	1.17	301.43	240.33	214.37	142.11
Mehrabi et al. (1996)	S5	1.41	325.81	350.59	237.70	232.91
Mehrabi et al. (1996)	S6	1.41	371.93	330.15	281.82	216.08
Morandi et al. (2018)	TA2	1.46	370.46	249.72	280.42	149.85
Colangelo (2005)	L2	1.54	402.35	238.31	310.93	140.45
Colangelo (2005)	N1	1.54	400.29	241.46	308.96	143.04

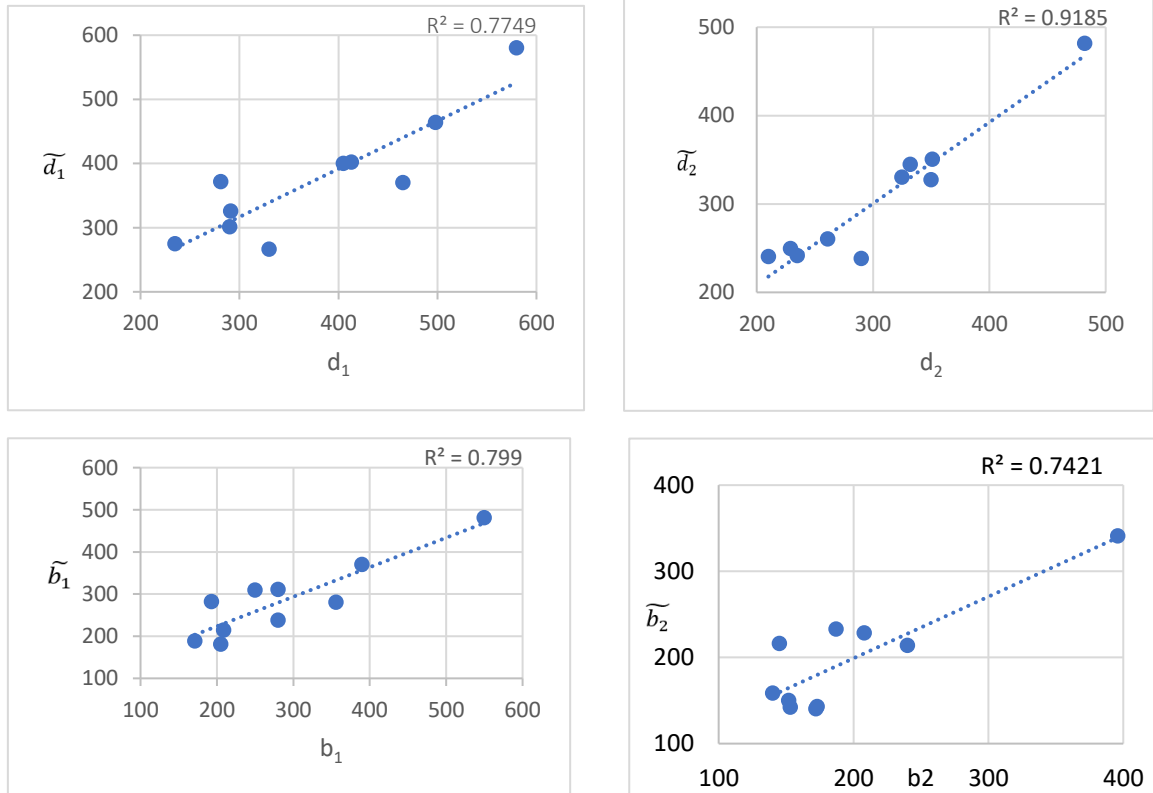


Figure 62. Non-diagonal struts position discrepancy between GA and proposed analytical equation.

With the new relation for the weightage of each equivalent strut (\tilde{p}_1 , \tilde{p}_2 and \tilde{p}_3) and using the analytical equation to find the optimum position of off diagonal struts (\tilde{d}_1 , \tilde{d}_2 , \tilde{b}_1 , \tilde{b}_2) for all 10 specimen of the proposed model is again validated with the experimental data and the micro-model. The outcomes force-displacement curves and shear-displacement curves are plotted for each specimen and shown in figures below with the position of strut and deformation frames after pushover analysis completed.

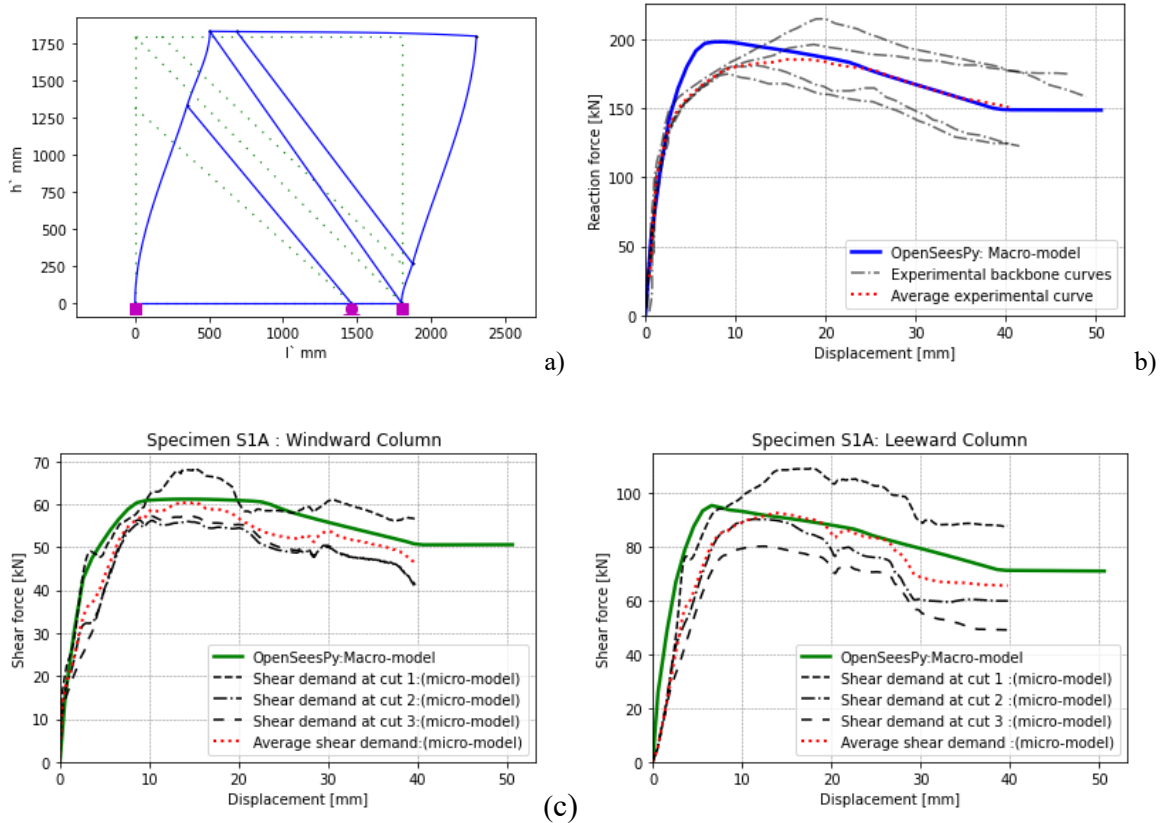


Figure 63. Validation of proposed model for specimen S1A (a) struts-frame orientation (b) global response (c) local response

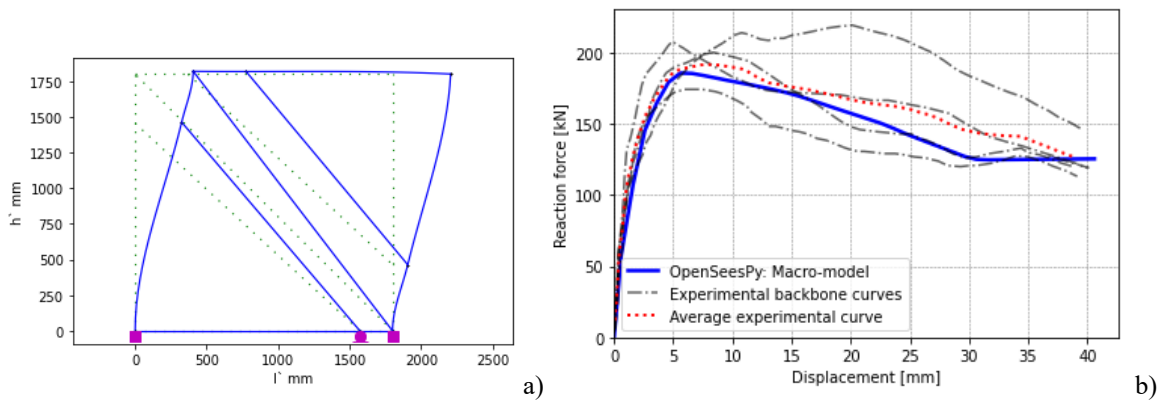


Figure 64. Validation of proposed model for specimen S1B (a) struts-frame orientation (b) global response

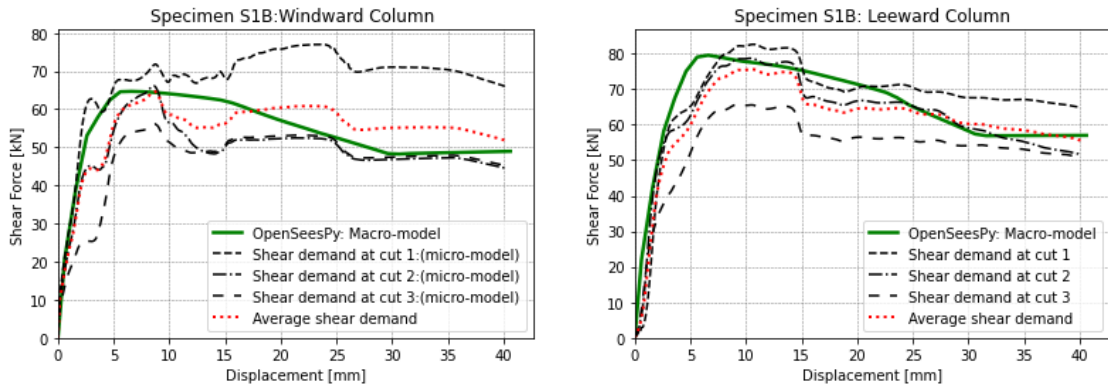


Figure 65. Validation of proposed model for specimen S1B local response

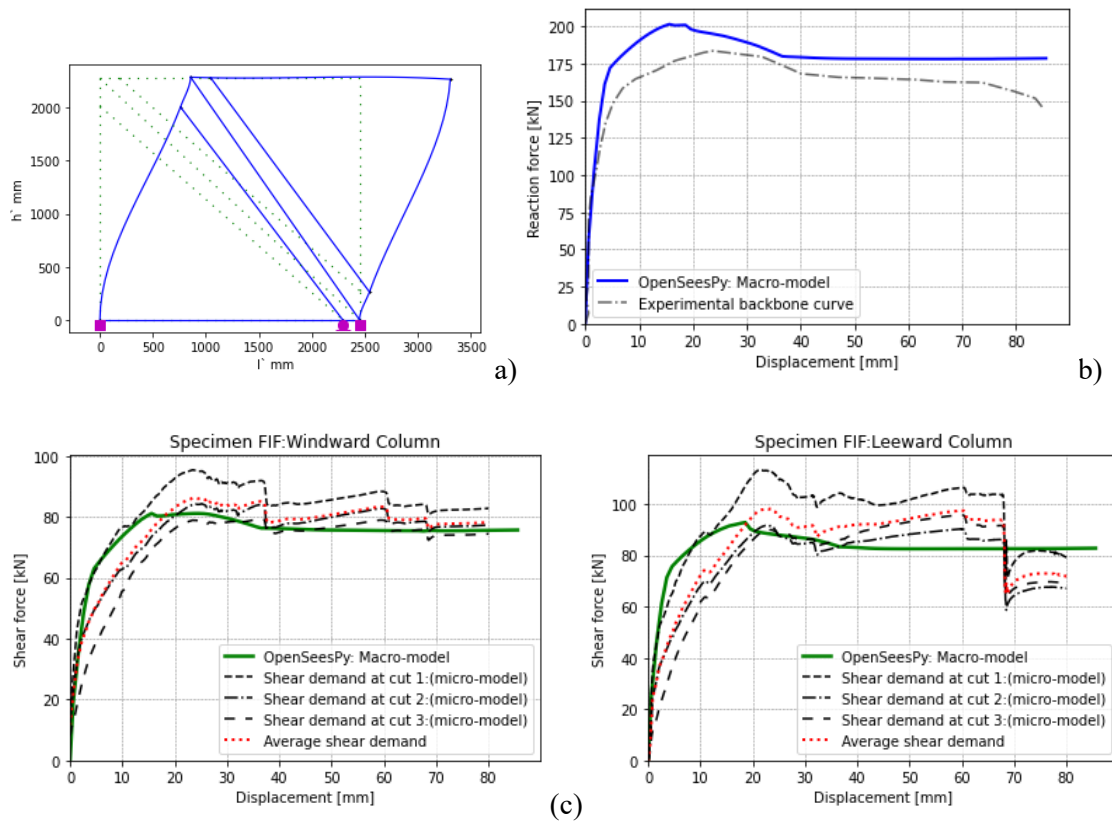


Figure 66. Validation of proposed model for specimen FIF (a) struts-frame orientation (b) global response (c) local response

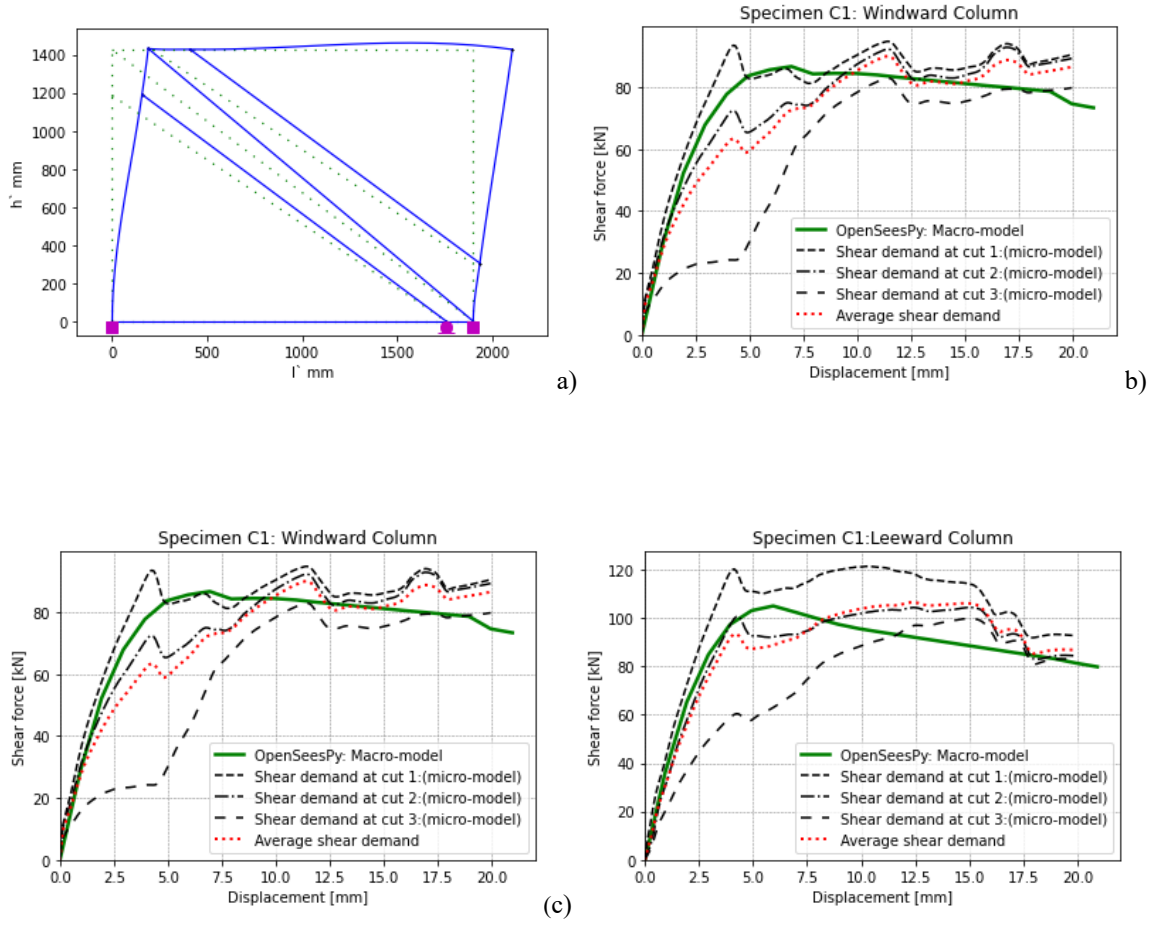


Figure 67. Validation of proposed model for specimen 5 (a) struts-frame orientation (b) global response (c) local response

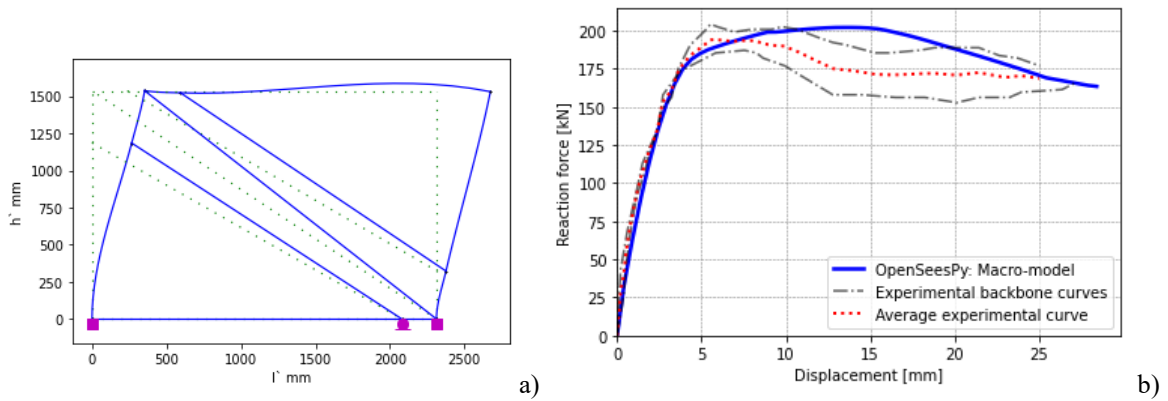


Figure 68. Validation of proposed model for specimen 6 (a) struts-frame orientation (b) global response

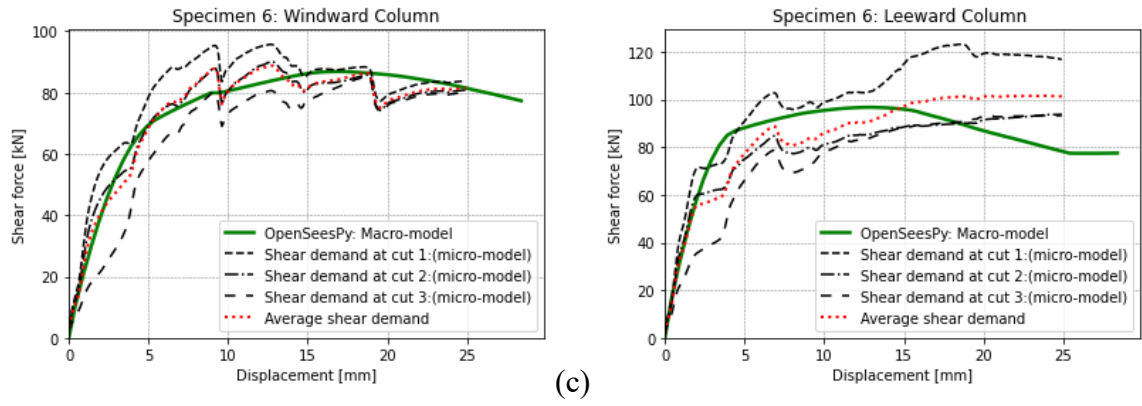


Figure 69. Validation of proposed model for specimen 6 local response

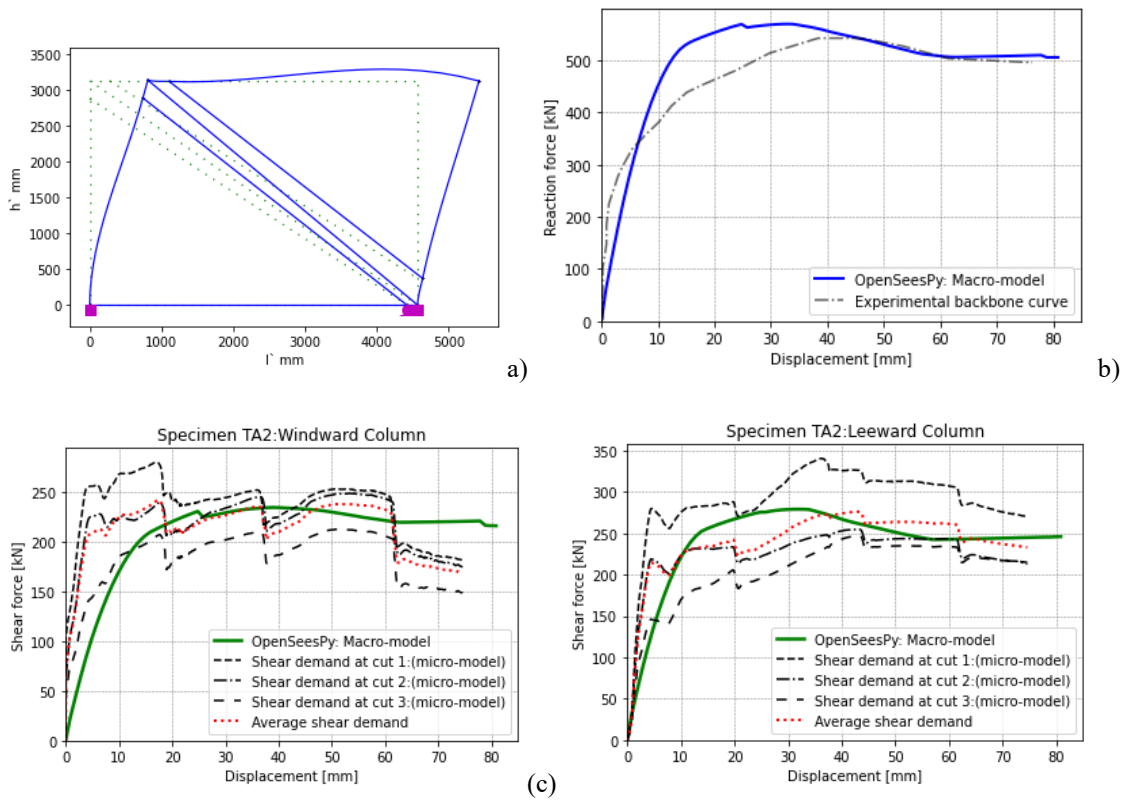


Figure 70. Validation of proposed model for specimen TA2 (a) struts-frame orientation (b) global response (c) local response

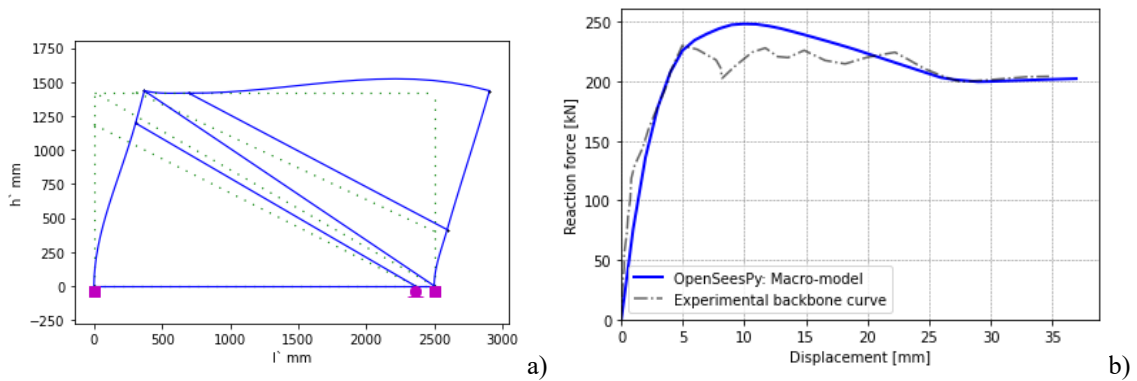


Figure 71. Validation of proposed model for specimen L2 (a) struts-frame orientation (b) global response

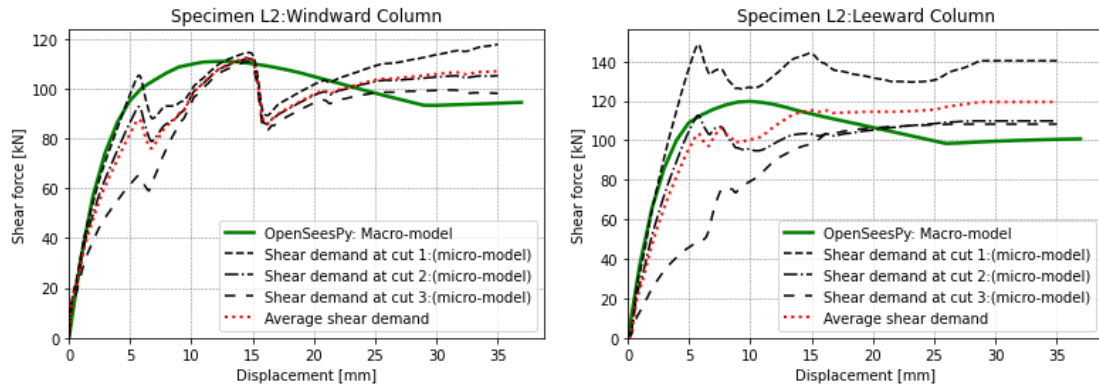


Figure 72. Validation of proposed model for specimen L2 local response

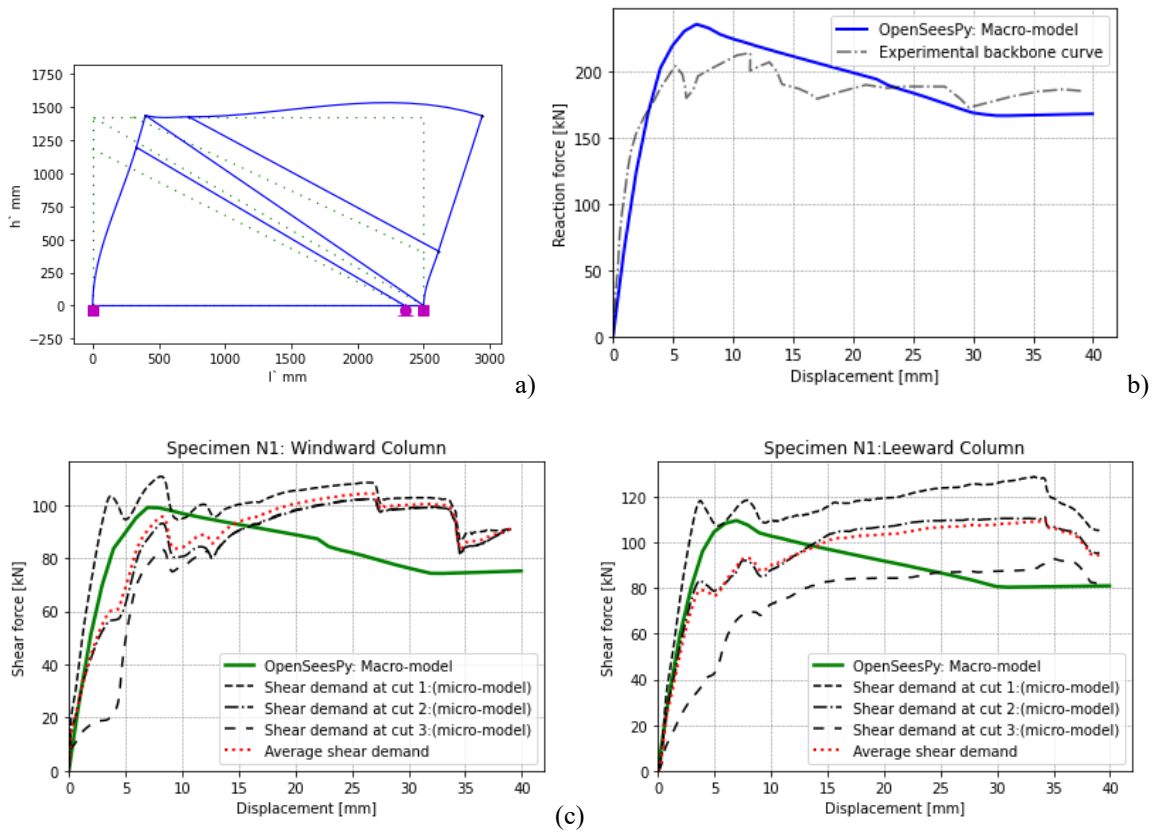


Figure 73. Validation of proposed model for specimen N1 (a) struts-frame orientation (b) global response (c) local response

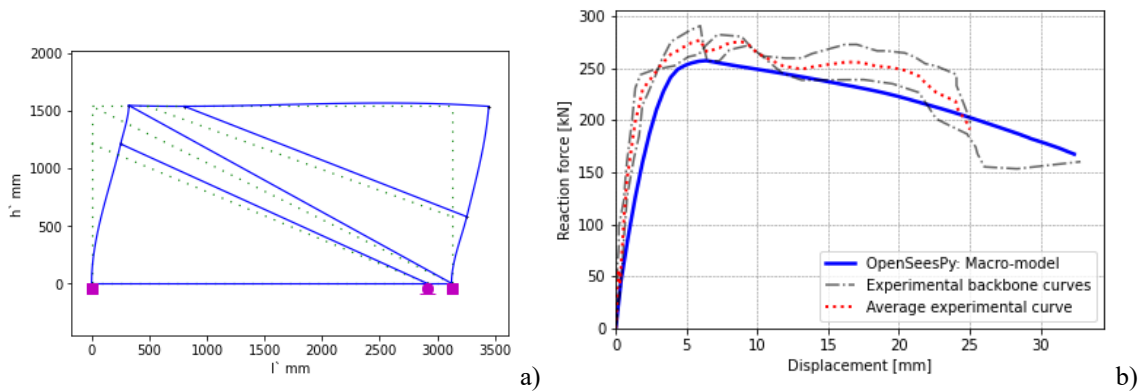


Figure 74. Validation of proposed model for specimen 11 (a) struts-frame orientation (b) global response

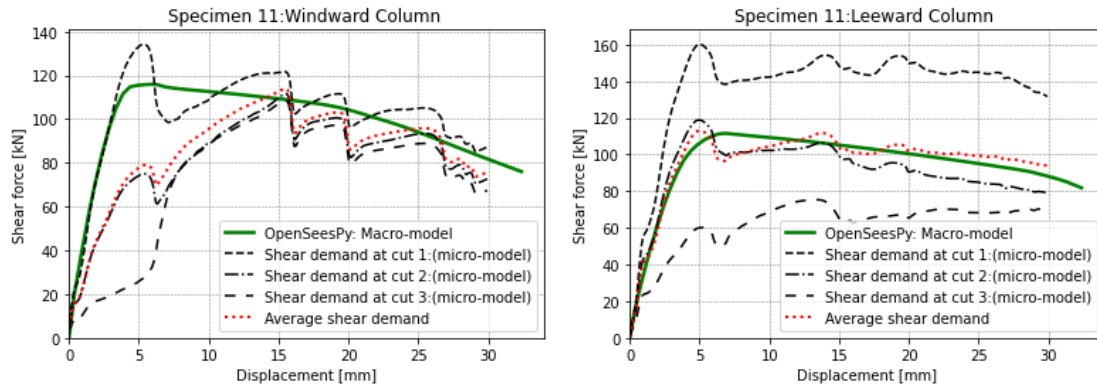


Figure 75. Validation of proposed model for specimen 11 local response

Lastly, Table 15 displays the error on the local and global responses of referenced specimen as determined by the empirical equation and the GA. Errors are represented on histogram for examining potential error would be necessary for a comprehensive evaluation of the model's performance.

Table 15. GA and proposed modal error for global and local response

Specimen ID	RMSD GA	RMSD Proposed model	Windward column shear (V) [kN]		Leeward column shear (V) [kN]		$\frac{RMSD_{p.model}}{RMSD_{GA}}$	maximum $\frac{(V_{W,p.model})}{(V_{W,GA})}$	maximum $\frac{(V_{L,p.model})}{(V_{L,GA})}$
			GA	Proposed model	GA	Proposed model			
S1A	191.43	221.19	60.59	61.19	92.29	95.41	1.16	1.01	1.03
S1B	271.33	248.94	65.43	64.68	78.09	79.55	0.92	0.99	1.02
FIF	520.89	502.58	81.17	81.08	93.52	92.83	0.96	1.00	0.99
C1	293.32	289.01	85.63	86.62	105.03	104.93	0.99	1.01	1.00
5	232.5	248.96	81.85	81.33	104.58	104.81	1.07	0.99	1.00
6	295.81	253.24	87.77	86.88	99.74	96.72	0.86	0.99	0.97
TA2	1400.74	1345.73	234.27	234.6	275.48	279.05	0.96	1.00	1.01
L2	292.19	326.93	110.82	111.03	118.48	119.76	1.12	1.00	1.01
N1	369.75	382.37	100.81	99.14	110.12	109.7	1.03	0.98	1.00
11	390.68	411.83	114.51	115.95	110.64	111.57	1.05	1.01	1.01

Summarizing, genetic algorithm (GA) is used to find the optimum position (d_1 , d_2 , b_1 , b_2) for the calibration with the experimental and refined model data. The fitness function simulates a structural model with specified parameters and computes fitness based on the difference between experimental data and model predictions. The optimisation method includes population size, number of generations, mutation rate, and number of parents mating, as stated in Chapter 4. The GA instance is initialised using the provided parameters and fitness function before beginning the optimisation process. The best solution i.e. d_1 , d_2 , b_1 , b_2 found by the GA is extracted and saved for further analysis. The convergence history of the GA is shown, demonstrating how the fitness value evolves over generations. The

optimization process aims to find the structural configuration that best matches experimental observations, contributing to the refinement and validation of the model. The optimisation method aims to identify the structural configuration that accurately fits experimental observations, hence contributing to model refinement and validation. The fitness function in this context evaluates the performance of a model by quantifying how well its predictions match experimental observations and the refined model. Fitness value of referenced specimen for the GA calibration and for validation of the proposed model is in Table 16. Higher fitness score offers superior solutions for the optimisation.

Table 16. Referenced specimen fitness value for GA and proposed model

Specimen ID	Fitness value for GA	Fitness value for proposed model
S1A	193.93	242.41
S1B	291.01	272.98
FIF	604.79	591.02
C1	339.86	318.69
5	277.73	284.26
6	303.00	294.13
TA2	1372.02	1406.34
L2	329.44	329.44
N1	415.37	416.09
11	455.84	432.40

Figure 76 illustrates the histogram representing RMSD errors based on the GA and the proposed modal for the global response. It appears to be skewed, with a small tail towards larger error values. This shows that while the majority of the data points may have smaller RMSD errors, there are also some instances of higher errors. The central tendency of the distribution can be determined through the position of the peak or centre of the distribution, which appears to be between 0.95 and 1.0. Bars are relatively evenly spread across the range of error values, indicating moderate variability in the RMSD errors.

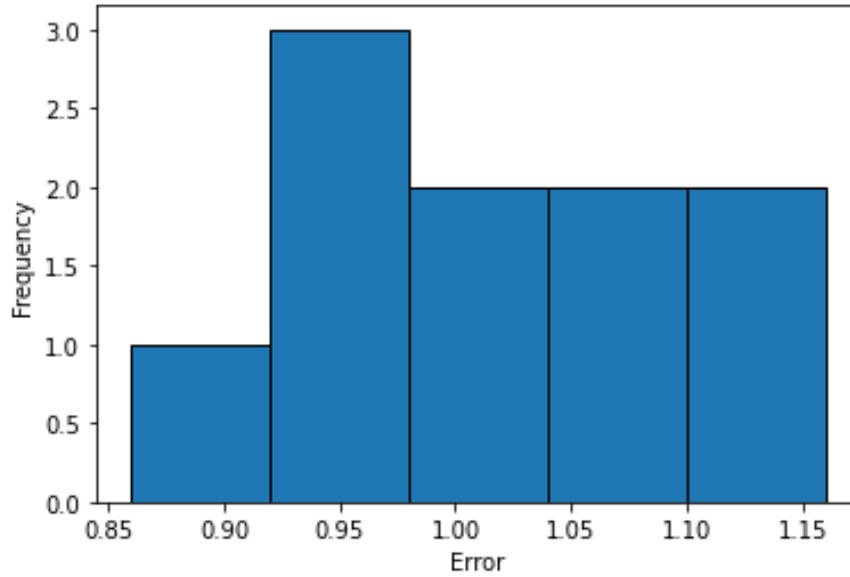


Figure 76. Histogram: error between GA and proposed model for global response

According to the GA and the suggested modal, Figure 77 and Figure 78 respectively show the histogram of windward and leeward column shear errors. The shape of histogram for windward column appears to be relatively symmetric, with most of the error concentrated around the center of the distribution. There is minimal skewness observed in the histogram. The distribution's centre or peak, which appears to be in the range of 0.99 to 1.00, is useful to determine the distribution's central tendency. Bars show a moderate degree of variability in the Windward column shear errors, with a rather even distribution across the error levels.

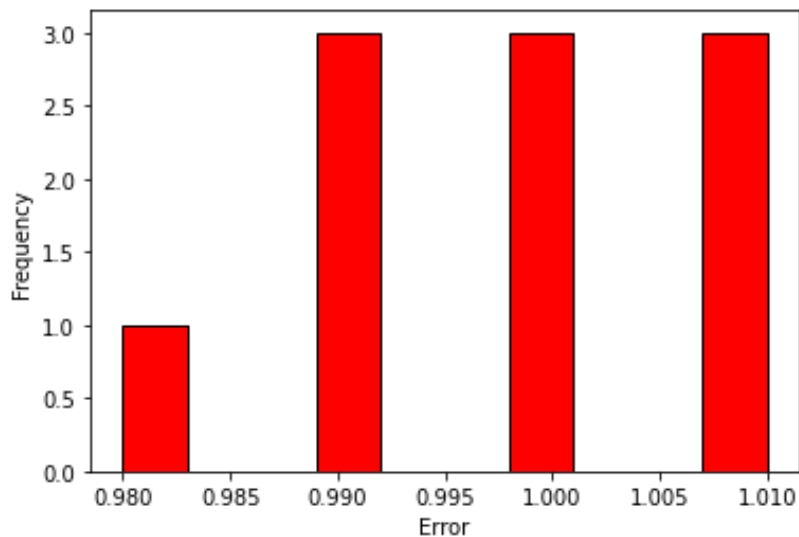


Figure 77 . Histogram: error between GA and proposed model for local response on windward column

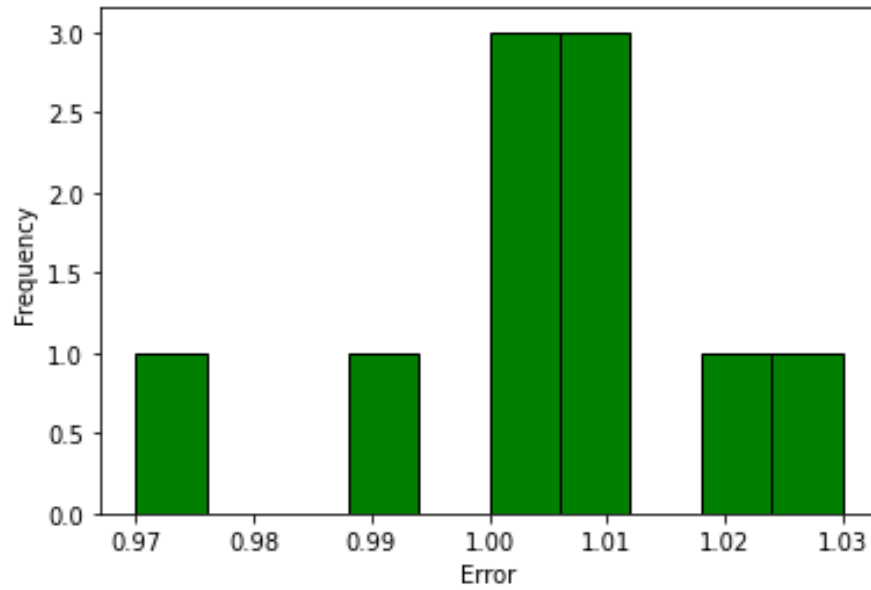


Figure 78. Histogram: error between GA and proposed model for local response on leeward column

The shape of the distribution of leeward column histogram is similar to a bell-shaped curve. Most of the data seems to be concentrated around the center of the distribution. The peak or centre of the distribution can be used to determine the distribution's central tendency. Based on this histogram, it appears that the distribution's peak is in the 1.00–1.101 range. The considerable variability in the Leeward column shear errors is indicated by the bars in this instance, which are split evenly across the error values.

CHAPTER 6

Conclusion

6.1 Summary of Key Findings

The primary objective of this thesis is to provide a multi-strut macro model and empirical formulas for seismic modelling of infilled RC frames that can accurately simulate the impact of non-structural masonry infills on the seismic behaviour of reinforced concrete framed structures. The suggested model is based on past experimental results. The infill wall was represented by three diagonal struts per direction, which simulated both global and local responses. Over the last seventy years, a large literature on mathematical modelling of infills has emerged. The various proposed models can be grouped into two categories: local or micro-models and simplified or macro-models. The first group includes models in which the structure is divided into multiple components to account for the local effects in detail. The second group contains simplified models based on the physical load transfer mechanism of the infill panel.

To account for the masonry panel's elastic in-plane stiffness, some codes and regulations require the use of a single equivalent diagonal compression strut. However, the shear demand caused by the frame-infill interaction cannot be determined using standard equivalent strut models, and the micro-modeling approach is too computationally demanding to be used in reality. Hence, the macro-models that can be employed in everyday engineering are extremely useful and additional shear demand resulting from the interaction between the frame and infill is crucial when assessing infill RC frames, as it may be responsible of local failures at the column ends and the joints. The simplest are the three equivalent-strut models, one of which represents diagonal infills and the other non-diagonal. The equivalent width of these struts determines their stiffness and strength, as well as the position of the non-diagonal struts which trigger shear demand.

The empirical formulas were developed and verified using considerable experimental data collected from earlier studies in the literature. A database of ten infilled frame specimens with varying typology, geometry, and mechanical properties was used as a reference. The shear parameters for each reference specimen were obtained through numerical calibration using genetic algorithm (GA). Following that, several trial-and-error tests are conducted to produce the relation for the weight of the struts to the aspect ratio of the frame. Genetic

algorithm was used to determine the optimal position of non-diagonal struts that resulted in the highest shear demand which is calibrated with the micro model and the empirical formula is validated with the results of GA. The proposed macro-model can accurately estimate the position of struts where the maximum shear force is triggered during earthquake.

6.2 Implications of Findings

A major issue is the "local" interaction between the infill panel and the surrounding structural elements in proximity of the nodes connecting the beams to the columns. Under horizontal load, the infill masonry's separation from the surrounding frame results in a concentration of load transfer and an increase in the shear demand on the structural elements, making them more vulnerable to brittle failures. This is especially important in buildings intended to support vertical loads alone, such as those constructed in the 1980s, since the constructive practice states that stirrup distribution within the structural elements is usually inadequate and inefficient. The equivalent model with a single concentric strut considered thus far is a simplified description of the non-structural panel within the frame, which is suitable to reflect the structure's overall response but cannot describe the above-mentioned phenomenon of local interaction.

This calibration study proposed a multi-strut equivalent macro model based on the axial-force-displacement relationship for triple struts to compute the weightage of each strut in the function of the length-to-height (l/h) ratio of the RC frame. The model is easily implemented in the majority of finite element computational methods that handle nonlinear frame structure analysis. The model was finally validated with ten blind prediction lateral-force-displacement tests, and the shear force on the column was validated using micro-model analysis. The validation results illustrate a good agreement between the analytical and experimental results for both global and local responses. The stiffening and strengthening impact, which influences the column's global displacement capacity, differs slightly from the experimental results. Also, the obtained shear force on the column by non-diagonal struts is not significantly different from the value generated by the micro-model.

The direct experience of earthquake-related damage to real buildings has tremendously helped in clarifying the function of non-structural infills, both in seismic response and in the characterization of structural damage. The in-plane behaviour of the masonry infill walls was researched in order to gain a thorough understanding of their interaction with the surrounding frames and nonlinear behaviour during an earthquake. The introduction to this

work provides a quick explanation of the important parameters, i.e. the weightage of the three struts, that should be considered while developing mathematical models that simply demonstrate the complexity of the task at hand.

A brief state-of-the-art assessment of existing macro- and micro-modeling was conducted. It has been found that micro-models allow for more accurate findings, although they demand additional computational efforts. The macro-models are capable of reproducing the true behaviour of these non-structural elements with high accuracy while using less computational resources and time. As a result, the multi-strut micro model is effective in estimating the exact maximum shear force on the columns in an efficient time.

6.3 Recommendations for Future Research

This macro-model study of infilled frame governs the in-plane behaviour of RC frame structure in terms of masonry-induced shear force at columns end. It is evident that there is a lot more to do with the infilled reinforced concrete construction. This section provides recommendations and future study suggestions for investigating the effects of infill walls on the performance of reinforced concrete buildings. Some of these recommendations are outlined below.

- Plaster on walls can be taken into account while determining the equivalent struts and material constitutive law.
- Three strut model give good results on calibration for infill walls considered as full without opening. However, the calibration study can be done for the wall with openings.
- The suggested method will be validated in a dynamic field simulation of seismic activity using spectral analysis.

Appendix A. *Openseespy* code for the multi-strut macro model generation

An example of *Openseespy* code used to define the multi-strut model is provided here.

Specimen S1B is used as a sample for the code.

```
import openseespy.opensees as ops
import math
import pandas as pd
import numpy as np
from scipy.interpolate import interp1d
import opsviz
import matplotlib.pyplot as plt

def multi_structs_model(**kwargs):

    ops.wipe()
    ops.model('basic', '-ndm', 2, '-ndf', 3)

#####
# GEOMETRY
#####
    Span = 1800.0      # [mm] c/c length
    Storey = 1800.0   # [mm] c/c height

    # Vertical axes, x
    x1 = 0.0
    x2 = x1 + Span

    # Horizontal axes, y
    y1 = 0.0
    y2 = y1 + Storey

    l = 1600.0
    h = 1600.0
    d1 = kwargs.get('d1', h/4)
    b1 = kwargs.get('b1', l/4)
    d2 = kwargs.get('d2', h/4)
    b2 = kwargs.get('b2', l/4)

    # NODES
    ops.node(1, x1, y1, 0)
    ops.node(2, x2, y1, 0)
    ops.node(3, x1, y2, 0)
    ops.node(4, x2, y2, 0)
    ops.node(5, x1+b1, y2, 0)
    ops.node(6, x2, y1+d1, 0)
    ops.node(7, x1, y2-d2, 0)
    ops.node(8, x2-b2, y1, 0)

    # CONSTRAINS
    ops.fix(1, 1, 1, 1)
    ops.fix(2, 1, 1, 1)
    ops.fix(8, 0, 1, 0)
```

```
#####
# MATERIALS
#####
IDconcCore = 1
IDconcCover = 2
IDreinf = 3
IDmason = 4
#-----
# Basic Concrete Properties (cover concrete)
fpc = -25.0      # [MPa] (+Tension;-Compression)
epsc0 = -0.0025 # strain at maximum stress in compression
fpcu = -17.0    # [MPa] ultimate stress for unconfined concrete
epscU = -0.012  # strain at ultimate stress in compression

# Confined Concrete Properties (core concrete)
fc1C = -28.0    # Confined concrete (mander model),maximum
epscC = -0.004 # strain at maximum stress in compression
fpc1C = -18.0   # ultimate stress for confined concrete
eps1CU = -0.024 # strain at ultimate stress
lamda = 0.1     # ratio between unloading slope at $eps2 and initial slope
#-----
# Steel Properties
Fy = 450.0      # [MPa] Steel yield stress
Es = 210000.0   # [MPa] modulus of steel
b = 0.001       # strain-hardening ratio
# control the transition from elastic to plastic branch between 10 and 20
R0 = 15.0
cR1 = 0.925
cR2 = 0.15
#-----
# Strut Property
StrDepth = 150      # [mm] Depth of the section
StrWidth = 664.07   # [mm] Width of the section
fpcM = -2.28        # [MPa] (+Tension;-Compression)
epsc0M = -0.0013    # strain at maximum stress in compression
fpcuM = -1.02       # [MPa] ultimate stress for unconfined concrete
epsUM = -0.0074     # strain at ultimate stress in compression
lamdaM = 0.085
#-----

# CONCRETE (matType, matTag, *matArgs)
# Cover concrete (unconfined)
ops.uniaxialMaterial('Concrete02', IDconcCover, fpc , epsc0, fpcu, epscU, lamda, 4.0,1570)

# Core concrete (confined)
ops.uniaxialMaterial('Concrete02', IDconcCore, fc1C, epscC, fpc1C, eps1CU, lamda, 4.2, 1000)

# Masonry
ops.uniaxialMaterial('Concrete02', IDmason, fpcM , epsc0M, fpcuM, epsUM, lamdaM, 0, 0)

# STEEL
# Reinforcing steel
ops.uniaxialMaterial('Steel02', IDreinf, Fy, Es, b, R0, cR1, cR2)
```



```
#####
# SECTIONS
#####
# COLUMN
ColSecTag = 1          # Column section tag
colWidth  = 200.0     # [mm] Width of the section
colDepth  = 200.0     # [mm] Depth of the section
coverC    = 20        # [mm] Cover
colBarTop = 2         # number of bar at top
colBarBot = 2         # number of bar at bottom
dBar1     = 10.0      # [mm] Diameter of the bar
barArea1  = math.pi * dBar1**2/4.0 # Area of rebar

y1C      = colDepth/2 # The distance from the section z-axis
z1C      = colWidth/2 # The distance from the section y-axis
nfColCoreY = 30      # Number of fiber for the core in which Y is divided
nfColCoreZ = 30      # Number of fiber for the core in which Z is divided
nfColCoverY = 5      # Number of fiber for the cover in which Y is divided
nfColCoverZ = 5      # Number of fiber for the cover in which Z is divided

ops.section('Fiber', ColSecTag)

# Create the concrete core fibers
ops.patch('rect', IDconcCore, nfColCoreY, nfColCoreZ, coverC- y1C, coverC- z1C, y1C- coverC, z1C-coverC)

# Create the concrete cover fibers (top, bottom, left, right)
ops.patch('rect', IDconcCover, nfColCoverY, nfColCoverZ, -y1C, z1C-coverC, y1C, z1C)
ops.patch('rect', IDconcCover, nfColCoverY, nfColCoverZ, -y1C, -z1C, y1C, coverC-z1C)
ops.patch('rect', IDconcCover, nfColCoverY, nfColCoverZ, -y1C, coverC-z1C, coverC-y1C, z1C-coverC)
ops.patch('rect', IDconcCover, nfColCoverY, nfColCoverZ, y1C-coverC, coverC- z1C, y1C, z1C-coverC)

# Create the reinforcing fibers (top, bottom)
ops.layer('straight', IDreinf, colBarTop, barArea1, -y1C + coverC, z1C- coverC, y1C- coverC, z1C- coverC)
ops.layer('straight', IDreinf, colBarBot, barArea1, -y1+coverC, - z1C + coverC, y1C- coverC, -z1C + coverC)

#-----
# BEAM
BmSecTag = 3          # Column section tag
BmWidth  = 400.0     # [mm] Width of the section
BmDepth  = 200.0     # [mm] Depth of the section
coverB    = 20.0     # [mm] Cover
BmBarTop = 3         # number of bar at top
BmBarBot = 3         # number of bar at bot
dBar3     = 10.0     # [mm] Diameter of the bar
barArea3  = math.pi*dBar3**2/4 # Area of rebar

y2B      = BmDepth/2 # The distance from the section z-axis
z2B      = BmWidth/2 # The distance from the section y-axis

nfBmCoreY = 20      # Number of fiber for the core in which Y is divided
nfBmCoreZ = 20      # Number of fiber for the core in which Z is divided
nfBmCoverY = 2      # Number of fiber for the cover in which Y is divided
nfBmCoverZ = 2      # Number of fiber for the cover in which Z is divided
```

```

ops.section('Fiber', BmSecTag)

# Create the concrete core fibers
ops.patch('rect', IDconcCore, nfBmCoreZ, nfBmCoreY, coverB- y2B, coverB- z2B, y2B-coverB, z2B- coverB )

# Create the concrete cover fibers (top, bottom, left, right)
ops.patch('rect', IDconcCover, nfBmCoverZ, nfBmCoverY, -y2B, z2B-coverB, y2B, z2B)
ops.patch('rect', IDconcCover, nfBmCoverZ, nfBmCoverY, -y2B, -z2B, y2B, coverB-z2B )
ops.patch('rect', IDconcCover, nfBmCoverZ, nfBmCoverY, -y2B, coverB-z2B, coverB-y2B, z2B-coverB)
ops.patch('rect', IDconcCover, nfBmCoverZ, nfBmCoverY, y2B-coverB, coverB- z2B, y2B, z2B-coverB)

# Create the reinforcing fibers (left, middle, right)
ops.layer('straight', IDreinf, BmBarTop, barArea3, -y2B + coverB, z2B- coverB, y2B- coverB, z2B- coverB)
ops.layer('straight', IDreinf, BmBarBot, barArea3, -y2B + coverB, -z2B + coverB, y2B- coverB, -z2B + coverB )
#-----
# STRUTS
StrWidth1 = kwargs.get('w1', StrWidth*0.45) # [mm] Width of the section-Top Right
StrWidth2 = kwargs.get('w2', StrWidth*0.35) # [mm] Width of the section- Bottom Left
StrWidth3 = kwargs.get('w3', StrWidth*0.25) # [mm] Width of the section- Diagonal

# Top Right strut
StrSecTag1 = 11 # Top Right Strut section tag
ys1 = StrDepth/2 # The distance from the section z-axis
zs1 = StrWidth1/2 # The distance from the section y-axis
# Bottom Left strut
StrSecTag2 = 12 # Bottom Left Strut section tag
ys2 = StrDepth/2 # The distance from the section z-axis
zs2 = StrWidth2/2 # The distance from the section y-axis

# Center strut
StrSecTag3 = 13 # Center Strut section tag
ys3 = StrDepth/2 # The distance from the section z-axis
zs3 = StrWidth3/2 # The distance from the section y-axis
nfStrCoreY = 1 # Number of fiber for the core in which Y is divided
nfStrCoreZ = 1 # Number of fiber for the core in which Z is divided

# Top Right strut
ops.section('Fiber', StrSecTag1)
ops.patch('rect', IDmason, nfStrCoreZ, nfStrCoreY, -ys1, -zs1, ys1, zs1)

# Bottom Left
ops.section('Fiber', StrSecTag2)
ops.patch('rect', IDmason, nfStrCoreZ, nfStrCoreY, -ys2, -zs2, ys2, zs2)

# Center
ops.section('Fiber', StrSecTag3)
ops.patch('rect', IDmason, nfStrCoreZ, nfStrCoreY, -ys3, -zs3, ys3, zs3)

```

```
#####
# ELEMENTS
#####

# Setting element tag
lftColB = 1      # Left column bottom part
lftColU = 2      # Left column upper part
rgtColB = 3      # Right column bottom part
rgtColU = 4      # Right column upper part
topBemL = 5      # Top beam left part
topBemR = 6      # Top beam right part
botBmL  = 7      # Bottom Beam left part
botBmR  = 8      # Bottom Beam right part
str1    = 9      # Eccentric truss masonry strut
str2    = 10     # Eccentric truss masonry strut
str3    = 11     # Diagonal truss masonry strut

# Geometric Transformation
TransfTag = 1
ops.geomTransf('Linear', TransfTag )

# Integration scheme
IntColTag, IntBemTag = 1, 2
np = 5 # Number of integration points
ops.beamIntegration('Lobatto',IntColTag , ColSecTag , np)
ops.beamIntegration('Lobatto',IntBemTag , BmSecTag , np)

# COLUMN A
ops.element('forceBeamColumn', lftColB, 1 , 7, TransfTag, IntColTag )
ops.element('forceBeamColumn', lftColU, 7 , 3, TransfTag, IntColTag )

# COLUMN B
ops.element('forceBeamColumn', rgtColB , 2 , 6, TransfTag, IntColTag )
ops.element('forceBeamColumn', rgtColU , 6 , 4, TransfTag, IntColTag )

# TOP Beam
ops.element('forceBeamColumn', topBemL, 3 , 5, TransfTag, IntBemTag)
ops.element('forceBeamColumn', topBemR, 5 , 4, TransfTag, IntBemTag)

# BOTTOM Beam
#          tag, ndI, ndJ, A,      E,      IZ      transfTag
ops.element('elasticBeamColumn', botBmL, 1, 8, 60000.0, 25500 , 450000000, TransfTag)
ops.element('elasticBeamColumn', botBmR, 8, 2, 60000.0, 25500 , 450000000, TransfTag)

# STRUTS
# Top right strut
ops.element('TrussSection',str1, 5, 6, StrSecTag1)
# Bottom left strut
ops.element('TrussSection',str2, 7, 8, StrSecTag2)
# Center strut
ops.element('TrussSection',str3, 2, 3, StrSecTag3)
```

```
#####
# GRAVITY LOADS
#####
# Setting Nodal force
P1 = 200000.0      # [N] Fv vertical load on each node

# Create a Plain load pattern with a Linear TimeSeries
ops.timeSeries('Linear', 1)
ops.pattern('Plain', 1, 1)

# Create nodal loads at nodes 3 & 4
#   nd FX FY MZ
ops.load(3, 0.0, -P1, 0.0)
ops.load(4, 0.0, -P1, 0.0)

#####
# GRAVITY ANALYSIS
#####
n_steps = 10

# Create the system of equation, a sparse solver with partial pivoting
ops.system('BandGeneral')

# Create the constraint handler, the transformation method
ops.constraints('Transformation')

# Create the DOF numberer, the reverse Cuthill-McKee algorithm
ops.numberer('RCM')

# Create the convergence test, the norm of the residual with a tolerance of
# 1e-9 and a max number of iterations of 1000
ops.test('NormDisplncr', 1.0e-9, 1000, 0)

# Create the solution algorithm, a Newton-Raphson algorithm
ops.algorithm('Newton')

# Create the integration scheme, the LoadControl scheme using steps of 0.1
ops.integrator('LoadControl', 1/n_steps)

# Create the analysis object
ops.analysis('Static')

# Perform the gravity load analysis, requires 10 steps to reach the load level
ops.analyze(n_steps)
```

```
#####
# PUSHOVER ANALYSIS
#####
# CONTROL NODE id
ctrl_node = 3
# BASE NODES id
basenodes = [1, 2]

# Set the gravity loads to be constant & reset the time in the domain
ops.loadConst('-time', 0.0)

# Set lateral load pattern with a Linear TimeSeries
ops.timeSeries('Linear', 1,1)
ops.pattern('Plain', 2, 1)
# Create nodal loads at nodes 3 & 4
ops.load(ctrl_node, 1, 0, 0)
# ops.load(4, 1, 0, 0)

# Set some parameters
dU = 1# Displacement increment
# Change the integration scheme to be displacement control
ops.integrator('DisplacementControl', ctrl_node, 1, dU, 1, dU, dU)

# Set some parameters
maxU = 40 # Max displacement
currentDisp, ok = 0.0, 0

D, R, Shr2, Shr3 = [0], [0], [0], [0]
while ok == 0 and currentDisp < maxU:
    # Analyze one step
    ok = ops.analyze(1)

    # if the analysis fails try initial stiffness
    if ok != 0:
        ops.test('NormDispIncr', 1.0e-4, 2000, 0)
        ops.algorithm('ModifiedNewton', '-initial')
        ok = ops.analyze(1)
        if ok == 0:
            ops.test('NormDispIncr', 1.0e-9, 1000, 0)
            ops.algorithm('Newton')

    currentDisp = ops.nodeDisp(ctrl_node, 1)
    ops.reactions()

# Outputs
Shr2.append((-ops.eleForce(lftColU,1))/1000) # Shear force in left column
Shr3.append((-ops.eleForce(rgtColB,1))/1000) # Shear force in right column
D.append(currentDisp)
R.append(-sum([ops.nodeReaction(node, 1) for node in basenodes])/1000)
opsvis.plot_defo(sfac=10)
plt.xlabel('l` mm')
plt.ylabel('h` mm')
return D, R, Shr2, Shr3
```

```

#-----
def read_column_wo_nan(df, col_name):
    return df[col_name].dropna().to_numpy()

def read_experimental_res(exp_file, exp_columns):
    # Read experimental data from excel file
    df = pd.read_excel(exp_file)
    # Read experimental data and remove NaNs
    try:
        return [read_column_wo_nan(df, exp_col) for exp_col in exp_columns]
    except:
        raise ValueError("The excel file does not contain the expected columns. Please check the excel file and
the exp_columns variable.")

def read_refined_model_res(ref_file, ref_sheet, ref_columns):
    df = pd.read_excel(ref_file, sheet_name=ref_sheet)
    df = df.dropna()

    X = np.squeeze(df[ref_columns["X"]].to_numpy())
    L = df[ref_columns["L"]].to_numpy()
    R = df[ref_columns["R"]].to_numpy()
    return X, L, R

def interp_curves(curve_1, curve_2):
    f1 = interp1d(curve_1[:,0], curve_1[:,1], kind='linear')
    f2 = interp1d(curve_2[:,0], curve_2[:,1], kind='linear')

    a = max(min(curve_1[:,0]), min(curve_2[:,0]))

    x_common = np.arange(max(min(curve_1[:,0]), min(curve_2[:,0])), min(max(curve_1[:,0]),
max(curve_2[:,0])), 0.1)
    return x_common, f1(x_common), f2(x_common)

def rmsd(curve_1, curve_2):
    _, interp_c_1, interp_c_2 = interp_curves(curve_1, curve_2)
    return np.sqrt(np.sum((interp_c_1 - interp_c_2)** 2))

def avg_two_curves(curve_1, curve_2):
    x_new, interp_c_1, interp_c_2 = interp_curves(curve_1, curve_2)
    return np.array([x_new, (interp_c_1 + interp_c_2)/2]).T

def avg_curves(curves):
    interps = [interp1d(curve[:,0], curve[:,1], kind='linear') for curve in curves]

    max_x = max(min(curve[:,0]) for curve in curves)
    min_x = min(max(curve[:,0]) for curve in curves)

    x_common = np.arange(max_x, min_x, 0.1)
    interpolated = [interp(x_common) for interp in interps]
    return np.array([x_common, np.mean(interpolated, axis=0)]).T

```

Appendix B. *Openseespy* code for genetic algorithm (GA)

```

import numpy as np
import pygad
import tripple_struts_model as msm
import pickle
import matplotlib.pyplot as plt
import multiprocessing as mp

#Experimental data file info
exp_file = "Experimentdata_S1B.xlsx"
exp_columns = [{"A", "B"}, {"C", "D"}, {"E", "F"}, {"G", "H"}]

# Refined data file info
ref_file = 'Shear.xlsx'
ref_sheet = 'S1B'
ref_columns = {"X": "A", "L": ["F", "G", "H", "I"], "R": ["N", "O", "P", "Q"]}

# Experimental data
data_exp = msm.read_experimental_res(exp_file, exp_columns)
data_avg = msm.avg_curves(data_exp)

# Refined model data
X_loc, L_loc, R_loc = msm.read_refined_model_res(ref_file, ref_sheet, ref_columns)
exp_data = {"glob_data": data_avg, "X_loc": X_loc, "L_loc": L_loc, "R_loc": R_loc, "peak_L": np.max(L_loc[:,3]),
"peak_R": np.max(R_loc[:,3])}

alpha = 6
analysis_name = 6_200
parallel_analysis = True # otherwise False or True

def fitness_func(ga_instance, solutions, solution_idx):
    if parallel_analysis:
        # Parallel run of the fitness function
        my_pool = mp.Pool(processes=mp.cpu_count())
        fitnesses = my_pool.map(opensees_run, solutions)
        my_pool.close()
    else:
        # Sequential run of the fitness function
        fitnesses = []
        for solution in solutions:
            fitnesses.append(opensees_run(solution))

# Parallel run of the fitness function
return fitnesses

def opensees_run(params):
    # Run pushover analysis
    D, R, Shr2, Shr3 = msm.multi_structs_model(d1= params[0], d2= params[1], b1= params[2], b2= params[3])

```

```

# RMSD values
RMSD_g = msm.rmsd(exp_data["glob_data"], np.array([D,R]).T)
delta_L = np.abs(exp_data["peak_L"]- np.max(Shr2))
delta_R = np.abs(exp_data["peak_R"]- np.max(Shr3))

# Return of the fitness function
return 1/((RMSD_g+alpha*(delta_L+delta_R))/1e4) if alpha in locals() and alpha else 1/(RMSD_g)

if __name__ == "__main__":
# GA parameters
n_pop = 10 # Number of populations
n_ind = 250 # Number of individuals in the population

ga_instance = pygad.GA(num_generations=n_pop,
    num_parents_mating=3,
    sol_per_pop=n_ind,
    num_genes = 4,
    fitness_func=fitness_func,
    mutation_num_genes=1,
    keep_elitism= 2,
    fitness_batch_size = n_ind,
    init_range_low=200,
    init_range_high=800,
    gene_type=[float, 0])

# Run the GA analysis
ga_instance.run()

# Take the best solution found by GA
solution, solution_fitness, solution_idx = ga_instance.best_solution(ga_instance.last_generation_fitness)

# Save best solution into a pickle file
with open(f"best_solution_{analysis_name}.pkl", "wb") as f:
    pickle.dump({"solution": solution, "solution_fitness": solution_fitness}, f)

# Save GA results
ga_instance.save(filename=f"./GA_results_{analysis_name}")

# Plot of convergence history
fig = ga_instance.plot_fitness() #plot of convergence history
ax = fig.gca() #axes

ax.set_xlim(0) #set x-axis limits to 0
ax.set_xlabel("Generation") #set x-axis label
ax.set_ylabel("Fitness") #set y-axis label
ax.set_title("Convergence history") #set title
ax.grid(alpha = 0.75) #set grid (alpha is the transparency of the grid)
ax.get_legend().remove() #remove legend
fig.savefig(f"conv_hist_{analysis_name}.png", dpi = 150) #save figure
plt.show(fig) #show figure

```


Appendix C. *Openseespy* code for run and plot

```

import tripple_struts_model as msm
import matplotlib.pyplot as plt
import numpy as np

# Experimental data file info
exp_file = "Experimentdata_S1B.xlsx"
exp_sheet= 'S1B'
exp_columns = [{"A", "B"}, {"C", "D"}, {"E", "F"}, {"G", "H"}]

# Experimental data
data_exp = msm.read_experimental_res(exp_file, exp_columns)
data_avg = msm.avg_curves(data_exp)

# Refined data file info
ref_file = 'Shear.xlsx'
ref_sheet = 'S1B'

ref_columns = {"X": "A", "L": ["F", "G", "H", "I"], "R": ["N", "O", "P", "Q"]}
X_loc, L_loc, R_loc = msm.read_refined_model_res(ref_file, ref_sheet, ref_columns)

# Run pushover analysis
#D, R, Shr2, Shr3 = dsm.multi_structs_model(d1=498, d2= 332, b1=390, b2=208) # GA
D, R, Shr2, Shr3 = msm.multi_structs_model(d1=464.2, d2= 344.94, b1=370.11, b2=228.25) # Equation

# RMSD values
RMSD_g = msm.rmsd(data_avg, np.array([D,R]).T)
delta_L = np.abs(np.max(L_loc[:,3])- np.max(Shr2))
delta_R = np.abs(np.max(R_loc[:,3])- np.max(Shr3))
print(f"The Global RMSD value is: {RMSD_g:.2f}")
print(f"The Local response shear error in Windward column: {delta_L:.2f}")
print(f"The Local response shear error in Leeward column: {delta_R:.2f}")
print(f"Fitness: {RMSD_g+6*(delta_L+delta_R):.2f}")
#-----
# PLOTS
lc1 = 'blue'
lc2 = 'black'
lc3 = 'red'
custom_dashes = (0, (5, 5))

# Global pushover curve
fig = plt.figure()
ax = fig.gca()

ax.plot(D, R, '-', color=lc1, label='OpenSeesPy: Macro-model',linewidth=2.5)
plt.plot(data_exp[0][:,0], data_exp[0][:,1], '-', color=lc2, alpha=0.60)
plt.plot(data_exp[1][:,0], data_exp[1][:,1], '-', color=lc2,alpha=0.60)
plt.plot(data_exp[2][:,0], data_exp[2][:,1], '-', color=lc2,alpha=0.6)
plt.plot(data_exp[3][:,0], data_exp[3][:,1], '-', color=lc2, label='Experimental backbone curves',alpha=0.6)
ax.plot(data_avg[:,0], data_avg[:,1], ':',color=lc3, label='Average experimental curve', linewidth=2)
ax.grid(True, linestyle='--', linewidth=0.5, color='gray')

ax.set_xlabel('Displacement [mm]')
```

```

ax.set_ylabel('Reaction force [kN]')
#ax.set_title(f'Pushover Curves for Specimen {exp_sheet}')
ax.set_xlim(0), ax.set_ylim(0)
ax.legend()
plt.show()
plt.close(fig)
#-----
lc1 = 'green'
lc2 = 'black'
lc3 = 'red'
custom_dashes = (0, (5, 5))
# Shear plot for left column (Windward)
fig = plt.figure()
ax = fig.gca()

ax.plot(D, Shr2, '-', color=lc1, label='OpenSeesPy: Macro-model',linewidth=2.5)
ax.plot(X_loc, L_loc[:,0], '--', color=lc2, label='Shear demand at cut 1:(micro-model)')
ax.plot(X_loc, L_loc[:,1], '-.', color=lc2, label='Shear demand at cut 2:(micro-model)')
ax.plot(X_loc, L_loc[:,2], linestyle = custom_dashes, color=lc2, label='Shear demand at cut 3:(micro-model)')
ax.plot(X_loc, L_loc[:,3], ':', color=lc3, label='Average shear demand',linewidth=2)

ax.set_xlabel('Displacement [mm]')
ax.set_ylabel('Shear Force [kN]')
ax.set_title(f'Specimen {exp_sheet}: Windward Column ')
ax.set_xlim(0), ax.set_ylim(0)
ax.grid(True, linestyle='--', linewidth=0.5, color='gray')
ax.legend()

plt.show()
plt.close(fig)
#-----
# Shear plot for right column (Leeward)
fig = plt.figure()
ax = fig.gca()

ax.plot(D, Shr3, '-', color=lc1, label='OpenSeesPy: Macro-model',linewidth=2.5)
ax.plot(X_loc, R_loc[:,0], '--', color=lc2, label='Shear demand at cut 1')
ax.plot(X_loc, R_loc[:,1], '-.', color=lc2, label='Shear demand at cut 2')
ax.plot(X_loc, R_loc[:,2], linestyle = custom_dashes, color=lc2, label='Shear demand at cut 3')
ax.plot(X_loc, R_loc[:,3], ':', color=lc3, label='Average shear demand',linewidth=2)

ax.set_xlabel('Displacement [mm]')
ax.set_ylabel('Shear Force [kN]')
ax.set_title(f'Specimen {exp_sheet}: Leeward Column')

ax.grid(True, linestyle='--', linewidth=0.5, color='gray')
ax.legend()
ax.set_xlim(0), ax.set_ylim(0)
plt.show()
plt.close(fig)

```

References

- [1] O. Bolea, “The Seismic Behaviour of Reinforced Concrete Frame Structures with Infill Masonry in the Bucharest Area,” *Energy Procedia*, vol. 85, pp. 60–76, Jan. 2016, doi: 10.1016/J.EGYPRO.2015.12.275.
- [2] A. S. of C. Engineers, “Prestandard and commentary for the seismic rehabilitation of building,” 2000.
- [3] Fabio Di Trapani; Gabriele Bertagnoli; Marco Filippo Ferrotto; Diego Gino, “Empirical equations for the direct definition of stress-strain laws for fiber-section-based macromodeling of infilled frames,” *J Eng Mech*, 2018.
- [4] A. Fiore, A. Netti, and P. Monaco, “The influence of masonry infill on the seismic behaviour of RC frame buildings,” *Eng Struct*, vol. 44, pp. 133–145, Nov. 2012, doi: 10.1016/J.ENGSTRUCT.2012.05.023.
- [5] Fabio Di Trapani; Marilisa Di Benedetto; Massimo Petracca; Guido Camata, “Infill-frame interaction: refined modelling for the analysis and the estimation of the internal forces in seismic assessment for RC building structures,” in *9th International Conference on Computational Methods in Structural Dynamics and Earthquake Engineering Methods in Structural Dynamics and Earthquake Engineering*, Athens, Greece, Jun. 2023.
- [6] Humberto Salazar Amorim Varum, “Seismic assessment, strengthening and repair of existing buildings,” Universidade de Aveiro, Portugal, 2003.
- [7] André Filipe Furtado, Hugo Rodrigues, H. Varum, and A. Costa, “Assessment and strengthening strategies of existing RC buildings with potential soft-storey response,” in *9th International Masonry Conference*, Guimarães, Jul. 2014.
- [8] Matjaz Dolsek ; Peter Fajfar, “The effect of masonry infills on the seismic response of a four storey reinforced concrete frame—a probabilistic assessment,” *Eng Struct*, vol. 30, no. 11, pp. 3186–3192, Nov. 2008.
- [9] A. Furtado, H. Rodrigues, and A. Arêde, “Modelling of masonry infill walls participation in the seismic behaviour of RC buildings using OpenSees,” *International Journal of Advanced Structural Engineering*, Jan. 2015, doi: 10.1007/s40091-015-0086-5.
- [10] *Tall Buildings*. Elsevier, 1967. doi: 10.1016/C2013-0-05446-1.
- [11] R.E. Klingner and V.V. Bertero, “Infilled frames in earthquake-resistance construction ,” Berkeley, California, Dec. 1976.
- [12] Bryan Stafford Smith, “Behavior of square infilled frames,” *Journal of the Structural Division*, vol. 92, pp. 381–404, 1966.
- [13] B. STAFFORD SMITH and C. CARTER, “A METHOD OF ANALYSIS FOR INFILLED FRAMES.,” *Proceedings of the Institution of Civil Engineers*, vol. 44, no. 1, pp. 31–48, 1969, doi: 10.1680/iicep.1969.7290.
- [14] F. J. Crisafulli, “Seismic behaviour of reinforced concrete structures with masonry infills,” 1997.

-
- [15] A. B. Mehrabi, P. B. Shing, M. P. Schuller, and J. L. Noland, “Experimental Evaluation of Masonry-Infilled RC Frames,” *Journal of Structural Engineering-asce*, vol. 122, pp. 228–237, 1996, [Online]. Available: <https://api.semanticscholar.org/CorpusID:110713582>
- [16] L. Cavaleri and F. Di Trapani, “Cyclic response of masonry infilled RC frames: Experimental results and simplified modeling,” *Soil Dynamics and Earthquake Engineering*, vol. 65, pp. 224–242, Jan. 2014, doi: 10.1016/j.soildyn.2014.06.016.
- [17] P. Asteris, S. Antoniou, D. Sophianopoulos, and C. Chrysostomou, “Mathematical Macromodeling of Infilled Frames: State of the Art,” *Journal of Structural Engineering*, vol. 137, pp. 1508–1517, Jan. 2011, doi: 10.1061/(ASCE)ST.1943-541X.0000384.
- [18] F. Di Trapani, G. Macaluso, L. Cavaleri, and M. Papia, “Masonry infills and RC frames interaction: Literature overview and state of the art of macromodeling approach,” *European Journal of Environmental and Civil Engineering*, vol. 19, Jan. 2015, doi: 10.1080/19648189.2014.996671.
- [19] G. G. Deierlein, A. M. Reinhorn, and M. R. Willford, “Nonlinear structural analysis for seismic design,” *NEHRP seismic design technical brief*, vol. 4, pp. 1–36, 2010.
- [20] D. C. Kent and R. Park, “Flexural members with confined concrete,” *Journal of the structural division*, vol. 97, no. 7, pp. 1969–1990, 1971.
- [21] J. B. Mander, M. J. N. Priestley, and R. Park, “Theoretical stress-strain model for confined concrete,” *Journal of structural engineering*, vol. 114, no. 8, pp. 1804–1826, 1988.
- [22] “Springer_Handbook_of_Computational_Intel”.
- [23] C. Darwin, *The origin of species by means of natural selection: or, the preservation of favoured races in the struggle for life*, vol. 11. D. Appleton and Company, 1923.
- [24] E. Wirsansky, *Hands-on genetic algorithms with Python: applying genetic algorithms to solve real-world deep learning and artificial intelligence problems*. Packt Publishing Ltd, 2020.
- [25] F. Di Trapani, G. C. Marano, and A. P. Sberna, “A genetic algorithm-based framework for the optimal seismic retrofitting of reinforced concrete buildings by steel-jacketing”.
- [26] P. Morandi, S. Hak, and G. Magenes, “Performance-based interpretation of in-plane cyclic tests on RC frames with strong masonry infills,” *Eng Struct*, vol. 156, pp. 503–521, 2018.
- [27] F. Di Trapani, N. A. Khan, L. Zhou, C. Demartino, and G. Monti, “Cyclic response of infilled RC frames with window and door openings: Experimental results and damage interpretation,” *Earthq Eng Struct Dyn*, vol. 53, no. 1, pp. 43–67, 2024.
- [28] A. B. Mehrabi and P. B. Shing, “Finite element modeling of masonry-infilled RC frames,” *Journal of structural engineering*, vol. 123, no. 5, pp. 604–613, 1997.

- [29] F. Colangelo, “Pseudo-dynamic seismic response of reinforced concrete frames infilled with non-structural brick masonry,” *Earthq Eng Struct Dyn*, vol. 34, no. 10, pp. 1219–1241, 2005, doi: <https://doi.org/10.1002/eqe.477>.
- [30] L. Cavaleri and F. Di Trapani, “Prediction of the additional shear action on frame members due to infills,” *Bulletin of Earthquake Engineering*, vol. 13, no. 5, pp. 1425–1454, 2015, doi: [10.1007/s10518-014-9668-z](https://doi.org/10.1007/s10518-014-9668-z).